

ELECTROSPUN POLYAMIDE-6 AND POLYAMIDE-6/HALLOYSITE
NANOTUBES COMPOSITE NANOFIBERS: PARAMETER OPTIMIZATION
AND CHARACTERIZATION

A THESIS SUBMITTED TO
THE GRADUATE SCHOOL OF NATURAL AND APPLIED SCIENCES
OF
MIDDLE EAST TECHNICAL UNIVERSITY

BY

SELİN ŞAHİN

IN PARTIAL FULFILLMENT OF THE REQUIREMENTS
FOR
THE DEGREE OF MASTER OF SCIENCE
IN
CHEMICAL ENGINEERING

DECEMBER 2018

Approval of the thesis:

**ELECTROSPUN POLYAMIDE-6 AND POLYAMIDE-6/HALLOYSITE
NANOTUBES COMPOSITE NANOFIBERS: PARAMETER
OPTIMIZATION AND CHARACTERIZATION**

submitted by **SELİN ŞAHİN** in partial fulfillment of the requirements for the degree
of **Master of Science in Chemical Engineering Department, Middle East
Technical University** by,

Prof. Dr. Halil Kalıpçılar
Dean, Graduate School of **Natural and Applied Sciences**

Prof. Dr. Pınar Çalık
Head of Department, **Chemical Engineering**

Prof. Dr. Göknur Bayram
Supervisor, **Chemical Engineering Dept., METU**

Examining Committee Members:

Prof. Dr. Necati Özkan
Polymer Science and Technology Dept., METU

Prof. Dr. Göknur Bayram
Chemical Engineering Dept., METU

Prof. Dr. Bora Maviş
Mechanical Engineering Dept., Hacettepe University

Assoc. Prof. Dr. Erhan Bat
Chemical Engineering Dept., METU

Asst. Prof. Dr. Emre Büküşoğlu
Chemical Engineering Dept., METU

Date: 07.12.2018

I hereby declare that all information in this document has been obtained and presented in accordance with academic rules and ethical conduct. I also declare that, as required by these rules and conduct, I have fully cited and referenced all material and results that are not original to this work.

Name, Surname: Selin Şahin

Signature:

ABSTRACT

ELECTROSPUN POLYAMIDE-6 AND POLYAMIDE-6/HALLOYSITE NANOTUBES COMPOSITE NANOFIBERS: PARAMETER OPTIMIZATION AND CHARACTERIZATION

Şahin, Selin

Master of Science, Department of Chemical Engineering

Supervisor: Prof. Dr. Gökür Bayram

December 2018, 145 pages

Electrospinning is a very simple and efficient method in production of nanofibers with high surface area/volume ratio, thus has significant potential in developing the nanotechnology. The nano-scale fibers and the interactions in nano level among components of the fibers ensure composite nanofibers to be a promising field of research.

In this study, optimization of the electrospinning parameters for neat Polyamide-6 (PA6) nanofiber production and investigation on performance of composite nanofibers containing Halloysite Nanotubes (HNTs) were aimed. Firstly, neat PA6 nanofibers were produced by changing the solution concentration, solvent type, applied voltage, solution feed rate and tip-to-collector distance. Simultaneously, the PA6 composite nanofibers with unmodified and modified HNTs (m-HNTs) were prepared and characterized using SEM, TGA, DSC analyses and tensile tests. Also, degradation tests under chemical vapors and a flame retardancy test were performed on some selected samples.

Results revealed that the addition of 1 wt.% m-HNTs to PA6 increased the tensile modulus of the neat PA6 nanofiber mat by 25% and provided uniform fiber morphology and constant thermal properties. In degradation test, the neat PA6 and the nanofiber mat containing 1 and 8 wt.% m-HNTs were subjected to HCl, acetone, toluene and water vapors. After HCl and water vapor exposure, decrease in thermal

and mechanical properties were observed together with significant change in morphology. Chemical degradation was slightly prevented by the addition of 1 wt.% m-HNTs. Diffusion coefficients of the thin nanofiber mats exposed to these chemical vapors were determined to be in the order of 10^{-15} m²/s. LOI tests were applied to both electrospun mats and compression molded films to determine flame retardant properties. While compression molded PA6 films had a LOI value of 27% O₂, the LOI value of the electrospun PA6 mat was found as 31% O₂. This revealed the positive effect of orientation and the porous structure of the nanofibers on the flame retardant properties.

Keywords: Nanocomposite, Electrospinning, Polyamide-6, Halloysite Nanotubes, Degradation

ÖZ

ELEKTRO-EĞİRME YÖNTEMİYLE ÜRETİLEN POLİAMİD-6 VE POLİAMİD-6 /HALOYSİT NANOTÜP KOMPOZİT NANOFİBERLERİ: PARAMETRE OPTİMİZASYONU VE KARAKTERİZASYONU

Şahin, Selin
Yüksek Lisans, Kimya Mühendisliği Bölümü
Tez Yöneticisi: Prof. Dr. Göknur Bayram

Aralık 2018, 145 sayfa

Elektro-eğirme, yüksek yüzey alanı/hacim oranına sahip nanofiberlerin üretiminde kullanılan çok basit ve verimli bir yöntemdir, dolayısıyla nanoteknolojinin geliştirilmesinde önemli bir potansiyele sahiptir. Nano-ölçekli fiberler ve fiber bileşenleri arasındaki nano düzeydeki etkileşimler, kompozit nanofiberlerin umut vaat eden bir araştırma alanı olmasını sağlamaktadır.

Bu çalışmada, katkısız Poliamid-6 (PA6) nanofiberlerinin üretimi için elektro-eğirme parametrelerinin optimizasyonu ve Halloysit Nanotüp (HNT) içeren PA6 kompozit nanofiberlerin performansının araştırılması amaçlanmıştır. İlk olarak, katkısız PA6 nanofiberler, çözelti konsantrasyonu, çözücü tipi, uygulanan elektrik potansiyeli, çözelti besleme debisi ve toplama uzaklığı değerleri değiştirilerek üretilmiştir. Eş zamanlı olarak, modifiye edilmemiş ve edilmiş HNT içeren PA6 kompozit nanofiberleri hazırlanmıştır ve SEM, TGA, DSC analizleri ve çekme testi kullanılarak karakterize edilmiştir. Ayrıca kimyasal buhar ortamında bozunma ve yanmaya karşı dayanım testleri seçilen bazı numuneler üzerinde uygulanmıştır.

Sonuçlar PA6'ya ağırlıkça %1 modifiye edilmiş HNT eklenmesiyle saf PA6 nanofiber dokumanın çekme modülünün %25 oranında arttırıldığını, düzgün fiber morfolojisinin ve sabit termal özelliklerin sağlandığını ortaya çıkarmıştır. Bozunma testlerinde, saf PA6 ve ağırlıkça % 1 ve 8 modifiye edilmiş HNT içeren nanofiber dokumalar HCl, aseton, toluen ve su buharlarına maruz bırakılmıştır. HCl ve su buharı etkileşimlerinden sonra

morfolojide belirgin deęişim ile birlikte termal ve mekanik özelliklerde azalma gözlemlenmiştir. Kimyasal bozunma, ağırlıkça %1 modifiye edilmiş HNT eklenmesiyle bir miktar önlenmiştir. Bu kimyasal buharlara maruz kalan ince nanofiber dokumaların difüzyon katsayılarının 10^{-15} m²/s mertebesinde olduğu belirlenmiştir. Hem elektro-eęirme yöntemiyle üretilmiş dokumalara hem de basınçlı kalıplama ile üretilmiş filmlere LOI testi uygulanmıştır. Basınçlı kalıplama ile üretilen PA6 filmlerin LOI değeri %27 O₂ iken, elektro-eęirme yöntemiyle üretilen PA6 dokumaların LOI değeri %31 O₂ olarak bulunmuştur. Bu sonuç, nanofiberlerin oryantasyonunun ve boşluklu yapısının yanmayı geciktirici özellikler üzerinde olumlu etkisi olduğunu göstermektedir.

Anahtar Kelimeler: Nanokompozit, Elektro-eęirme, Poliamid-6, Halosit Nanotüp, Bozunma

To my precious family...

ACKNOWLEDGMENTS

I would like to express my gratitude to my supervisor, Prof. Dr. Gökür Bayram, for her guidance, advice and criticism throughout the research. Her wisdom and support motivated me and gave me a strength. Without her patience and understanding, completing this thesis would have been almost impossible.

I would like to thank the Scientific and Technological Research Council of Turkey (TUBITAK) for financial supporting this study by the 315M018 project.

I would like to express my gratitude to Refik Barış Yılmaz, Berrak Erkmen and Deniz Budak for their friendship and great help both in research and experiments.

I also would like to thank my friends from polymer group of METU; Merve Özkutlu and Almira Çaldıklıođlu for their friendship and help during my experiments.

I want to thank to my lovely friends Nisa, Nurber, Özge, Burak, İrem, Aslı, Yağmur, Soner, Fatma and Merve and for creating an enjoyable, supportive and friendly environment during the graduate education.

I am also thankful to Dilara Hasdemir, Gonca Gencer and my cat Lilikush for creating restful environment in home and being a family to me.

I am also thankful to my cousin Ebru Söylemez. I believe that we will be there for each other all the time. Thank you!

I also express my deepest gratitude to Erdem Canbalaban. I am very lucky to have you, thank you!

Last but not least, I would like to thank my parents, Rıza and Lale Şahin, and my lovely sister Seçkin Şahin, for their endless love, trust and support in every step of my life. My success wouldn't have been possible, without their encouragement and love.

TABLE OF CONTENTS

ABSTRACT.....	v
ÖZ.....	vii
ACKNOWLEDGMENTS.....	x
TABLE OF CONTENTS.....	xi
LIST OF TABLES.....	xiv
LIST OF FIGURES.....	xvi
CHAPTERS	
1.INTRODUCTION.....	1
2.BACKGROUND.....	3
2.1 Nanofibers.....	3
2.2 Electrospinning.....	3
2.2.1 Solution Parameters.....	5
2.2.1.1 Solution Concentration.....	5
2.2.1.2 Viscosity.....	6
2.2.1.3 Molecular Weight.....	6
2.2.1.4 Conductivity.....	7
2.2.1.5 Surface Tension.....	8
2.2.2 Process Parameters.....	8
2.2.2.1 Voltage.....	8
2.2.2.2 Feed Rate.....	10
2.2.2.3 Tip to Collector Distance.....	10
2.2.3 Ambient Parameters.....	11
2.3 Composite Nanofibers.....	12
2.4 Degradation Properties of Nanofibers.....	15
2.4.1 Diffusion Theory in Polymers.....	17
2.5 The Scope of the Thesis.....	19
3.MATERIALS.....	21
3.1 Materials.....	21
3.1.1 Polyamide-6 (PA6).....	21

3.1.2 Halloysite Nanotubes (HNTs)	21
3.1.3 Solvents and Other Chemicals	22
3.2 Experimental Procedure	22
3.2.1 Preparation of Polymer Solution	22
3.2.2 Surface Modification of Halloysite Nanotubes	22
3.2.3 Preparation of Composite Solution	23
3.1.1 Electrospinning Process	24
3.3 Characterization Methods	26
3.3.1 Viscosity Measurement	26
3.3.2 Scanning Electron Microscopy (SEM) Analysis	26
3.3.3 Transmission Electron Microscopy (TEM) Analysis.....	27
3.3.4 Fourier Transformed Infrared (FTIR) Spectroscopy.....	27
3.3.5 Thermogravimetric Analysis (TGA).....	27
3.3.6 Differential Scanning Calorimetry (DSC) Analysis.....	27
3.3.7 Tensile Test	28
3.3.8 Limiting Oxygen Index Test	29
3.3.9 Degradation of Electrospun Mats under Chemical Vapors.....	30
4.RESULTS AND DISCUSSION	33
4.1 Parameter Study of Electrospinning.....	33
4.1.1 Solution Concentration Optimization.....	33
4.1.2 Solvent Type and Concentration Optimization.....	36
4.1.3 Voltage Optimization	39
4.1.3.1 Scanning Electron Microscopy (SEM) Analysis	39
4.1.3.2 Thermogravimetric Analysis (TGA)	42
4.1.3.3 Differential Scanning Calorimetry (DSC) Analysis.....	43
4.1.3.4 Tensile Test Results	44
4.1.4 Feed Rate Optimization.....	46
4.1.4.1 Scanning Electron Microscopy (SEM) Analysis	47
4.1.4.2 Thermogravimetric Analysis (TGA)	50
4.1.4.3 Differential Scanning Calorimetry (DSC) Analysis.....	50
4.1.4.4 Tensile Test Results	51
4.1.5 Tip-to-Collector Distance Optimization.....	53
4.1.5.1 Scanning Electron Microscopy (SEM) Analysis	53

4.1.5.2 Thermogravimetric Analysis (TGA).....	56
4.1.5.3 Differential Scanning Calorimetry (DSC) Analysis	57
4.1.5.4 Tensile Test Results	58
4.2 Preparation and Characterization of Electrospun Fibers of PA6/HNTs Nanocomposites	60
4.2.1 Scanning Electron Microscopy (SEM) Analysis	60
4.2.2 Transmission Electron Microscopy (TEM) Analysis	67
4.2.3 Thermogravimetric Analysis (TGA).....	68
4.2.4 Differential Scanning Calorimetry (DSC) Analysis	70
4.2.5 Tensile Test Results	71
4.3 Degradation of Electrospun Mats under Chemical Vapors.....	78
4.3.1 Fourier Transformed Infrared (FTIR) Spectroscopy Analysis.....	89
4.3.2 Scanning Electron Microscopy (SEM) Analysis	100
4.3.3 Thermogravimetric Analysis.....	104
4.3.4 Differential Scanning Calorimeter	110
4.3.5 Tensile Test Results	112
4.4 Limiting Oxygen Index Test	117
5.CONCLUSIONS.....	119
REFERENCES.....	121
APPENDICES	
APPENDIX A	131
APPENDIX B	133
APPENDIX C	135
APPENDIX D	139
APPENDIX E	141

LIST OF TABLES

TABLES

Table 1. The properties of PA6 [54].	21
Table 2. Physical properties of HNTs [55].	21
Table 3. Technical information of the Inovenso Ne 300 electrospinning device [57].	25
Table 4. Parameters of the electrospinning process.	26
Table 5. Viscosity results of 10, 15 and 20 wt.% polymer solutions.	34
Table 6. DSC data of the nanofibers produced using different applied voltage values.	44
Table 7. DSC data of the nanofibers produced using different feed rate values.	51
Table 8. DSC data of the nanofibers produced using different feed rate values.	58
Table 9. Decomposition temperatures of un-HNTs and m-HNTs containing composite nanofibers.	70
Table 10. DSC data of un-HNTs and m-HNTs containing composite nanofibers.	71
Table 11. Weight changes at equilibrium and diffusion coefficients of the samples exposed to different chemical vapors.	89
Table 12. The expected FTIR bands for PA6 [80, 81].	90
Table 13. Decomposition temperatures of the samples exposed to different chemical vapors in the old setup.	107
Table 14. Decomposition temperatures of the samples exposed to different chemical vapors in the new setup.	110
Table 15. DSC data of the samples exposed to different chemical vapors in the old setup.	111
Table 16. DSC data of the samples exposed to different chemical vapors in the new setup.	111
Table C.1. Tensile test data of the nanofiber mats produced using different voltage values.	135
Table C.2. Tensile test data of the nanofiber mats produced using different feed rate values.	135

Table C.3. Tensile test data of the nanofiber mats produced using different tip-to-collector distance values.	135
Table C.4. Tensile test data of the composite nanofiber mats containing un-HNTs and m-HNTs.	136
Table C.5. Tensile test data of the samples exposed to different chemical vapors in the old setup.	137
Table C.6. Tensile test data of the samples exposed to different chemical vapors in the new setup.	138
Table D.1. Data used to calculate the diffusion coefficient of the samples containing 1 wt.% m-HNTs exposed to acetone vapor.	139

LIST OF FIGURES

FIGURES

Figure 1. Schematic representation of electrospinning process.	5
Figure 2. Effects of voltage on electrospinning and fiber diameter	9
Figure 3. Applications of electrospun nanocomposites	13
Figure 4. Experimental procedure of surface modification of HNTs.	23
Figure 5. Experimental procedure for the preparation of composite solution.	24
Figure 6. Inovenso Ne 300 electrospinning device.	25
Figure 7. Shimadzu Autograph AG-IS 100kN universal tensile test machine.....	28
Figure 8. Specimen dimensions and the shape of the tensile test specimens.....	29
Figure 9. Frame with a width of 1 cm and test setup for the LOI test.	30
Figure 10. (a) Sample holder of the old setup (b) desiccator where the experiments are carried out with the first setup (c) new setup with glass grid.....	32
Figure 11. SEM micrograph of the fibers produced with (a) 10, (b) 15, (c) 20, (d) 30 wt.% PA6 solutions.	35
Figure 12. Cumulative frequency of fiber diameters of the nanofibers produced with different solution concentrations.	36
Figure 13. SEM micrograph of the fibers produced with (a) 10, (b) 15, (c) 20, (d) 30 wt.% PA6 solutions in FA and AA solvent mixture.	37
Figure 14. Cumulative frequency of fiber diameters of the nanofibers produced with different solution concentrations (FA and AA solvent mixture).....	38
Figure 15. (a) SEM micrograph of fibers produced with 20 wt.% PA6 solution (FA); (b) SEM micrograph of the fibers produced with 20 wt.% PA6 solution (FA and AA mixture).	39
Figure 16. SEM micrograph of neat PA6 nanofibers produced using (a) 25, (b) 30, (c) 35, (d) 40 kV applied voltages.	41
Figure 17. Cumulative frequency of fiber diameters of the nanofibers produced with different applied voltages.	42
Figure 18. TGA curves of the nanofibers produced using different applied voltage values.....	43

Figure 19. Tensile strengths of the nanofiber mats produced using different applied voltage values.....	45
Figure 20. Tensile moduli of the nanofiber mats produced using different applied voltage values.....	46
Figure 21. Elongation at break of the nanofiber mats produced using different applied voltage values.....	46
Figure 22. SEM micrograph of neat PA6 nanofibers produced using (a) 0.10, (b) 0.20, (c) 0.25, (d) 0.30, (e) 0.33, (f) 0.35 (g) 0.40 mL/h feed rates.	48
Figure 23. Cumulative frequency of fiber diameters of the nanofibers produced with different feed rates.....	49
Figure 24. TGA curves of the nanofibers produced using different feed rate values.	50
Figure 25. Tensile strengths of the nanofiber mats produced using different feed rate values.....	52
Figure 26. Tensile moduli of the nanofiber mats produced using different feed rate values.....	52
Figure 27. Elongation at break of the nanofiber mats produced using different feed rate values.....	53
Figure 28. SEM micrograph of neat PA6 nanofibers produced using (a) 5, (b) 7, (c) 9, (d) 10, (e) 12, (f) 15 cm tip-to-collector distances.	55
Figure 29. Cumulative frequency of fiber diameters of the nanofibers produced with different tip-to-collector distances.	56
Figure 30. TGA curves of the nanofibers produced using different tip-to-collector distance values.	57
Figure 31. Tensile strengths of the nanofiber mats produced using different tip-to-collector distance values.	59
Figure 32. Tensile moduli of the nanofiber mats produced using different tip-to-collector distance values.	59
Figure 33. Elongation at break of the nanofiber mats produced using different tip-to-collector distance values.	60
Figure 34. SEM micrograph of the composite containing 1 wt.% un-HNTs (a) SEM micrograph at 1000x magnification (b) at 100000x magnification.	61

Figure 35. SEM micrograph of the composite containing 2 wt.% un-HNTs (a) SEM micrograph at 1000x magnification (b) at 100000x magnification.....	61
Figure 36. SEM micrograph of the composite containing 4 wt.% un-HNTs (a) SEM micrograph at 1000x magnification (b) at 100000x magnification.....	62
Figure 37. SEM micrograph of the composite containing 6 wt.% un-HNTs (a) SEM micrograph at 1000x magnification (b) at 100000x magnification.....	62
Figure 38. SEM micrograph of the composite containing 8 wt.% un-HNTs (a) SEM micrograph at 1000x magnification (b) at 100000x magnification.....	63
Figure 39. Cumulative frequency of fiber diameters of the nanofiber nanocomposites containing different un-HNT concentration.	63
Figure 40. SEM micrograph of the composite containing 1 wt.% m-HNTs (a) SEM micrograph at 1000x magnification (b) at 100000x magnification.....	64
Figure 41. SEM micrograph of the composite containing 2 wt.% m-HNTs (a) SEM micrograph at 1000x magnification (b) at 100000x magnification.....	65
Figure 42. SEM micrograph of the composite containing 4 wt.% m-HNTs (a) SEM micrograph at 1000x magnification (b) at 100000x magnification.....	65
Figure 43. SEM micrograph of the composite containing 6 wt.% m-HNTs (a) SEM micrograph at 1000x magnification (b) at 100000x magnification.....	66
Figure 44. SEM micrograph of the composite containing 8 wt.% m-HNTs (a) SEM micrograph at 1000x magnification (b) at 100000x magnification.....	66
Figure 45. Cumulative frequency of fiber diameters of the nanofiber nanocomposites containing different un-HNT concentration.	67
Figure 46. TEM micrographs of the composite nanofibers containing 1 wt.% m-HNTs at different magnifications.	68
Figure 47. TEM micrographs of the composite nanofibers containing 8 wt.% m-HNTs at different magnifications.	68
Figure 48. TGA graphs of the nanofiber nanocomposites containing different un-HNTs.	69
Figure 49. TGA graphs of the nanofiber nanocomposites containing different m-HNTs.	69
Figure 50. Representative stress-strain graph of the nanofiber mat produced using neat PA6.....	72

Figure 51. Tensile strengths of un-HNTs and m-HNTs containing composite nanofiber mats.	73
Figure 52. Tensile moduli of un-HNTs and m-HNTs containing composite nanofiber mats.	74
Figure 53. Elongation at break of un-HNTs and m-HNTs containing composite nanofiber mats.	74
Figure 54. SEM micrograph of the rupture surface of the neat PA6 sample after tensile test.	75
Figure 55. SEM micrograph of the rupture surface of the composite nanofibers containing 1 wt.% (a) un- HNTs, (b) m-HNTs after tensile test.....	76
Figure 56. SEM micrograph of the rupture surface of the composite nanofibers containing 2 wt.% (a) un- HNTs, (b) m-HNTs after tensile test.....	76
Figure 57. SEM micrograph of the rupture surface of the composite nanofibers containing 4 wt.% (a) un- HNTs, (b) m-HNTs after tensile test.....	77
Figure 58. SEM micrograph of the rupture surface of the composite nanofibers containing 6 wt.% (a) un- HNTs, (b) m-HNTs after tensile test.....	77
Figure 59. SEM micrograph of the rupture surface of the composite nanofibers containing 8 wt.% (a) un- HNTs, (b) m-HNTs after tensile test.....	78
Figure 60. Weight change graph of the samples exposed to HCl vapor.	79
Figure 61. Weight change graph of the samples exposed to acetone vapor.	80
Figure 62. Weight change graph of the samples exposed to toluene vapor.	80
Figure 63. Weight change graph of the samples exposed to water vapor.....	81
Figure 64. Percent weight change graph of the samples exposed to HCl vapor.....	82
Figure 65. Percent weight change graph of the samples exposed to acetone vapor. .	83
Figure 66. Percent weight change graph of the samples exposed to toluene vapor...	84
Figure 67. Percent weight change graph of the samples exposed to water vapor.....	85
Figure 68. Normalized weight increase as a function of square root of time for HCl exposed samples.....	86
Figure 69. Normalized weight increase as a function of square root of time for acetone exposed samples.....	87
Figure 70. Normalized weight increase as a function of square root of time for toluene exposed samples.....	88

Figure 71. Normalized weight increase as a function of square root of time for water exposed samples.....	89
Figure 72. (a) FTIR graphs (b) zoomed FTIR graphs of the samples exposed to HCl vapor in the old setup.	92
Figure 73. (a) FTIR graphs (b) zoomed FTIR graphs of the samples exposed to acetone vapor in the old setup.	93
Figure 74. (a) FTIR graphs (b) zoomed FTIR graphs of the samples exposed to toluene vapor in the old setup.	94
Figure 75. (a) FTIR graphs (b) zoomed FTIR graphs of the samples exposed to water vapor in the old setup.	95
Figure 76. (a) FTIR graphs (b) zoomed FTIR graphs of the samples exposed to HCl vapor in the new setup.....	96
Figure 77. (a) FTIR graphs (b) zoomed FTIR graphs of the samples exposed to acetone vapor in the new setup.....	97
Figure 78. (a) FTIR graphs (b) zoomed FTIR graphs of the samples exposed to toluene vapor in the new setup.....	98
Figure 79. (a) FTIR graphs (b) zoomed FTIR graphs of the samples exposed to water vapor in the new setup.....	99
Figure 80. SEM images of unexposed (a) neat PA6 (b) 1 wt.% m-HNTs (c) 8 wt.% m-HNTs; HCl exposed (d) neat PA6 (e) 1 wt.% m-HNTs (f) 8 wt.% m-HNTs; acetone exposed (g) neat PA6 (h) 1 wt.% m-HNTs (i) 8 wt.% m-HNTs; toluene exposed (j) neat PA6 (k) 1 wt.% m-HNTs (l) 8 wt.% m-HNTs; water exposed (m) neat PA6 (n) 1 wt.% m-HNTs (o) 8 wt.% m-HNTs samples in the old setup.....	101
Figure 81. SEM images of unexposed (a) neat PA6 (b) 1 wt.% m-HNTs (c) 8 wt.% m-HNTs; HCl exposed (d) neat PA6 (e) 1 wt.% m-HNTs (f) 8 wt.% m-HNTs; acetone exposed (g) neat PA6 (h) 1 wt.% m-HNTs (i) 8 wt.% m-HNTs; toluene exposed (j) neat PA6 (k) 1 wt.% m-HNTs (l) 8 wt.% m-HNTs; water exposed (m) neat PA6 (n) 1 wt.% m-HNTs (o) 8 wt.% m-HNTs samples in the new setup.	103
Figure 82. TGA graphs of the samples exposed to HCl vapor in the old setup.	105
Figure 83. TGA graphs of the samples exposed to acetone vapor in the old setup.	105
Figure 84. TGA graphs of the samples exposed to toluene vapor in the old setup..	106
Figure 85. TGA graphs of the samples exposed to water vapor in the old setup.....	106

Figure 86. TGA graphs of the samples exposed to HCl vapor in the new setup.	108
Figure 87. TGA graphs of the samples exposed to acetone vapor in the new setup.	108
Figure 88. TGA graphs of the samples exposed to toluene vapor in the new setup.	109
Figure 89. TGA graphs of the samples exposed to water vapor in the new setup. ..	109
Figure 90. Tensile strengths of the samples exposed to different chemical vapors in the old setup.	113
Figure 91. Tensile moduli of the samples exposed to different chemical vapors in the old setup.	114
Figure 92. Elongation at break of the samples exposed to different chemical vapors in the old setup.	114
Figure 93. Tensile strengths of the samples exposed to different chemical vapors in the new setup.	116
Figure 94. Tensile moduli of the samples exposed to different chemical vapors in the new setup.	116
Figure 95. Elongation at break of the samples exposed to different chemical vapors in the new setup.	117
Figure 96. SEM micrographs of the neat PA6 nanofiber mat on which the LOI test applied.	118
Figure A.1. FTIR Spectra of unmodified and 1 wt.% APTES modified HNTs.	131
Figure B.1. DSC curves of the nanofibers produced using different applied voltage values.	133
Figure B.2. DSC curves of the nanofibers produced using different feed rate values.	133
Figure B.3. DSC curves of the nanofibers produced using different tip-to-collector distance values.	134
Figure E.1. Cumulative frequency plots of fiber diameters of the samples exposed to HCl vapor in the old setup.	141
Figure E.2. Cumulative frequency of fiber diameters of the samples exposed to acetone vapor in the old setup.	142
Figure E.3. Cumulative frequency of fiber diameters of the samples exposed to toluene vapor in the old setup.	142

Figure E.4. Cumulative frequency of fiber diameters of the samples exposed to water vapor in the old setup.	143
Figure E. 5. Cumulative frequency of fiber diameters of the samples exposed to HCl vapor in the new setup.....	143
Figure E.6. Cumulative frequency of fiber diameters of the samples exposed to acetone vapor in the new setup.....	144
Figure E.7. Cumulative frequency of fiber diameters of the samples exposed to toluene vapor in the new setup.....	144
Figure E.8. Cumulative frequency of fiber diameters of the samples exposed to water vapor in the new setup.....	145

CHAPTER 1

INTRODUCTION

Electrospinning is a special method of producing nanofibers using electrostatic force. This method is generally applied to polymer-based materials including natural and synthetic polymers. Electrospinning technique has far superior properties to other nanofiber production methods such as drawing, template synthesis, phase separation and self-assembly [1], and it is anticipated that these properties will contribute to improvements in the nanotechnology field. Both the fact that the produced fibers are in the nano-size and they are produced using a reinforcement material ensures that the composite fibers have improved properties and can be used in surface applications and areas where high mechanical properties are required.

Electrospinning is a process that forms nanofibers with the aid of an electrically charged polymer solution or polymer melt. In this method, the potential difference between the tip of nozzle and collector provides to form polymer jet. The chain entanglements in the polymer solution yield the continuous polymer jet formation. The fibers that produced from the melt polymer cool and dry during the electrospinning process by the influence of the environment. However, in the fibers produced using the polymer solution, the solvent evaporates and the fibers are obtained [1].

Electrospinning has been extensively explored in recent years due to its many uses, such as filtration, optical and chemical sensors, protective clothing, biomedical applications and nanocomposite production. Many different polymers can be used for electrospun production. Polyamide-6 (PA6) is one of these polymers and is widely used as an engineering plastic due to its superior mechanical properties. In addition, Halloysite nanotubes (HNTs) have begun to attract interest as polymer additives in recent years. These materials are natural nanotubes that are harmless, inexpensive and environmentally friendly for human health. HNTs, also described as a "green" nano-material, have been extensively studied in many polymer matrices [2, 3].

In this thesis, it was aimed to optimize the electrospinning process parameters of PA6 nanofibers. In addition, multifunctional properties of PA6/HNTs composite nanofiber mats were investigated in terms of their thermal, mechanical, flame retardant properties and degradation under different chemical vapors. Many studies have been carried out using electrospinning method to produce PA6 nanofibers without additives [4–6]. On the contrary, there is a lack of research in use of HNTs as an additive in the electrospinning, which has superior features and future promise. Both nanocomposite production by using electrospinning method and use of HNTs as an additive constitute the original values of the study. In addition to all these, PA6/HNTs nanocomposite produced with the aim of having resistant to chemical degradation with improved mechanical, thermal and fire retardant properties is the first in this field. Determination of degradation properties provides information that may be useful for the usage areas (protective equipment, filtration etc.) and lifetime of nanofiber mats.

CHAPTER 2

BACKGROUND

2.1 Nanofibers

The fibers are one-dimensional structures having a linear, longitudinal extension, and they can be produced naturally and synthetically. Today, polymeric fibers are used in many important applications such as filtration, composites production, tissue engineering, sensors and surface applications [7]. The reduction in fiber diameter provides many superior properties in many aspects. In filtration applications, lower fiber diameter increases the specific surface area, which provides the higher filtration efficiency. In composites, large specific surface area provides the strong interface between reinforcement and matrix material. In addition, lower diameters lead to increase in the mechanical properties such as tensile strength and stiffness of fibers. For these reasons the usage of nanofibers is beneficial in many ways [8, 9].

Nanofiber is a fiber with a nanoscale diameter and it can be produced by several techniques such as drawing, template synthesis, phase separation, self-assembly and electrospinning [1]. Electrospinning is the simplest and commonly used of these techniques.

2.2 Electrospinning

In electrospinning process, electric field is used to overcome the surface tension of polymer solutions or melts to produce polymer jet. By using this technique, nanofibers, nanowires and nanotubes can be produced [8]. Electrospinning process should consist of a syringe that holds the polymer solution, the high voltage supply and the collector. Under high voltage, electrospinning process starts with Taylor cone formation from polymer solution. The jet formed as a result of stretching the polymer solution moves towards the collector and fiber formation is completed with the evaporation of the solvent from jet. Breaking up of the polymer jet can be prevented by chain entanglements [1].

There are many types of polymers such as polyamides, polyurethanes, polycarbonate, polyethylene oxide, etc. [7] that can be used in the electrospinning process. These polymers and their composites can be produced directly by electrospinning. Inorganic materials like carbon nanotubes and ceramics require post-processing after electrospinning [1].

The schematic representation of electrospinning device is shown in Figure 1. There exists a collector, high voltage supply, syringe pump and polymer solution as seen in the figure. Productivity of electrospinning process and nanofiber arrangements depends on the collector type. This is due to the conductivity of the collector that affects amount of fibers collected on the collector [10]. Two types of collectors are used to obtain the nanofibers: plate collector and rotating drums. Aligned fibers can be obtained using a rotating drum, but this requires a high rotating speeds which also can cause to change fiber diameter.

In order to understand the electrospinning process and the formation of fibers from the polymer solution, working parameters are very important. These parameters can be divided into three; solution parameters, process parameters and ambient parameters. To produce smooth and continuous fibers, those parameters are optimized and effect of each parameter can be investigated [11].

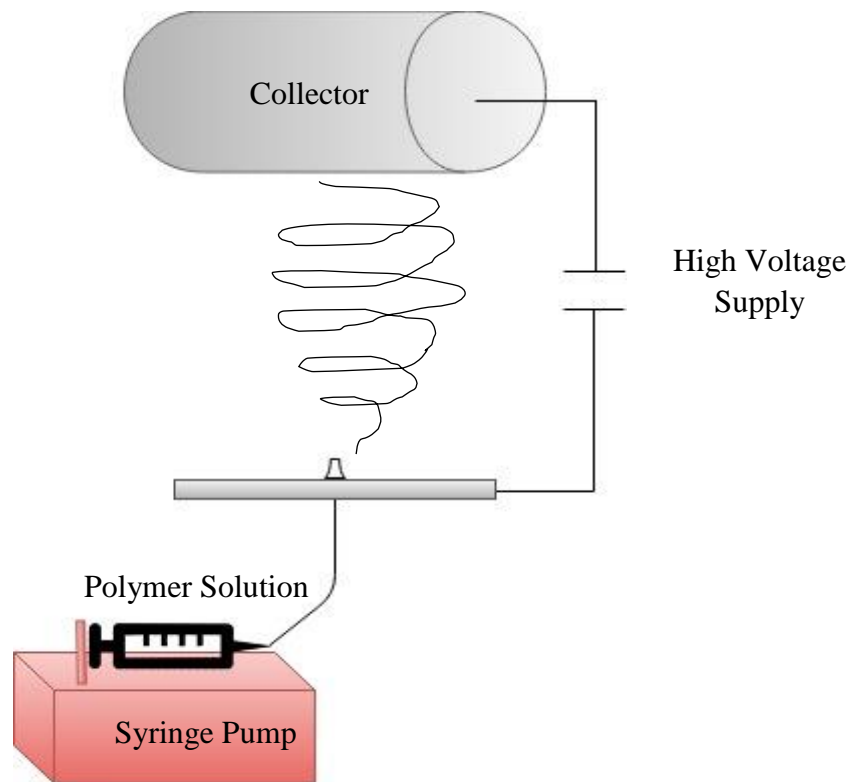


Figure 1. Schematic representation of electrospinning process.

2.2.1 Solution Parameters

The solution parameters affecting the electrospinning process are solution concentration, viscosity, molecular weight, conductivity and surface tension of polymer solution.

2.2.1.1 Solution Concentration

The solution concentration is one of the important parameters affecting the production process and fiber morphology [12]. The electrospinning process requires stretching of the polymer jet to produce nanofibers. This stretching is significantly affected by the solution concentration. Due to stretching and surface tension at low concentrations, entangled polymer chains break into small parts before reaching the collector, resulting in bead formation [13]. The viscosity increases with increasing solution concentration, which also increases chain entanglements. At high solution concentrations, these chain entanglements overcome the surface tension easily and smooth fibers without beads

can be produced. When the concentration of the solution exceeds the value at which the bead-free fiber can be produced, a needle-tip blocking is observed due to rapid evaporation of the solvent during production. This may cause the formation of defected and beaded fibers [13]. If the concentration of the solution is too high, formation of ribbon shaped fiber is observed.

Zhang et al. [14] stated that at higher polymer concentrations, the polymer chains become more entangled and thus lose their ability to move, resulting in reduced stretching during production, and thicker fibers are produced. It is noted that the ribbon-shaped fiber formation is caused by the rapid evaporation of the solvent during the process [14, 15].

2.2.1.2 Viscosity

The viscosity of the solution is an important parameter affecting the fiber morphology and is directly proportional to the solution concentration. As mentioned in the part of solution concentration, at low viscosities beaded fibers are obtained. As expected, insufficient viscosities cause to produce fibers with defected structures. The formation of the beads in the electrospinning process is also explained by the formation of droplets in order to reduce the surface area in the polymer jet due to insufficient surface tension. On the contrary, at high viscosities, the axial stretching would be insufficient due to the high viscoelastic forces, and thick fibers are obtained [17].

According to Heikkilä and Harlin [18], solution viscosity is the most important parameter affecting the diameter of the nanofibers. Beaded and fine fiber formation was observed at low viscosities, and as the viscosity increased, smooth and thicker fiber formation was observed. In low viscosities, polymer chains have increased mobility and lower stability. This causes the polymer jet to overstretch. With increasing amount of polymer, the mobility of polymer chains is restricted and the jet stretching is reduced.

2.2.1.3 Molecular Weight

Molecular weight which indicates presence of chain entanglements in the polymer structure is another parameter that affects fiber structure. If the molecular weight is

reduced at the constant solution concentration, the formation of the beaded fibers, if increased, the formation of the ribbon-shaped fiber are observed. Sufficient intermolecular interaction must occur to form smooth and non-beaded fibers. Chain entanglements and hydrogen bond formation favor the interaction which also improve the electrospinnability [19]. However, if this interaction is provided by the presence of an oligomer, the effect of molecular weight should not be considered [12].

Koski et al. [20] reported that the fiber diameter increases with increasing molecular weight. The cross-sections of the fibers at low molecular weights are circular. As the solution concentration increases, the diameters of the fibers increase and the formation of ribbon-shaped fibers is observed instead of circularly shaped fibers. In fibers produced using low molecular weight polymers, transition from circular cross-section fibers to ribbon-shaped fibers takes place at higher solution concentrations than those produced with polymers of high molecular weight.

2.2.1.4 Conductivity

Stretching occurs by repulsing the charges on the surface of the polymer jet. If the conductivity of the solution is high, the polymer jet will carry more charges, resulting in more stretching. More stretching causes the formation of fine fibers. In addition, when the conductivity is too high, instabilities occur, which affects the continuity of the electrospinning process. On the other hand, if the conductivity of the polymer solution is zero, no polymer jet can form [1]. The conductivity of the solution can be adjusted with the polymer type, solution type and salt addition. Adding ionic salts (NaCl and KH_2PO_4) and using organic acids as solvents can increase conductivity [12].

Nirmala et al. [21] produced PA6 nanofibers by electrospinning and investigated the effects of different solvents on the formation of very fine fibers with a high aspect ratio. For this purpose, the electrical conductivity values of polymer solutions prepared with different solvents, including formic acid, were compared. It has been found that the formation of very thin fibers increases with the increase of the electrical conductivity of the solution. These interesting structures have potential to be used in the fields such as filtration, composite production, drug transport and tissue engineering.

2.2.1.5 Surface Tension

The polymer solution accumulates at the tip of the nozzle due to surface tension. During the electrospinning process, the electrical forces balance the surface tension and the polymer droplet is elongated to form Taylor Cone. If this force exceeds the surface tension, a polymer jet will form and move towards the collector [22]. At low solution concentrations, solvent molecules tend to form a droplet due to surface tension. Along with increased solution concentration, solvent and polymer molecules interact more and reduce the tendency of solvent molecules to form spherical shape [1]. For this reason, reduced surface tension by changing solvent type at constant solution concentration prevents the formation of beaded fibers [12].

In a study of Yang et al. [16], the effect of surface tension on fiber morphology was investigated. Polyvinylpyrrolidone (PVP) fibers were prepared with different solvents and compared at constant concentration. It has been found that the fibers produced from solutions with high surface tension and low viscosity are beaded, and the fibers produced from solutions having low surface tension and high viscosity are bead-free and smooth.

2.2.2 Process Parameters

The process parameters are important for the electrospinning process that are external factors affecting the polymer jet. These parameters are voltage, feed rate and tip-collector distance.

2.2.2.1 Voltage

The crucial factor in the electrospinning process is applied voltage, which must exceed a certain value in order to be able to form the polymer jet during process. This value must be large enough to overcome the surface tension and which is different for each polymer solution. Throughout the electrospinning process, always an excess amount of polymer solution is accessible in the form of Taylor Cone from which fiber production can be done. If the applied voltage is higher than threshold value, the polymer jet is accelerated and more amount of solution turns into fiber. As more of the

solution fed to the nozzle is drawn by the electric force, a smaller and unstable Taylor Cone forms [23].

In many cases, the high voltage provides a reduction in fiber diameter by increasing the stretching and accelerating the polymer jet. Another parameter that affects the fiber diameter is the flight time of the polymer jet. The long flight time provides more time for the solvent to evaporate, hence thinner fiber formation can be observed. For this reason, the diameter of the fibers may increase up to a certain voltage value and then decrease [24]. It is possible to obtain fine fibers with optimum voltage value [1]. The effects of voltage on polymer jet formation and fiber diameter are shown in Figure 2.

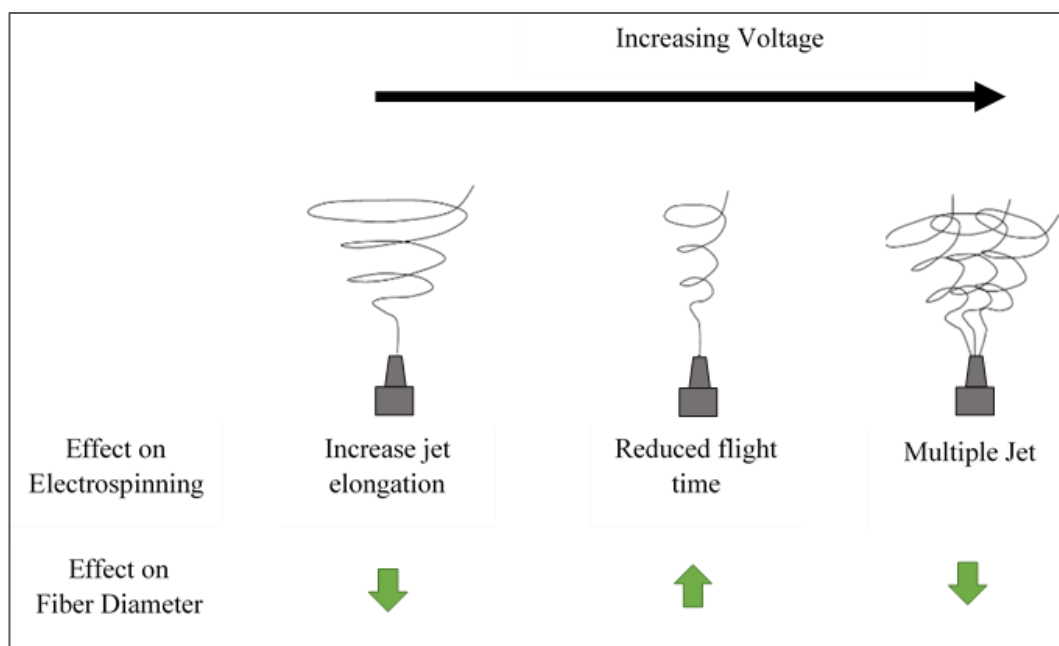


Figure 2. Effects of voltage on electrospinning and fiber diameter [25].

Uchko et al. [26] reported that the morphology of thin films produced by electrospinning is dependent on many process parameters including the applied voltage. As a result of this study, the reduction of the diameter of the fibers was achieved by increasing the applied voltage. Increasing the electric potential has increased the electrostatic tension that occurs in the polymer jet. This is shown as the reason for the faster pulling of fibers. Deitzel et al. [27] investigated the effects of

electrical potential and solution concentration on fiber morphology. It is stated that electric potential has an effect on bead formation. It has been observed that with increasing electrical potential, the shape of the surface of the polymer jet changes and stability decreases which causes bead formation. The concentration of the solution was found to be the most important parameter affecting the fiber diameter. With increasing solution concentration fiber diameter increased. This increase was related to the Power Law. Yördem et al. [28] found that electric potential is a parameter dependent on solution concentration and tip-to-collector distance. However, it is stated that the electric potential does not affect the diameter distribution of the nanofibers alone at high solution concentrations. These results show the interactions of the parameters.

2.2.2.2 Feed Rate

The feed rate should be determined for supplying the required materials to the electrospinning process. At the specified voltage, the feed rate value, which can generate an proper Taylor Cone, should be used [1]. Generally, the use of low feed rate values is preferred in order to provide the necessary time for the polymer solution to be polarized. If the feed rate is too high, the formation of beaded and thick fibers are observed. This is because of the increased volume and the lack of time to evaporate the solvent [12].

Fallahi et al. [29] investigated the effect of feed rate and solution conductivity on fiber diameter. SEM images were examined to understand the effects of these parameters on fiber diameter. As a result, the average fiber diameter did not change statistically with changes in the feed rate. In addition, the fiber diameter increased with increasing solution conductivity.

2.2.2.3 Tip to Collector Distance

Changing collector distance values directly affect the flight time and stretching magnitude. In order to produce uniform fibers, the time required for the solvent to evaporate from the polymer jet must be provided. When the tip-to-collector distance is reduced, the time spent for the polymer jet to reach the collector will be shortened. In addition, the electric field strength will increase as it is inversely proportional to the distance which will accelerate the polymer jet. As a result, there will not be enough

time to evaporate the solvent and high voltage will cause jet instabilities. For this reason, the fiber diameter decreases with increasing distance. However, stretching will decrease and fiber diameter will increase because the increased distance will cause the applied field strength to decrease. Even if the distance is too large, fiber formation will not be observed due to the insufficient stretching. Therefore, the smoothest and finest fibers can be produced at the optimized distance [1, 11].

Wang et al. [30] investigated the effect of collection distance on poly(phenylene vinylene) (PPV) fiber morphology. As a result of this study, bead formation was observed at low tip-to-collector distance values. In addition, very fine fiber formation was detected at high collection distance values. The reason for this is that sufficient time is provided for the evaporation of the solvent. In another study, Hekmati et al. [31] also investigated the effect of tip-to-collector distance on PA6 fiber morphology. Time for complete evaporation of the solvent is arranged by the collection distance. For this reason, 5, 10, 15 and 20 cm collection distance values were tried by keeping the other process parameters constant. It has been found that the fiber diameter increases considerably as the collection distance decreases. The decreasing collection distance, however, leads to an increase in the polydispersity of the average fiber diameters. The increase in fiber diameter with decreasing collecting distance is explained by the shortening of the bending time of the polymer jet from the needle tip. With increasing collecting distance, the polymer jet can be further twisted and the fiber diameter is reduced.

2.2.3 Ambient Parameters

The morphology of the nanofibers is known to be influenced by the ambient conditions, and these conditions are temperature and relative humidity. In a study, nanofibers were produced at 25, 50 and 75°C polymer solution temperatures to investigate the effect of temperature on morphology. When the results were analyzed, flat fiber formation was observed at 50 and 75°C. According to Koombhongse [15], during production polymer skin is formed and skin collapse under the influence of atmospheric pressure and solvent evaporation from the inside of fiber. High temperatures trigger skin formation and consequently ribbon-like fibers are formed

[32]. In another study, Poly(vinylidene fluoride) (PVDF) nanofibers were produced at different ambient temperatures. Only polymer drops were formed at low temperature (5°C). At low temperatures, the surface tension was increased and the voltage was not sufficient to overcome this value. As a result, bead formation was observed. Nanofibers were successfully produced at 15 °C. At 45°C, the formation of small beads was observed and this was explained by instable polymer jet at high temperatures. In addition, the average fiber diameter decreased with increasing ambient temperature [33].

In a study by Schoenmaker et al. [34], the effect of relative humidity on varying polymer concentration were investigated. Polyamide 4,6 (PA 4,6) and Polyamide 6,9 (PA 6,9) polymers were used for this purpose. It was observed that the different relative humidity values affected the structure of PA 4,6 more. This led to the conclusion that the affinity for water was higher in PA 4,6. At varying PA concentrations, fiber diameter decreased with increasing relative humidity. When water molecules are absorbed by the polymer jet, they act as plasticizers and cause thinning of the polymer jet.

2.3 Composite Nanofibers

Nanocomposites are one of the attracted research topics due to their improved mechanical property, dimensional stability, thermal stability and conductivity. They generally consist of two or more different compounds. At least one of these components must be nano-sized. Electrospinning process is widely used to produce polymer composite fibers. Since these nanocomposites possess both the advantages of the fibrous structure and composite, they are used in many applications [1, 35]. Figure 3 shows the application areas of the composite nanofibers that are currently used and predicted.

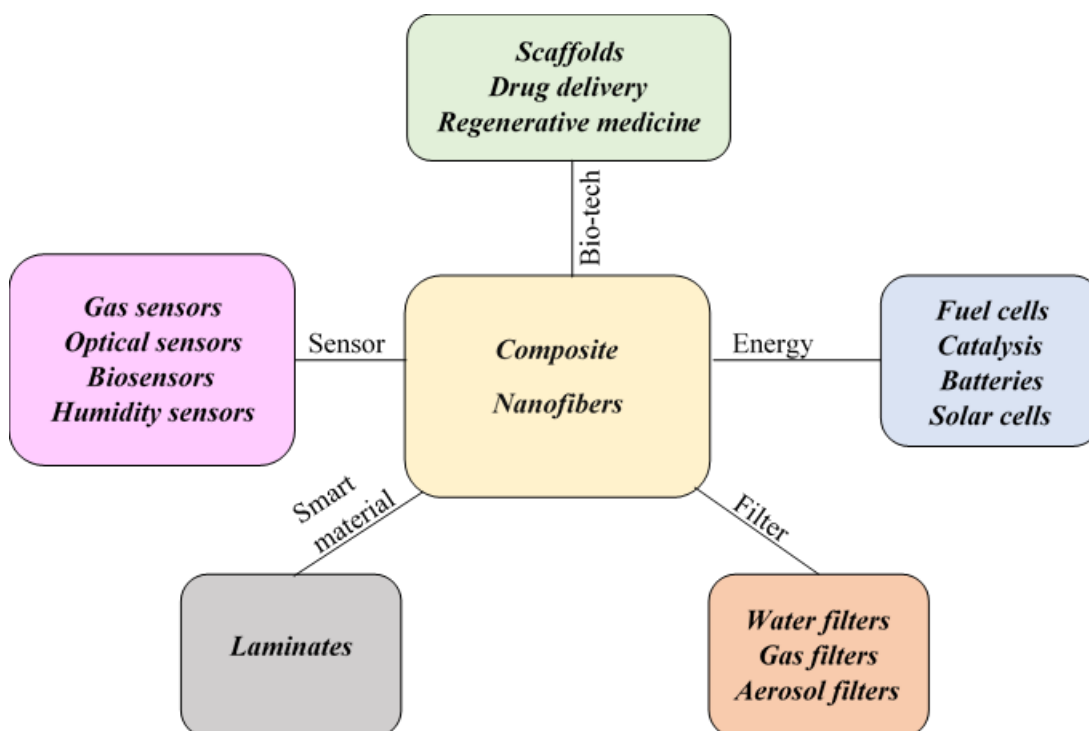


Figure 3. Applications of electrospun nanocomposites [35].

In addition to all the parametric studies about the fiber production mentioned above, studies on nanocomposite production by electrospinning method are also included in the literature. In a study conducted by Li et al. [36], the organically-modified montmorillonite (O-MMT)-added PA6 nanofibers were produced by the electrospinning method. The diameters of the fibers were found to be around 100 nm. The solution viscosity and morphology of the fibers changed after the addition of O-MMT. Characterization with Transmission Electron Microscopy (TEM) showed that the O-MMT separated into layers were oriented in the direction of the fiber axis. According to the results of mechanical characterization, the elastic modulus and tensile strength were increased by 70% and 30%, respectively, compared to the neat PA6 nanofibers. Jose et al. [37] successfully produced PA6 nanofibers with surface modified multi-walled carbon nanotubes (MWCNT). Characterization through Scanning Electron Microscope (SEM) showed that as the amount of MWCNT increased, the fiber diameter decreased. In addition, it has been found that mechanical properties increased as the amount of MWCNT increased. This is explained by the

strengthening of the polymer matrix by orienting the MWCNTs which have superior mechanical properties in the fiber.

There are a few studies in the literature on nanocomposite fibers produced using HNTs as additive material. Tao et al. [38] prepared polyglycolic acid (PGA)/HNTs composites by electrospinning method. It was found that HNTs significantly improves the mechanical properties of fibers. Zhilin et al. [39] produced poly(methylmethacrylate) (PMMA)/HNTs composite nanofiber prepared through electrospinning technique with improved mechanical properties. The diameter of the composite nanofibers was determined to be about 800 nm, and the fiber diameters were slightly changed with increasing HNTs content. The Fourier Transform Infrared Spectrophotometer (FTIR) results show that the spectra of the PMMA/HNTs composite nanofibers were similar and there is no difference compared to the neat PMMA nanofibers. In this work, it was demonstrated that the HNTs in the PMMA matrix were homogeneous and well dispersed. According to the results of differential scanning calorimetry (DSC) analysis, the glass transition temperature increased with the increasing amount of HNTs, which indicated thermal property of the produced nanocomposites improved with the addition of HNTs.

Xue et al. [40] investigated the properties of HNTs-added polycaprolactam (PCL) microfiber membranes and developed antibacterial properties with a sustained drug release profile of more than three weeks. The PCL ratio was selected as 6% by weight. The solution was dissolved in trifluoroethane, and the tip-to-collector distance was 20 cm, and voltage was 12 kV. Surface of HNTs was modified with (3-aminopropyl)triethoxysilane (APTES) silane coupling agent. It was observed that morphology of the fibers was not changed by incorporating HNTs to the structure. TEM analysis showed that the homogeneous distribution of HNTs in the fibers was achieved with the surface modification. Samples which were parallel and perpendicular to the collector rotation direction were cut from the produced membranes for mechanical test. They were wetted with deionized water to obtain similar conditions with usage area of wet state membranes. When the results were compared, the samples cut which were parallel to the collector rotation direction had a tensile strength twice greater than the other samples. Among the prepared specimens,

the highest mechanical test results were obtained as the tensile strength of 16 ± 0.9 MPa and the elongation values of $85.4 \pm 13.3\%$ for the specimens prepared with the addition of 5 wt.% HNTs. Mechanical properties decreased with increasing amount of HNTs.

In a study conducted by Wang et al. [41], it was aimed to develop and analyze the multifunctional properties of films produced by electrospinning method. The properties to be investigated were controlled drug delivery in wound healing and inhibition of bacterial growth. As a result of this study, biocompatible polycaprolactone and chitosan hybrid electrospun fibers were produced and it was concluded that the fibers could be successfully used in drug delivery and bacterial growth inhibition. In another study conducted by Moon and Lee [42], poly(ethylene oxide) (PEO)/hydrated iron oxide (HIO)/sodium alginate (SA) composite nanofibers were produced by electrospinning method and it was aimed to develop multifunctional properties. As a result of the study, nanofibers with antibacterial and good mechanical (31.6 ± 0.4 MPa tensile strength) properties were produced. It has been emphasized that these nanofibers are suitable for use in the fields such as biomedical, food, environmental, protective equipment, composite industries etc. due to their multifunctional properties.

2.4 Degradation Properties of Nanofibers

Degradation properties of plastics under certain conditions is one of the important research topics that causes a change in the physical and chemical structure of the polymers. Changes in polymer structure under heat, light, air and chemical environments is important for industries such as medicine, textile, membrane separation and food packaging [43]. In order to reduce the effects of these aggressive environments and to improve the mechanical properties, nanocomposite materials can be used [44].

There are studies in the literature which investigate the degradation properties of polyamides and polyamide composite materials. Boulton and Jackson [45] reported that polyamide was degraded when exposed to sulfuric acid, ultraviolet light and sunlight. Viscosity measurement and tensile tests were carried out after the chemical

degradation and at the end of these measurements; a small decrease in viscosity and a reduction of 50% in tensile strength were observed. Shelley et al. [46] investigated the effects of clay addition to the PA6 matrix. Tensile test, infrared spectroscopy, dynamic mechanical analysis and chemical degradation test with a harmful gas (NO_x) were used for the characterization. As a result of the study, an improvement of 200% in tensile modulus and 175% in tensile strength was obtained with the 5% clay addition. Reduction of tensile modulus and strength was observed after the samples were exposed to NO_x gas.

Abastari et al. [47] investigated the permeability properties of PA66 in sulfuric acid solution and the relationship between permeability and chemical degradation for polymeric materials. Permeability, diffusion and chemical degradation tests were applied to the samples in the different concentrations of sulfuric acid solutions. A mathematical relationship was established between diffusion rate and molecular weight as a result of the change in weight average molecular weight. Makaremi et al. [48] used HNTs as a reinforcing material to improve the mechanical properties, thermal resistance and water filtration performance of electrospun polyacrylonitrile (PAN) nanofiber membranes. When the mechanical properties of HNTs-loaded specimens were investigated, improvement in tensile strength and elongation were found. In addition, significant improvements have been observed in thermal properties. The PAN/HNTs membranes were tested for their water filtration capability. The hollow structure of HNTs increased the surface area of the membrane, and increase in HNTs concentration increased the water permeability, which indicated that HNTs-loaded nanofibers were suitable for use in water filtration technologies. Ghanbari et al. [49] applied filtration tests on HNTs-loaded polysulfone nanocomposite membranes. In their study, the hydrophilic nature of HNTs increased water permeability and facilitated the entrance of water through the membrane. Furthermore, it was reported that the hollow structure of HNTs allowed water molecules to penetrate into the nano-structure.

Gonçalves et al. [50] examined the degradation mechanism of pressed PA66 films. For this reason, prepared films were immersed in water at temperatures ranging from 25-90° C and degradation was characterized by FTIR and solid-state NMR spectroscopy.

As a result of the degradation, molecular oxygen and radical intermediates were formed, and degradation proceeded by imide formation. It has been stated that PA66 degradation in water is thermo-oxidative and this process is facilitated by an increase in flexibility of the polymer matrix through interaction with water.

2.4.1 Diffusion Theory in Polymers

Solvent absorption rates of polymers and nanocomposites can be shown by calculating the diffusion coefficient. The Fick's second law of diffusion (Equation 2.1) explains the accumulation of the solvent in the sample depending on the time and the diffusion coefficient (D).

$$\frac{\partial C}{\partial t} = \frac{\partial}{\partial x} \left(D \frac{\partial C}{\partial x} \right) \quad (2.1)$$

Equation 2.1 shows the one-dimensional (x-direction) concentration change as a function of time. After mathematical treatments of kinetic data, diffusion coefficient is obtained. Crank (1975) developed a solution for diffusion coefficient and Equation 2.2 is obtained [51].

$$\frac{C_t}{C_\infty} = 1 - \frac{4}{\pi} \sum_{n=0}^{\infty} \frac{(-1)^n}{2n+1} \exp\left(\frac{-D(2n+1)^2 \pi^2 t}{4l^2}\right) \cos\left(\frac{(2n+1)\pi x}{2l}\right) \quad (2.2)$$

In Equation 2.2, C_t is concentration at time t , C_∞ is equilibrium concentration and $2l$ is the film thickness. Integrating Equation 2.2 gives Equation 2.3, where M_t is percent weight change (%) at time t and M_∞ is percent weight change (%) at equilibrium.

$$\frac{M_t}{M_\infty} = 1 - \sum_{n=0}^{\infty} \frac{8}{(2n+1)^2 \pi^2} \exp\left(\frac{-D(2n+1)^2 \pi^2 t}{4l^2}\right) \quad (2.3)$$

Equation 2.3 can be rearranged for short times and gives Equation 2.4.

$$\frac{M_t}{M_\infty} = 2 \left(\frac{D}{\pi l^2} \right)^{1/2} t^{1/2} \quad (2.4)$$

When M_t/M_∞ is drawn with respect to $t^{1/2}$, slope of the graph gives the diffusion coefficient. The ratio of M_t/M_∞ should be lower than 0.5 for linear relationship with time [44, 52].

Diffusion constant calculation can be made by using the results of chemical degradation experiments. In this direction, Preda et al. [53] studied the diffusion mechanisms of water vapor in polyamide 6,6 (PA66) and polyamide 6,10 polymers. In the study, it was observed that the water vapor did not follow the Fick's Law of the diffusion into polyamide 6,10, while the polyamide 6,6 had a mass transfer mechanism that conformed to the Fick's Law. In the work of Abacha et al.[44], the organoclay material (montmorillonite) was added to PA6 by melt mixing method and the diffusion of water vapor in the nanocomposite material at different temperatures was investigated. In addition, influence of water held by PA6 on the size, mechanical, and surface properties were investigated. As a result of the study, diffusion coefficient with organoclay addition decreased. The weight change increased with the amount of organoclay but did not exceed the weight change of the neat PA6. Also, organoclays were well dispersed in PA6 matrix and therefore higher mechanical properties were obtained with the addition of organoclay. However, mechanical properties were decreased significantly with water interaction. It was stated that the water held in the structure acted as a plasticizer and reduced the glass transition temperature, tensile modulus and yield stress of the material.

2.5 The Scope of the Thesis

Electrospinning is an efficient method in production of nanofiber mats when compared with other nanofiber fabrication processes. Nanofibers produced using this method have excellent properties such as high ratio of surface area/volume, high porosity, and superior mechanical properties.

PA6 is an engineering thermoplastic which has a high fiber forming ability with good mechanical properties. HNTs are very attractive natural nanomaterials, which can be used to prepare nanocomposites with high performance and they are inexpensive compared to other nanofillers such as carbon nanotubes (CNTs).

As a result of the literature survey, it is seen that there is a research gap in the use of HNTs and PA6 together as component of composite nanofibers prepared through electrospinning method. It is thought that the PA6/HNTs composite nanofibers is an exciting area for research purposes due to great application potential of HNTs and improved properties of PA6. In addition, the ability to dissolve PA6 in formic acid or a mixture of formic acid and acetic acid for use in the electrospinning process is advantageous compared to other solvents which are much more harmful to environment.

In this thesis, a comprehensive optimization study covering the production of neat PA6 fibers was performed and the effect of process parameters on the nanofiber structure was investigated. HNTs-added PA6 composite nanofibers were then produced and characterized in terms of morphology, mechanical, thermal, flame retardant and degradation properties. The degradation behaviour of the composite nanofiber mats, which is another original part of the study, was also investigated under four different chemical vapors, namely HCl, acetone, toluene and water. Results of the degradation tests for the fibers can give information about the usage areas and their lifetimes. In addition to these, the flame retardant property of some selected nanofiber mats were determined through LOI test which is not available in literature for PA6 electrospun mat according to the best of our knowledge.

CHAPTER 3

EXPERIMENTAL

3.1 Materials

3.1.1 Polyamide-6 (PA6)

Commercial grade Polyamide, PA6 (Tecomid NB40) was supplied by Eurotec Engineering Plastics. The specifications for the material are given in Table 1.

Table 1. The properties of PA6 [54].

Properties	Value
Density (g/cm ³)	1.13
Melting Temperature (°C)	223
Processing Temperature (°C)	240-260
Color	Natural
Moisture Absorption (%) (50% RH, 23 °C)	3

3.1.2 Halloysite Nanotubes (HNTs)

Halloysite Nanotubes (HNTs) with $\text{Al}_2\text{Si}_2\text{O}_5(\text{OH})_4 \cdot 2\text{H}_2\text{O}$ formulation was purchased from Sigma-Aldrich (685445) and used as reinforcement. The physical properties of HNTs are given in Table 2.

Table 2. Physical properties of HNTs [55].

Property	Value
Average Diameter (nm)	30-70
Length (μm)	1-3
Surface Area (m ² /g)	64
Color	White

3.1.3 Solvents and Other Chemicals

Formic acid (Sigma-Aldrich) with 98-100% purity and acetic acid (Riedel-de Haen) with 100% purity were used as solvents in the electrospinning process. There is almost no water in the solvents used. (3-aminopropyl)triethoxysilane (APTES) 99% (Sigma-Aldrich) was used in surface modification of HNTs due to compatibility with the polymer and HNTs. Hydrochloric acid (fuming 37%, Merck), acetone (Merck), toluene (Merck) and deionized water were used for the chemical degradation tests.

3.2 Experimental Procedure

3.2.1 Preparation of Polymer Solution

PA6 is a polar polymer according to its chemical structure and can easily absorb moisture from environment. It is therefore necessary to dry the material as specified in the technical data sheet (at least 2 hours at 80°C) [54]. To provide polymer granules with the same conditions and to make them ready to use, the granules were dried at 80 °C under vacuum until there was no change in weight. The dried polymer granules were dissolved in the solvent such that the solution concentration was 15% by weight. Mixture of formic acid and acetic acid (4:1 volume) was used as solvent. To obtain a homogeneous mixture, the prepared solution was mixed with magnetic stirrer (Velp Scientifica, Arex heating magnetic) for 4 hours at 50°C. After obtaining the homogeneous solution, the mixture was cooled to room temperature.

3.2.2 Surface Modification of Halloysite Nanotubes

HNTs were dried under vacuum at 110°C until the weight change was not observed. 200 g of 80 vol.% ethanol-water mixture was prepared as a solvent. The pH of the mixture was adjusted to 3.25 by adding small amount of acetic acid. The mixture was placed in an ultrasonic bath where its temperature was kept constant at 70°C. APTES was used as silane coupling agent and added as 1 wt.% of the mixture. Mechanical and ultrasonic mixing was applied for 30 minutes in order to completely hydrolyze the alkoxy groups. After adding 5 grams of dried HNTs, mechanical and ultrasonic mixing was continued for 4 hours. The mixture was then filtered through a Buchner funnel and filter paper, the modified HNTs were washed with a 300 mL 80 vol.% ethanol-

water mixture and the dried at 110 °C for 3 hours under vacuum. The schematic representation of the procedure is given in Figure 4. After modification, FTIR analyses were performed to understand the differences between unmodified and modified HNTs and results are given in Appendix A [56].

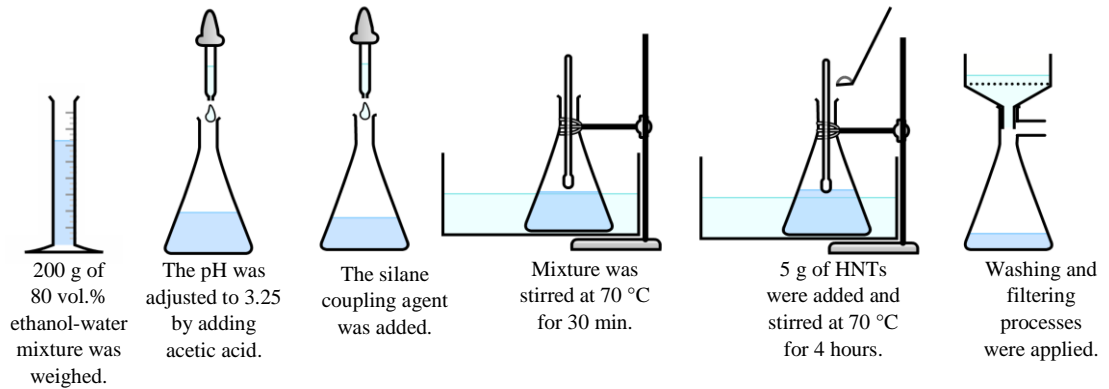


Figure 4. Experimental procedure of surface modification of HNTs.

3.2.3 Preparation of Composite Solution

In order to prepare the composite solution, first the amount of solvent to be used was determined. Two equations were then formulated and solved together to determine the desired PA6 concentration and HNTs content of 1, 2, 4, 6 and 8% relative to the amount of PA6. The equations are given below.

$$\text{PA6 Concentration (wt.\%)} = \frac{m_{\text{PA6}}}{m_{\text{solvent}} + m_{\text{PA6}} + m_{\text{HNTs}}} \times 100 \quad (3.1)$$

$$\text{HNTs Concentration (wt.\%)} = \frac{m_{\text{HNTs}}}{m_{\text{PA6}} + m_{\text{HNTs}}} \times 100 \quad (3.2)$$

Firstly, HNTs with the determined amount were added to FA and AA mixture to obtain 1, 2, 4, 6 and 8 wt.% composites. Then this suspension was sonicated using a Bandelin Sonorex RK 100 sonicator for 30 minutes in order to get better dispersion. The PA6 pellets were added and mixed with magnetic stirrer for 4 hours to obtain a

homogeneous mixture. For each additive amount, two sets of experiments were carried out, which included unmodified and modified HNTs. The schematic representation of the procedure is given in Figure 5.

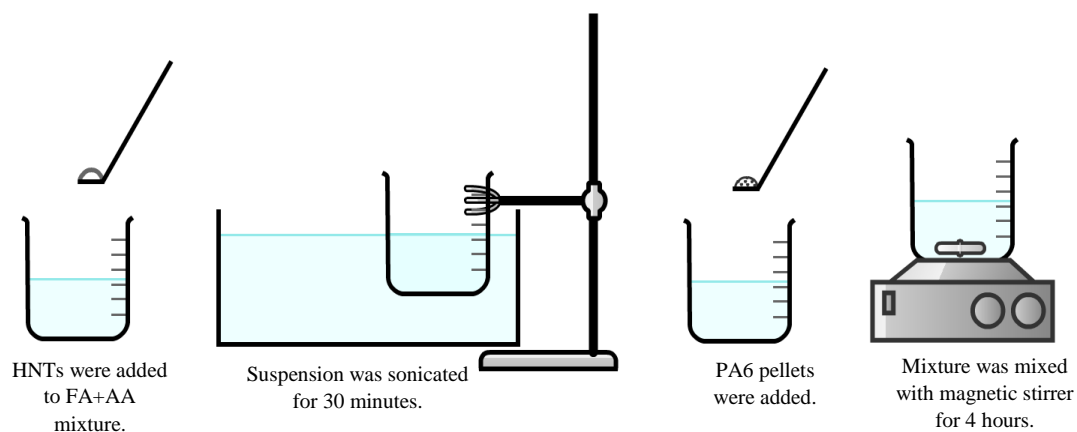


Figure 5. Experimental procedure for the preparation of composite solution.

3.1.1 Electrospinning Process

Electrospinning was performed using an Inovenso Ne 300 electrospinning equipment (see Figure 6) which is a multi-needle laboratory scale device capable of nanofiber production and homogeneous nanofiber coating on the cylinder or plate surfaces. Technical information of the device is given in Table 3. All the experimental parameters of the polymer and the composite production are given in Table 4. The experiments for the optimization purposes were performed at room temperature ($23 \pm 2^\circ\text{C}$) and relative humidity ($45 \pm 10\%$) in the laboratory conditions.



Figure 6. Inovenso Ne 300 electrospinning device.

Table 3. Technical information of the Inovenso Ne 300 electrospinning device [57].

Property	Value
Voltage range (kV)	0-40
Feed rate range (mL/h)	0.01-1000
Needle diameter (mm)	0.8
Collector Types	Rotating cylinder or constant plate
Cylinder Dimensions (diameter × length)	100 mm × 220 mm
Material of collector	Aluminum

The parameters optimized in this study are voltage, feed rate and tip-to-collector distance. The limits of each parameter in the device, which are 0-40 kV for the voltage, 0.01-1000 mL/h for the feed rate and 45-245 mm for the tip-to-collector distance were taken into account when optimizing these parameters.

Table 4. Parameters of the electrospinning process.

	Variables	Fixed Parameters
Solution Concentration (wt.%)	10, 15, 20, 30	30 kV, 0.3 mL/h, 10 cm, FA
Solvent Type	(FA+AA; 4/1)	
Solution Concentration (wt.%)	10, 15, 20, 30 wt.%	30 kV, 0.3 mL/h, 10 cm
Applied Voltage (kV)	15, 20, 25, 30, 35, 40	15 wt.%, 0.3 mL/h, 10 cm, FA+AA, 200 rpm
Feed Rate (mL/h)	0.1, 0.2, 0.25, 0.3, 0.33, 0.35, 0.4	15 wt.%, 30 kV, 10 cm, FA+AA, 200 rpm
Tip-to-Collector Distance (cm)	5, 7, 9, 10, 12, 15	15 wt.%, 30 kV, 0.33 mL/h, FA+AA, 200 rpm
HNTs Concentration (wt.%)	1, 2, 4, 6, 8 un-HNTs 1, 2, 4, 6, 8 m-HNTs	15 wt.%, 30 kV, 0.30 mL/h, 10 cm, FA+AA, 200 rpm

3.3 Characterization Methods

3.3.1 Viscosity Measurement

The viscosities of the polymer solutions prepared for electrospinning were measured with a CANNON 2020 rotational viscometer. 100 mL solutions were prepared for each concentration (10, 15, 20 and 30 wt.% PA6) and viscosities were measured using the a spindle. During the measurements, torque (%) values were read between 10 and 100.

3.3.2 Scanning Electron Microscopy (SEM) Analysis

A QUANTA 400 F Field Emission high resolution Scanning Electron Microscope in METU Central Laboratory was used to determine the morphology of the produced nanofibers. The nanofibers collected on the aluminum foil were cut in 1x1 cm² dimensions and were adhered to the carbon band. The samples were coated with gold-palladium alloy to provide conductivity. The average diameters of the fibers were measured with ImageJ2 (Fiji) (NIH, USA) software. For each sample, diameters of 100 nanofibers were measured and the distribution plots were drawn.

3.3.3 Transmission Electron Microscopy (TEM) Analysis

A FEI brand Tecnai G2 Spirit Biotwin high contrast Transmission Electron Microscope (CTEM) in METU Central Laboratory was used at an acceleration voltage of 120 kV. To prepare the samples, 400 mesh cooper grid was placed onto the collector as target. Electrospinning was performed for 2-3 seconds. For the samples exposed to chemical vapors, the nanofiber mats were embedded into EPON 812 (epoxy resin) and polymerized at 60 °C for 30 hours in the bar shape mould. First bar-shaped block was cut to receive the section which was placed in the block holder. Secondly, block holder was placed in the microtome device (model, marka). The surface of the sample was smoothed with the help of a glass knife. Finally, the desired section was cut with diamond blade (Struers Accutom 50) floated on water pool and placed on carbon coated grids.

3.3.4 Fourier Transformed Infrared (FTIR) Spectroscopy

A Perkin Elmer FTIR-ATR instrument was used to determine the changes in structure of the nanofibers after chemical vapor exposure, in the range of 500-4000 cm^{-1} wavenumbers.

3.3.5 Thermogravimetric Analysis (TGA)

Thermogravimetric analyses (TGA) were performed with a Shimadzu DTG-60 instrument. Neat and composite nanofiber samples were heated from 25°C to 800°C at 10°C/min under N₂ flow (500 ml/min).

3.3.6 Differential Scanning Calorimetry (DSC) Analysis

Differential scanning calorimetry (DSC) analysis of the produced nanofibers was carried out from 25°C to 300°C with a 10°C/min heating rate under N₂ atmosphere using a Shimadzu DSC-60A differential scanning calorimeter. Approximately 5 mg of samples were bent into a standard DSC aluminum pans and results were analyzed after first run. The degree of crystallinity values were calculated with using the Equation 3.3.

$$X_c = \frac{\Delta H_f^m}{\Delta H_f^o} \times 100 \quad (3.3)$$

where X_c is degree of crystallinity (%), ΔH_f^m is heat of fusion (J/g), ΔH_f^o is heat of fusion for 100% crystalline polymer (190.6 J/g for PA6 [58]).

3.3.7 Tensile Test

The tensile test to determine the mechanical properties was performed on a Shimadzu Autograph AG-IS 100kN universal tensile test machine. Figure 4 shows a photograph of the tensile testing device.



Figure 7. Shimadzu Autograph AG-IS 100kN universal tensile test machine.

Tensile tests for the fiber mats were made in accordance with ASTM D882-02 standard. The mat had the length of 50 mm, the gauge length of 30 mm, the width of 10 mm and the thickness of 40-100 μm . The thicknesses of the samples were measured with a micrometer (Micromar Micrometer 40 EWR) with a resolution of 0.0001 mm. The crosshead speed was set to 15 mm/min according to the size of the sample which is specified in the standard. For each additive concentration, five measurements were

made and the results were reported by taking the average and standard deviations of these results. In order to remove the samples collected on the aluminum foil without damaging, sample sizes were drawn on A4 paper first. Then a 10×10 mm² double-sided tape was affixed to clamped points of the sample. The other side of the double-sided tape was then affixed to the sample. After this step, the sample and the pasted paper were cut together and the aluminum foil was carefully peeled off. Sample preparation method and samples prepared using this technique are shown in Figure 8.

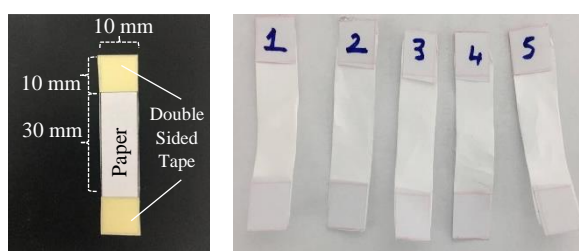


Figure 8. Specimen dimensions and the shape of the tensile test specimens.

3.3.8 Limiting Oxygen Index Test

Limiting oxygen index test for the nanofiber mat of the study was performed according to ASTM D2863-06a standard. Several attempts have been made to select the suitable type in the standard for thin films. Firstly, type VI (self-supporting when rolled) was tried for thin films. For this, a stainless steel rod with 20 cm length and 2 mm diameter was used. Nanofiber mats were wrapped around the bar at a 45° angle as specified in the standard. The release paper was used to separate the mat from the bar without damage. As a result of these experiments, it has been found that the nanofiber mats are not self-supporting.

As an alternative to this method, specimens were produced in sizes of 40 mm width, 140 mm length which was the same as the frame of the LOI equipment. Due to the large width of the samples, the path of the flame was not vertical through the length of the sample as required. In order to solve this problem, a frame with a width of 10 mm shown in Figure 9 was used. The specimens with 60 mm length and 10 mm width were

cut to fit the prepared frame and the first 50 mm sections were marked. The LOI value required for complete burning of 50 mm of these samples was reported to be the LOI value. LOI samples were taken from the middle part of the produced mats where dimensional homogeneity is expected to be maximum to minimize the effect of thickness differences. In addition, samples with the same geometry as the electrospun mat were produced using a twin-screw extruder (Thermoprism TSE-16-TC (L/D=24)) and a compression molding machine. After the extrusion, the 3 grams of the sample was preheated for 5 minutes at 270 °C in an aluminum foil with dimensions of 22x22 cm² in the compression molding device. It was held at the same temperature for 4 minutes under 200 bar pressure. These films were cut in the dimensions specified above for the LOI test (60x10 cm).



Figure 9. Frame with a width of 1 cm and test setup for the LOI test.

3.3.9 Degradation of Electrospun Mats under Chemical Vapors

After optimization studies (solution concentration, solvent type, HNTs additive amount, voltage, feed rate and distance optimization), neat, 1 and 8 wt.% m-HNTs containing nanofiber mats were selected in order to expose them to hydrochloric acid, acetone, toluene and water vapors. These experiments were performed on ten specimens for each sample. Water and toluene were used in pure form, acetone in 50% by volume and hydrochloric acid in 10% by weight of aqueous mixture.

In order to perform the chemical vapor degradation test, desiccators with 24 cm diameter were filled with 900 mL different chemicals which were mentioned above. Before the produced nanofibers were put into the desiccators, they were weighed using a Precisa XB 220A with a precision of 0.0001 grams scale. The sample holder in the desiccator was designed so that the samples were not in contact with any liquid solvent while being hanged up to 15 cm above via clips. The first setup can be seen in Figure 10(a) and (b). The specimens were weighed routinely at pre-determined time intervals. To prevent any solvent loss from the desiccator due to vaporization during the weighing operation, the solvent was always kept at 900 mL by the addition of the lost solvent. In the first two weeks of the experiment, three weights a day was done, but later this procedure was dropped down to a single weight measurement per day. In order to keep the temperature in the desiccator constant at 25°C, air conditioner was used throughout the experiment. The closet where desiccators were kept was insulated with glass wool covered with aluminum sheets. During the experiments, temperature and humidity values in the desiccators were maintained via manual hygrometers and monitored via digital hygrometer at 25 °C and 90 %, respectively.

The usage of the experimental setup was terminated after a month due to the fast oxidation rate of the clips under HCl acid vapor. On the other hand, the complications were not observed for toluene, acetone and water vapor and the measurements were continued for two months.

With the purpose of the preventing any problem due to oxidation, the experiments was repeated with a new setup in which no clips were used and sample holder was made out of glass grid. The redesigned experimental setup can be seen in Figure 10(c). In the experiment with new setup, weighing was done every half an hour for the first 4 hours then it was done hourly in the first day. After the weight change was observed to be reduced, the weight measurements were done regularly with 3 hours intervals in a day. The measurements were completed after 7 days.



Figure 10. (a) Sample holder of the old setup (b) desiccator where the experiments are carried out with the first setup (c) new setup with glass grid.

CHAPTER 4

RESULTS AND DISCUSSION

4.1 Parameter Study of Electrospinning

The main parameters used in electrospinning process are solution concentration, solvent type, voltage, feed rate and the tip-to-collector distance. In order to produce smooth, continuous and non-beaded nanofibers, these parameters have to be optimized. In the preliminary experiments, many attempts have been made to learn the electrospinning process and to produce a smooth nanofiber. After these experiments, parametric studies were performed.

4.1.1 Solution Concentration Optimization

In solution concentration optimization, different concentration values were tried by keeping the voltage, feed rate and the tip-to-collector distance values constant. 10, 15, 20 and 30 wt.% PA6 solutions were prepared in order to determine the limits of the electrospinning process. 30 kV voltage, 0.3 mL/h feed rate and 10 cm tip-to-collector distance values were chosen to produce nanofiber. Only formic acid was used as solvent during these experiments.

The viscosity measurement was conducted to characterize the prepared solutions. The results of 10, 15 and 20 wt.% polymer solutions are given in Table 5. The viscosity of 30 wt.% of the solution was not measured because the viscosity was outside the measurement limits of the device. When the results are analyzed, it is observed that viscosity increases with increasing polymer concentration as expected [17, 59].

Table 5. Viscosity results of 10, 15 and 20 wt.% polymer solutions.

Sample	Viscosity (cP)
10 wt.%	195
15 wt.%	480
20 wt.%	640

Polymer jet formed at the tip of the needle during the production of 10 wt.% of solution exhibited an unstable behavior, and this behavior led to the formation of more than one polymer jet. During the production of the 30 and 20 wt.% solutions, the fiber production were not continuous and the solvent at the needle tip accumulated and the tip was blocked due to the rapid evaporation of the solvent used. In the 15 wt. % solution, Taylor cone was properly formed, but the electrospinning process did not reach steady-state.

SEM analysis is used to understand the fiber morphology and average fiber diameter. SEM micrographs of 10, 15, 20 and 30 wt.% concentrations are given at 20,000 magnification in Figure 11 (a), (b), (c) and (d).

Figure 11 (a) shows SEM micrographs of nanofibers produced with 10 wt.% concentration. At this concentration it was determined that fiber diameters were between 50 and 100 nm and beaded fibers were formed. The formation of fine and beaded fibers can be explained as a result of the increased ability of the polymer chains to move at low concentrations and thus to higher stretching of the polymer jet [18]. Figure 11 (b) shows SEM micrographs of nanofibers produced with 15 wt.% concentration. Fiber diameters were increased compared to the 10 wt.% solution concentration and non-beaded fiber formation was observed. Figures 11 (c) and (d) show the SEM micrographs of 20 and 30 wt.% solution concentrations respectively. There is significant increase in fiber diameters produced with 30 wt.% concentration. The formation of thicker fibers can be explained by the more chain entanglements, which caused the less chain mobility. The reduction in chain mobility results in less stretching of the polymer jet. Thus thicker fibers were formed [14].

In addition, formation of ribbon-shaped fibers was observed at high concentrations (20 and 30 wt.%). Due to the fast evaporation of the scarce solvent, a skin was formed on the surface of the polymer jet. This skin causes to form hollow fiber [60]. Atmospheric pressure and cohesive forces lead to collapse these hollow fibers during solvent evaporation [61]. As a result, ribbon-shaped fibers were formed [36].

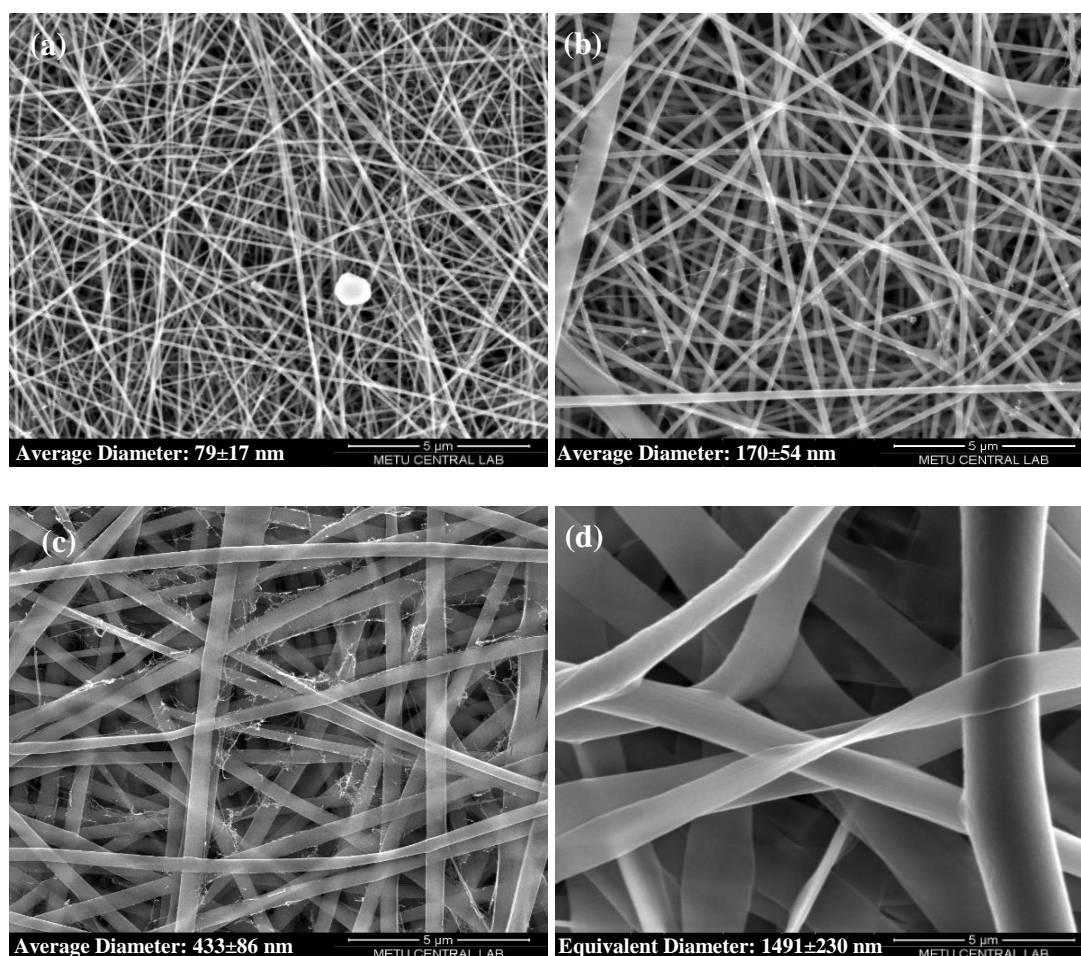


Figure 11. SEM micrograph of the fibers produced with (a) 10, (b) 15, (c) 20, (d) 30 wt.% PA6 solutions.

Figure 12 shows the cumulative frequency of fiber diameters of nanofibers produced with different solution concentrations. Fiber diameters significantly increased with increasing solution concentration. Narrower distributed fiber diameter was observed at lower solution concentrations. Moreover, 30 wt.% PA6 solution concentration yielded larger spread of diameter than the other concentrations.

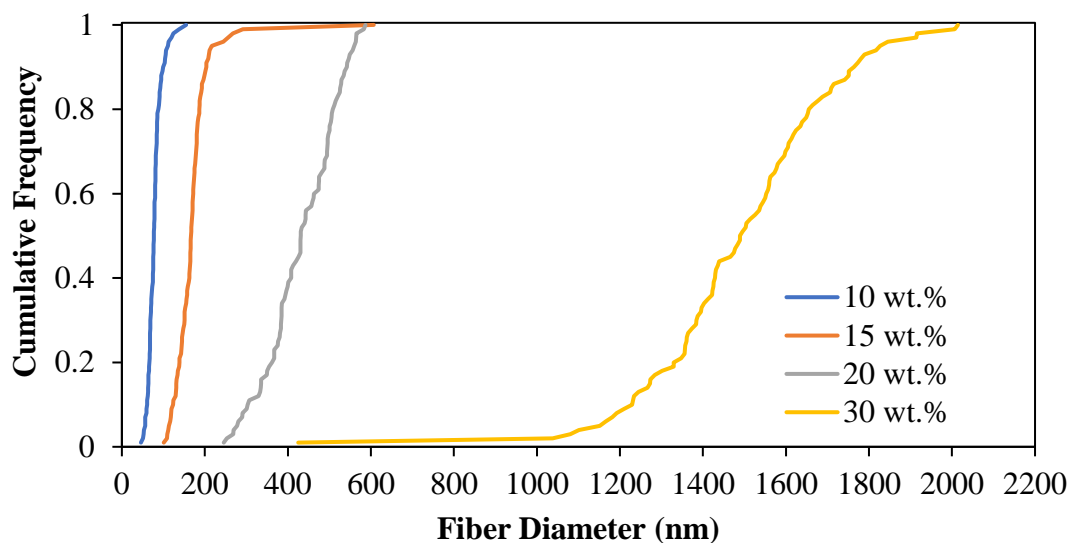


Figure 12. Cumulative frequency of fiber diameters of the nanofibers produced with different solution concentrations.

4.1.2 Solvent Type and Concentration Optimization

After the concentration optimization, electrospinning equipment was learned and different solution concentrations which could be used in the production of nanofibers were tried. As a result of these experiments, it was concluded that the solution concentration is an important parameter affecting the fiber morphology. The results obtained at this stage were considered and evaluated in the other parameter optimizations.

The correct solvent mixture must be used in order to obtain steady-state electrospinning process [59]. To obtain stable Taylor cone, formic acid (FA) and acetic acid (AA) (4:1) solution mixture was used. PA6 nanofibers were produced by changing the solvent type were characterized by SEM, and SEM micrographs are given in Figures 13 (a), (b), (c) and (d). SEM photographs showed that the fiber diameters increased significantly with increasing solution concentration as explained in solution concentration optimization. In addition, according to observations made during the experiments, using a mixture of formic acid and acetic acid as solvent provided a steady-state electrospinning process. FA has high dielectric constant, which cause increase in polarity, and increased polarity causes the Taylor cone to become

unstable. Addition of AA, that has lower dielectric constant provided to form stable Taylor cone. Moreover, surface tension of polymer solution decreases with the addition of AA. The reduced surface tension ensures stable Taylor cone formation at low polymer concentrations [59]. When selecting the acetic acid ratio, it has been taken into account that acetic acid does not dissolve PA6. In summary, using a mixture of formic acid and acetic acid (4/1) as a solvent facilitates the process to achieve steady state electrospinning. The optimum solution concentration for HNT addition was selected as 15 wt.% PA6 in FA and AA mixture because the finest fibers could be produced continuously in this concentration.

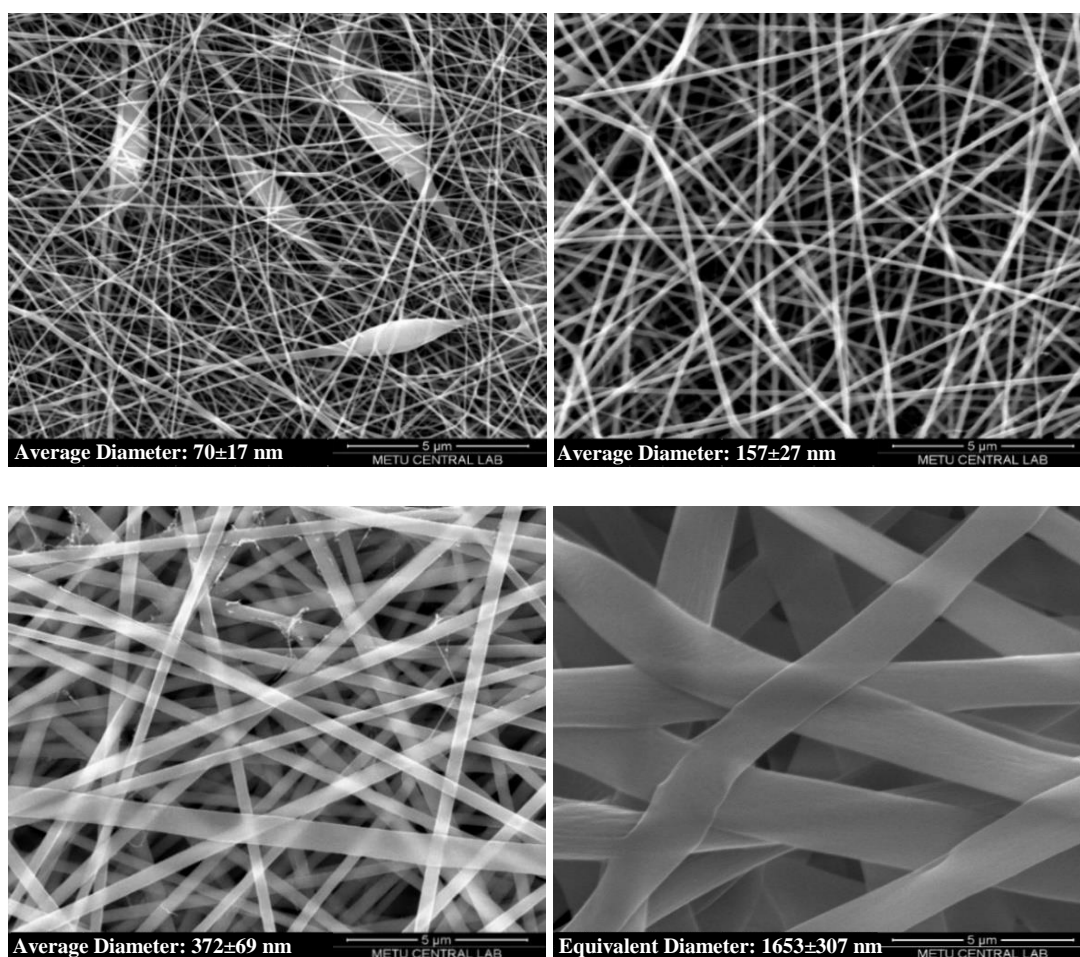


Figure 13. SEM micrograph of the fibers produced with (a) 10, (b) 15, (c) 20, (d) 30 wt.% PA6 solutions in FA and AA solvent mixture.

Figure 14 shows the cumulative frequency of fiber diameters of nanofibers produced with different solution concentrations in FA and AA solvent mixture. Fiber diameters again significantly increased with increasing solution concentration. Higher solution concentration led to less uniform fibers and broader distribution of their diameters.

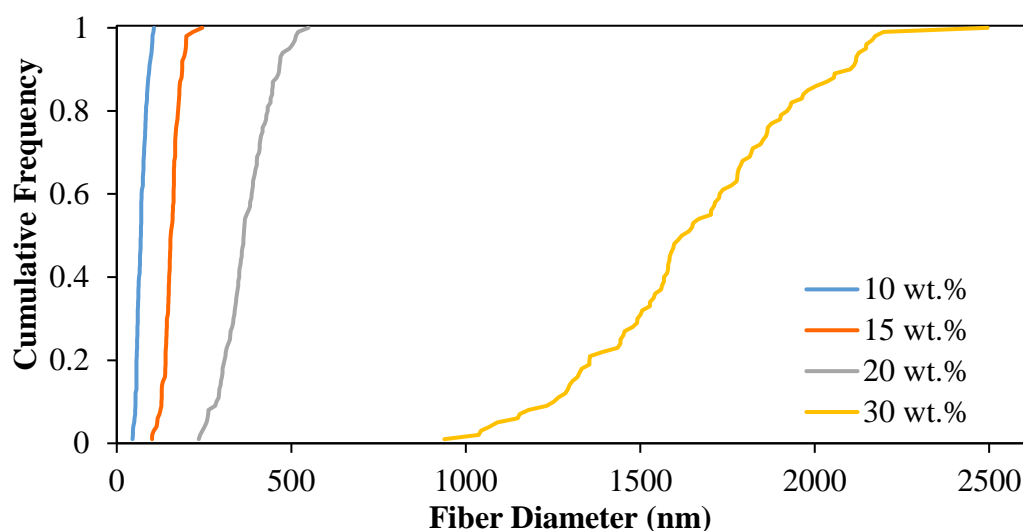


Figure 14. Cumulative frequency of fiber diameters of the nanofibers produced with different solution concentrations (FA and AA solvent mixture).

Optimization studies on both the solution concentration and the solvent type and optimization experiments resulted in very fine fibers formed around the main fibers. Examples of these fibers are shown in Figure 15. These can occur due to the solvent used in the electrospinning process. Formic acid is a highly polar solvent and causes partial ionization of amide groups of PA6. This results in increased conductivity and very fine fiber formation [62].

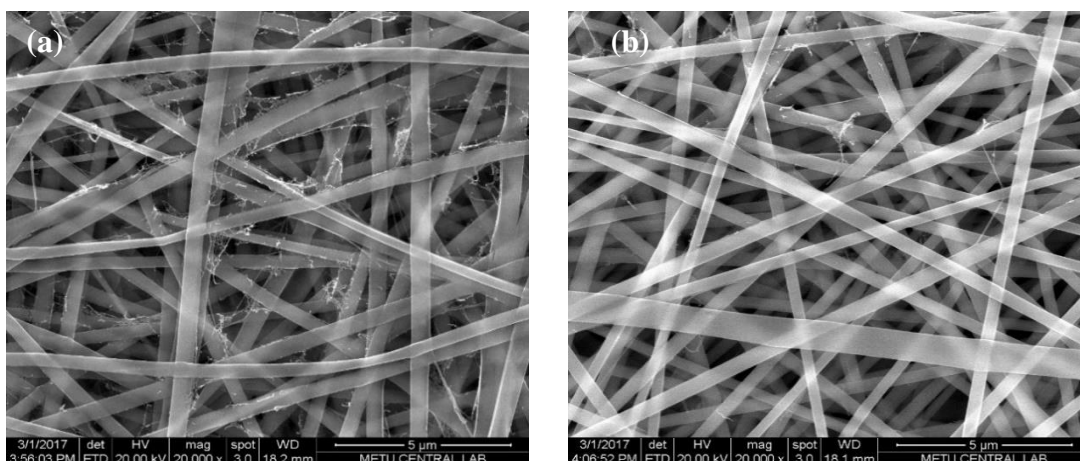


Figure 15. (a) SEM micrograph of fibers produced with 20 wt.% PA6 solution (FA); (b) SEM micrograph of the fibers produced with 20 wt.% PA6 solution (FA and AA mixture).

4.1.3 Voltage Optimization

After the appropriate solution and solvent concentration values were determined, the voltage value was optimized. In the voltage optimization, all the other parameters (15 wt.% solution concentration, 0.3 mL/h feed rate and 10 cm distance) were kept constant and 15, 20, 25, 30, 35 and 40 kV values were tried. In addition to SEM analysis that is used in the solution parameter optimizations (solution concentration and solvent type), TGA, DSC analyses and tensile tests were applied to the samples to understand the effects of process parameters such as voltage, feed rate, tip-to-collector distance on thermal and mechanical properties.

4.1.3.1 Scanning Electron Microscopy (SEM) Analysis

SEM micrographs are shown in Figure 16 for nanofibers produced using voltage values of 25, 30, 35 and 40 kV. In voltage optimization, the limits of the electrospinning device were considered and optimization started with a value of 15 kV. At this voltage, the polymer jet did not form. The reason is that electrostatic force cannot overcome the solution surface tension and polymer jet cannot form when voltage is below a critical value. At 20 kV voltage value, polymer jet was formed and fiber production was observed, but continuous production was not achieved. This

indicated that the voltage value was sufficient to overcome the surface tension of the solution, but was not sufficient for continuous production. Continuous production was possible at other applied voltage values. Figure 16 (a) shows the morphology of the nanofibers produced with 25 kV. At this voltage value, fiber diameters were found to be around 200 nm.

Figure 16 (b), (c), (d) shows the SEM micrographs of nanofibers produced using electric potentials of 30, 35 and 40 kV, respectively. Significant reductions in fiber diameters produced using 40 kV compared to 25 kV were observed. The formation of finer fibers can be explained by increasing the tension of the polymer jet during production. Increasing the applied voltage is shown as an increase in the electric field strength and therefore the increase in the stretching on the polymer jet. Increasing stretching results in fine fiber formation [63, 64]. In addition, the increased electrical potential allows the polymer jet to reach the collector faster.

According to the observations made during the production, constant and continuous Taylor Cone formation was observed at 30 kV voltage, but an unstable Taylor Cone was formed due to the excessive stretching of the polymer jet at 35 and 40 kV.

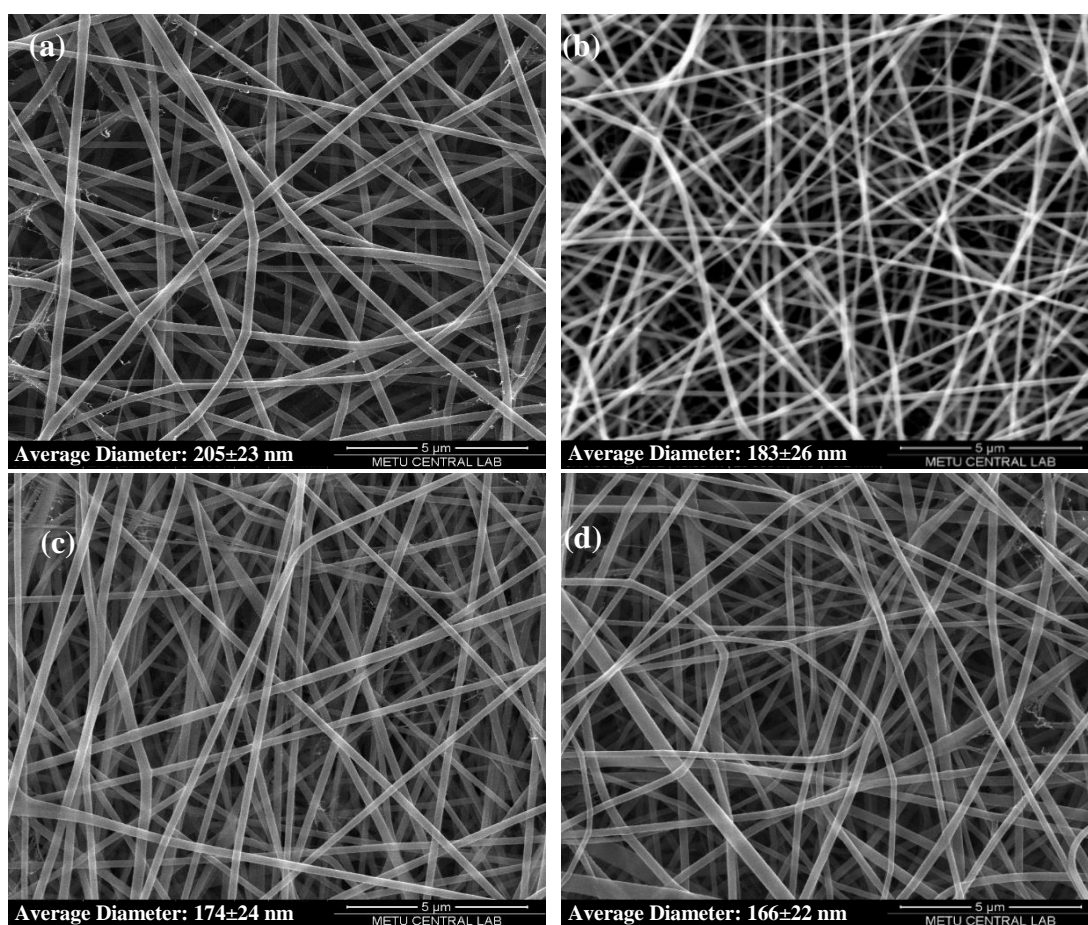


Figure 16. SEM micrograph of neat PA6 nanofibers produced using (a) 25, (b) 30, (c) 35, (d) 40 kV applied voltages.

Figure 17 shows cumulative frequency of fiber diameters of nanofibers produced with different applied voltages. Average fiber diameters decreased and distributions became narrow with increasing applied voltage. Increasing voltage may provide more uniform fiber formation.

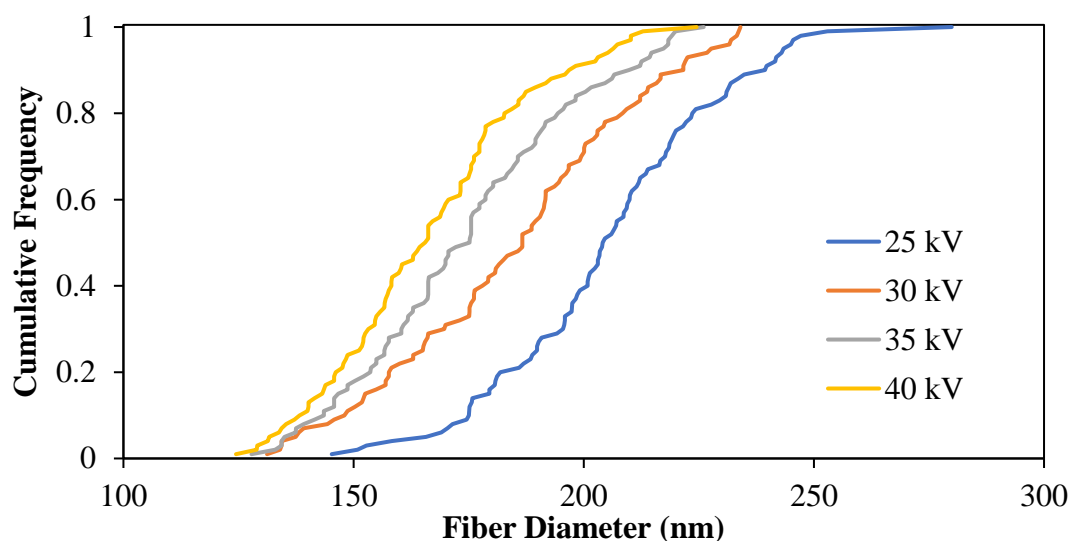


Figure 17. Cumulative frequency of fiber diameters of the nanofibers produced with different applied voltages.

4.1.3.2 Thermogravimetric Analysis (TGA)

Thermogravimetric analysis (TGA) was performed to investigate the thermal stability of the nanofiber produced using different electrical potential values and the weight loss graphs are given in Figure 18. By thermogravimetric analysis, the weight change and deformation temperatures of the samples depending on the temperature were obtained. Degradation temperatures are defined as the temperature between the temperature at which mass loss begins in the TGA analysis of the material and the temperature value at which the mass is fixed. This temperature was calculated by taking the derivative of the TGA curve. When the graphs were examined, no significant change was observed in the dissociation temperatures at different electrical potential values.

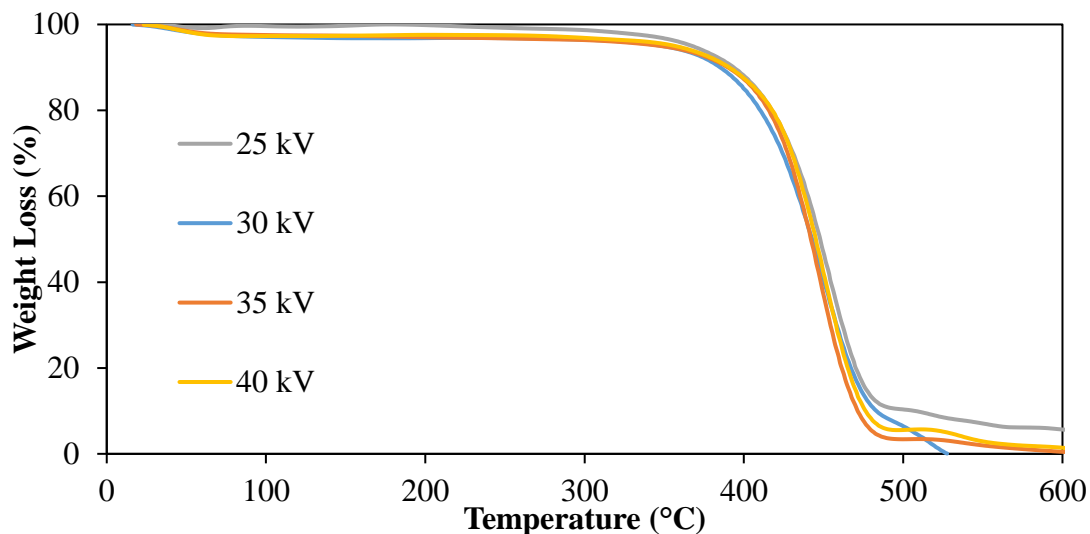


Figure 18. TGA curves of the nanofibers produced using different applied voltage values.

4.1.3.3 Differential Scanning Calorimetry (DSC) Analysis

DSC analysis was performed for the nanofibers produced using different electrical potential values. Some thermal properties of the fibers such as glass transition temperature (T_g), melting temperature (T_m) and degree of crystallization values are given in Table 6 below. The DSC curves of the samples are represented in Appendix B.

Results indicated that the changing voltage values did not cause a significant change in the T_g and T_m of the nanofibers. It is known that the electrospinning process parameters influence the degree of crystallization of the nanofibers. For this reason, the crystallization percentages of the prepared samples were calculated. As it is seen from the results, the highest crystallinity percentage was obtained in the fibers produced using 30 kV electrical potential. During the electrospinning process, as the polymer jet moves from the needle to the collector, the molecular orientation along with the electric field occurs, which results in the crystallization of the polymer. It is stated that the orientation of the polymer chains increases due to the increased elongation of the polymer jet with increasing electrical stretching. However, this increase continues only to a certain electrical potential value, which is called the

optimum voltage value. It is expected that beyond the critical value degree of crystallization will decrease. This is due to the fact that at high electrical potential values the polymer jet reaches the collector in a shorter time than is necessary for crystallization of the polymer [64]. In our study, there was a decrease in percent crystallization at value after 30 kV which was taken as an optimum value for this process.

Table 6. DSC data of the nanofibers produced using different applied voltage values.

Voltage (kV)	T _g (°C)	T _m (°C)	ΔH _f ^m (J/g)	X _c (%)
25	48.14	220.69	85.36	44.71
30	49.59	222.75	88.66	46.44
35	51.96	222.72	82.13	43.02
40	49.24	223.34	77.10	40.39

4.1.3.4 Tensile Test Results

The tensile test results of PA6 nanofiber mat produced at different applied voltage values are given in Figures 19-21 and detailed tensile test data is tabulated in Table C.1 of Appendix C. When the tensile strength, tensile modulus and elongation at break results of the mats produced with different voltages were compared, a slight increase in the tensile strength and tensile modulus values of the fiber mat produced using 35 kV compared to other voltages was observed. However, the highest elongation was obtained from fibers produced using 30 kV.

Along with decreasing fiber diameter, higher mechanical strength and lower ductility are obtained [65]. Considering this situation, it is expected that the nanofiber mat produced with 25 kV have the lowest mechanical strength end result and those produced with 40 kV have the highest mechanical result. However, the mat thickness produced using the 25 kV applied voltage was thinner than the samples produced at equal time in other electrical potential values. The result showed that less fiber was produced at low electric field values. In addition, at the 40 kV applied voltage value,

high stretching of the polymer jet affected fiber morphology, resulting in a high standard deviation in mechanical results. These situations explained that the expected effect of applied voltage on mechanical test results cannot be obtained. Considering values at 30 and 35 kV, it is seen that the tensile modulus are close to each other for these two values.

Considering all the characterization experiments and observations made, 30 kV was chosen as the most suitable electrical potential value because of the suitability for continuous production and the relatively higher crystallization percentage and the lower the standard deviations as a result of the mechanical tests.

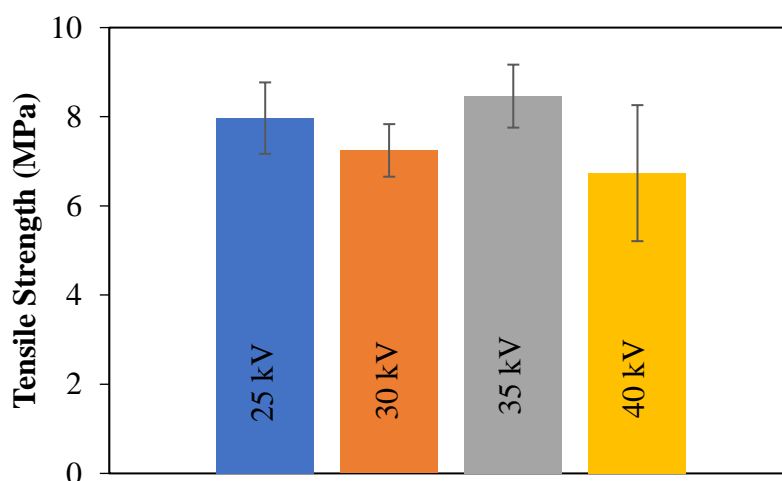


Figure 19. Tensile strengths of the nanofiber mats produced using different applied voltage values.

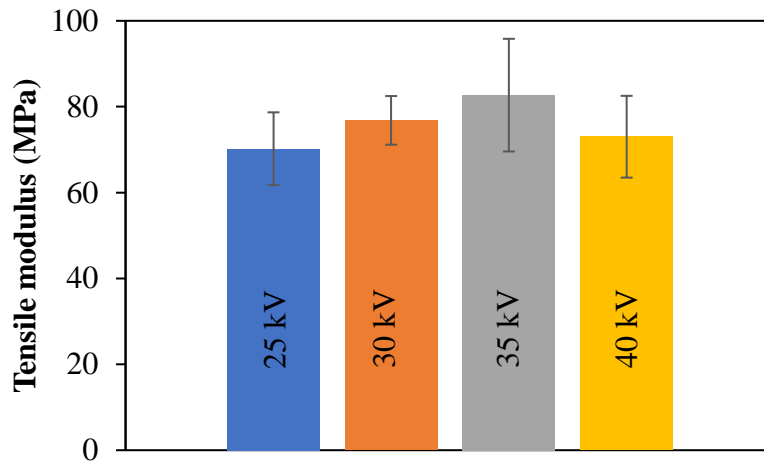


Figure 20. Tensile moduli of the nanofiber mats produced using different applied voltage values.

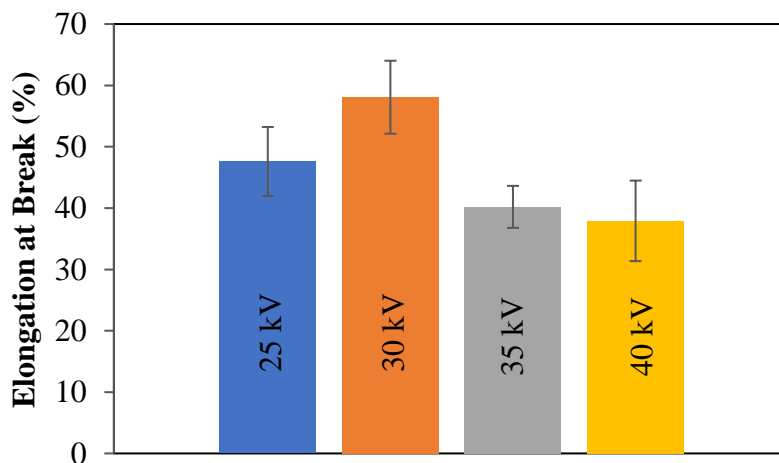


Figure 21. Elongation at break of the nanofiber mats produced using different applied voltage values.

4.1.4 Feed Rate Optimization

The solution feed rate values were optimized by setting the electrical potential and tip-to-collector distance values to 30 kV and 10 cm, respectively. The feed rate was increased from 0.1 to 0.40 mL/h. The produced nanofibers are characterized by SEM, TGA, DSC analyses and tensile tests.

4.1.4.1 Scanning Electron Microscopy (SEM) Analysis

SEM micrographs are shown in Figure 22 for the nanofibers produced using feed rate values of 0.1, 0.2, 0.25, 0.30, 0.33, 0.35 and 0.40 mL/h, respectively.

In order to produce nanofibers by electrospinning, the amount of solution ejected to the tip of the needle must be sufficient for Taylor Cone formation. Nanofibers were produced at feeding rates of 0.10, 0.20 and 0.25 mL/h, but the semi-spherical shape of the Taylor cone was not preserved during production due to the lack of polymer solution feed.

An overall increase in average fiber diameter was observed with increasing feed rate which is associated with an increase in volume (Figure 22 (e)-(g)). Similar result was also obtained in the literature [66, 67]. At 0.35 and 0.40 mL/h feed rates, tip blocking was observed due to excess solution accumulation at the tip. Accumulation of solution cause a problem during the drying of polymer jet [1]. At feed rates of 0.30 and 0.33 mL/hr, the Taylor cone was properly formed and that continuous production was achieved without blocking the needle tip.

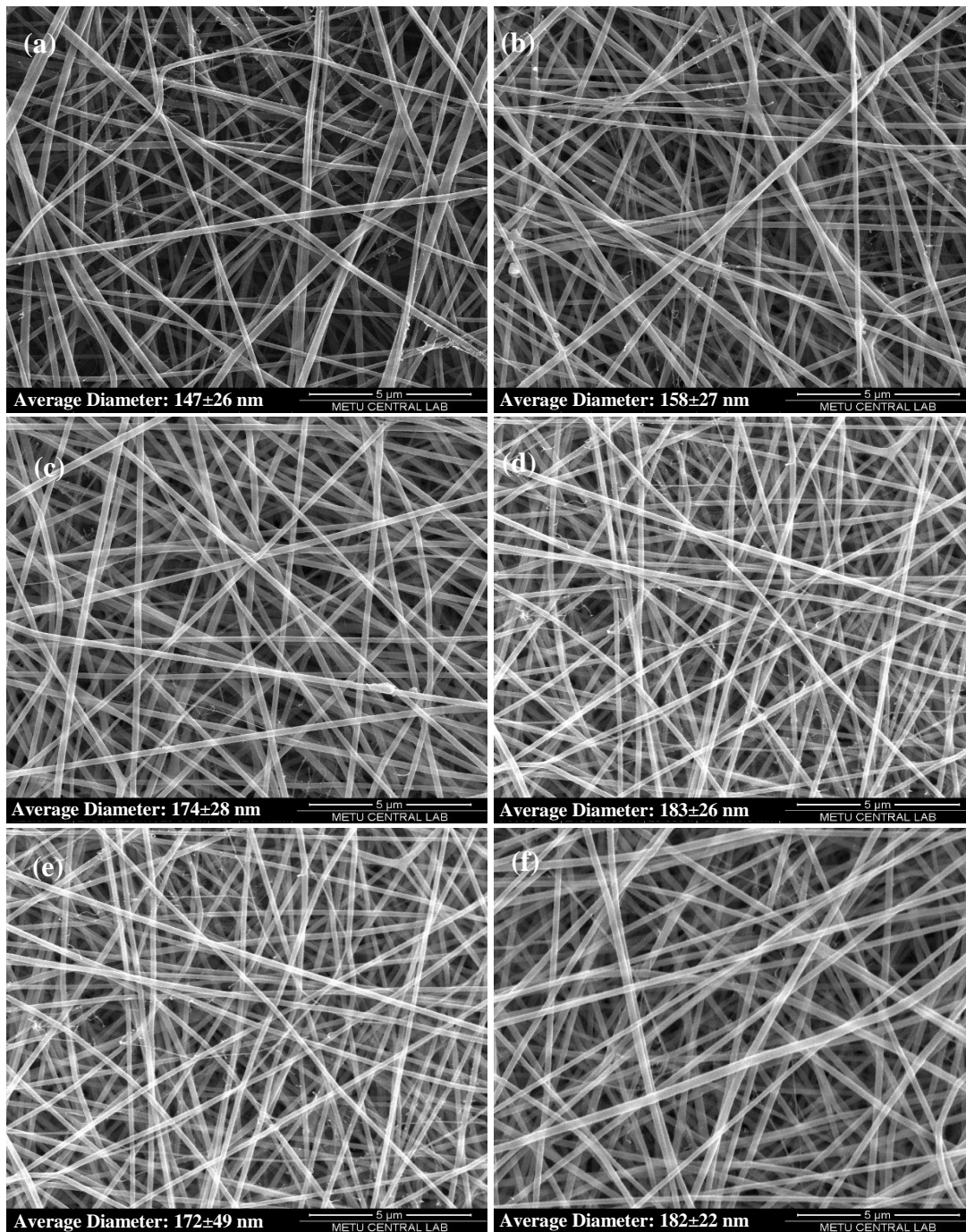


Figure 22. SEM micrograph of neat PA6 nanofibers produced using (a) 0.10, (b) 0.20, (c) 0.25, (d) 0.30, (e) 0.33, (f) 0.35 (g) 0.40 mL/h feed rates.

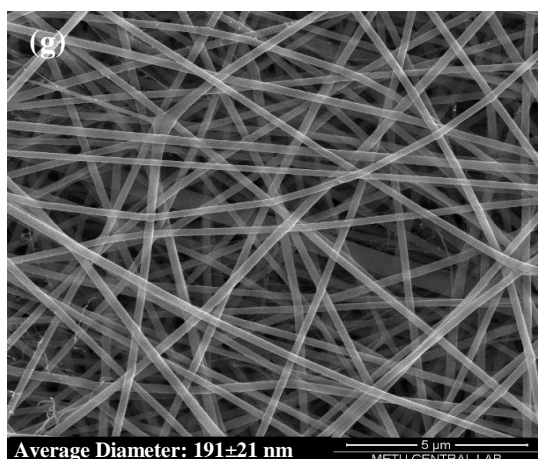


Figure 22 (cont'd). SEM micrograph of neat PA6 nanofibers produced using (a) 0.10, (b) 0.20, (c) 0.25, (d) 0.30, (e) 0.33, (f) 0.35 (g) 0.40 mL/h feed rates.

Figure 23 shows cumulative frequency of fiber diameters of nanofibers produced with different feed rates. The results showed that both small and large fibers were obtained at 0.33 mL/h feed rate, which resulting in a wide distribution. Other feed rate values showed narrow fiber distributions.

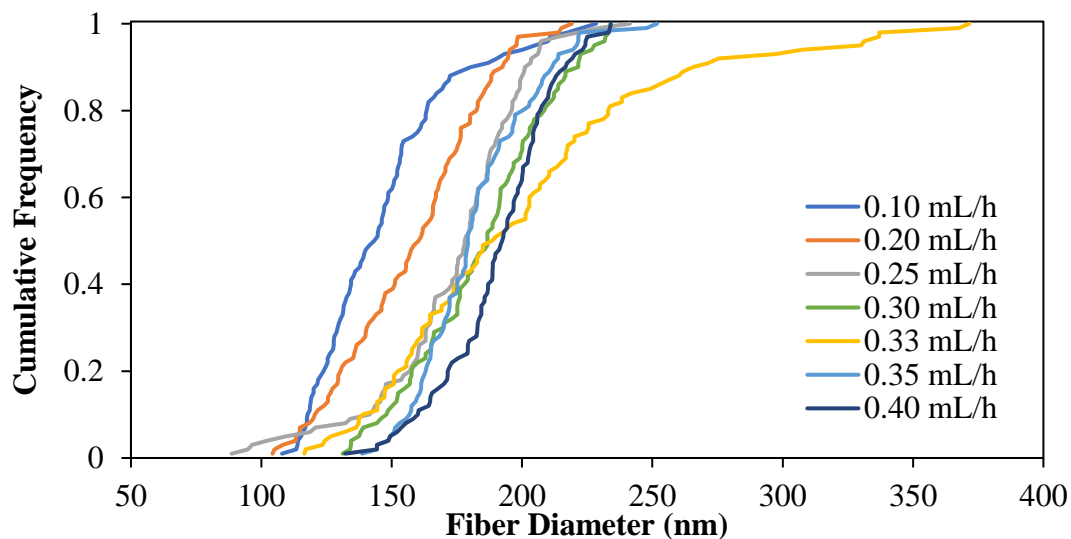


Figure 23. Cumulative frequency of fiber diameters of the nanofibers produced with different feed rates.

4.1.4.2 Thermogravimetric Analysis (TGA)

TGA graphs of the nanofibers produced using different solution feed rates were given in Figure 24. When the graphs were analyzed, no significant change in the decomposition temperatures was observed in the different solution feed rate values.

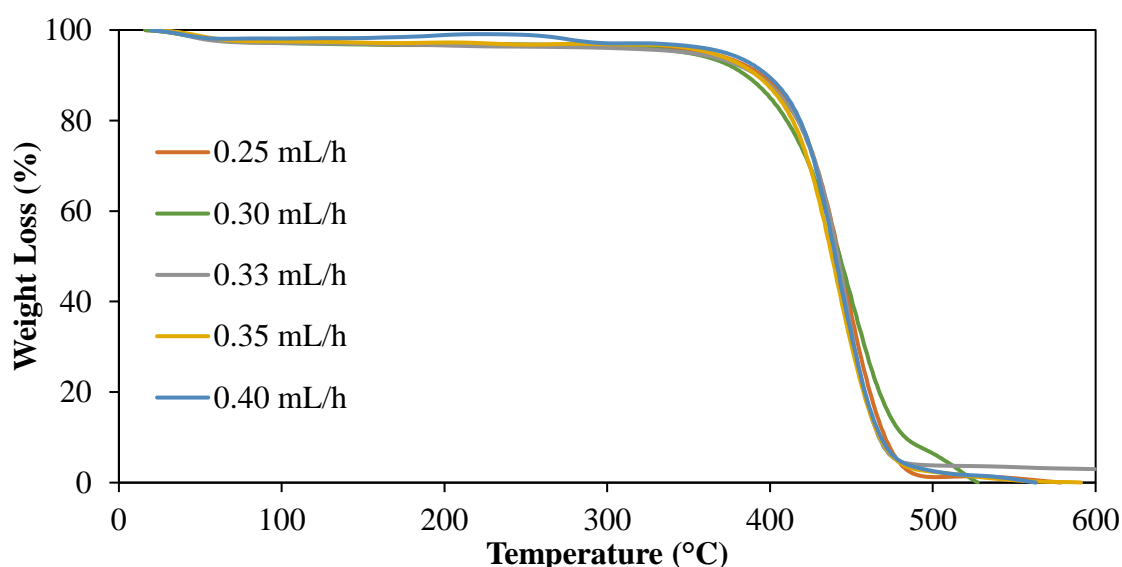


Figure 24. TGA curves of the nanofibers produced using different feed rate values.

4.1.4.3 Differential Scanning Calorimetry (DSC) Analysis

DSC analysis was performed for the produced nanofibers using different solution feed values and T_g , T_m and degree of crystallization of the fibers are given in Table 7. The DSC curves of the samples are given in Appendix B. The DSC analysis was not carried out for the samples produced at the solution feed rate values of 0.1 and 0.2 mL/h because of inadequate material production.

When the results were assessed, it was found that varying solution feed rates do not cause a significant change in T_g and T_m . When the degree of crystallization was calculated, it was found that this value increased slightly with the increasing solution feed, then decreased thereafter. Increased solution feed rate increased ejected polymer solution to the needle, which resulted in the applied voltage to become insufficient to form the continuous polymer jet. As a result, the high solution feed rate can cause a decrease in the degree of crystallization. At low solution feed rates, the solvent cannot

evaporate completely during production due to overstretching of the polymer jet which also cause a decrease in degree of crystallization. Moreover, low feed rates are not sufficient for continuous production of nanofibers [67]. According to the results in Table 7, the degree of crystallization started to decrease after the solution feed rate value of 0.30 mL/h.

Table 7. DSC data of the nanofibers produced using different feed rate values.

Feed Rate (mL/h)	T _g (°C)	T _m (°C)	ΔH _f ^m (J/g)	X _c (%)
0.25	47.42	224.00	84.28	44.15
0.30	49.59	222.75	88.66	46.44
0.33	46.12	225.16	84.85	44.44
0.35	47.55	223.50	80.75	42.30
0.40	49.17	226.03	74.17	38.85

4.1.4.4 Tensile Test Results

The tensile test results of PA6 nanofiber mats at different feed rate values are given in Figures 25-27 and detailed tensile test data is tabulated in Table C.2 of Appendix C. It was found that the standard deviation was generally large in the samples produced with feed rates of 0.25 and 0.40 mL/h. This shows that low and high feed rate values was not suitable for smooth and continuous sample production. Although the tensile strength value at the feed rate of 0.4 mL/h was higher than the other feed rate values, it can be said that feed rate of 0.33 mL/h resulted in better tensile strength due to the lower standard deviation. When the tensile modulus results were compared, the highest value was obtained at the feed rate of 0.33 mL/h. Providing smooth and continuous fiber production at this feed value increased the orientation of the polymer chains and consequently improved the mechanical properties. When the results of the elongation at break obtained for different feed rate values were compared, it was seen that the elongation at break increased up to 0.33 mL/h feed rate value and then decreased slightly. Glass transition temperatures did not change significantly, which indicated that the mobility of the nanofibers was not affected by different feed rates.

Considering the diameters, degree of crystallization, mechanical properties of the nanofibers, and observations during production, it was decided to select the feed rate of 0.33 mL/h as the optimum value.

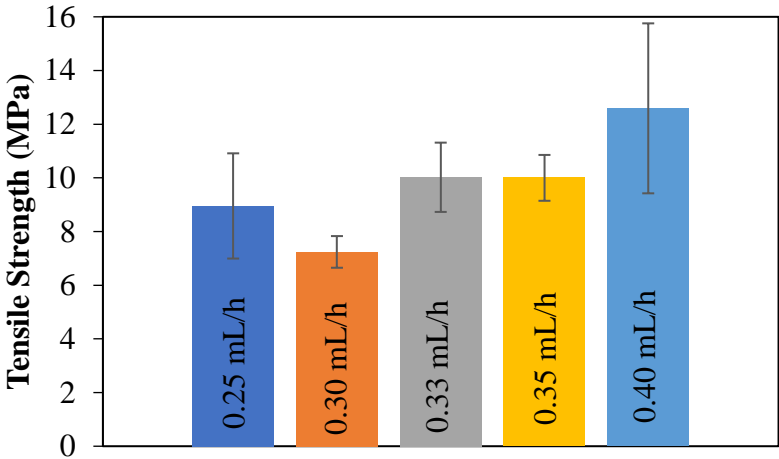


Figure 25. Tensile strengths of the nanofiber mats produced using different feed rate values.

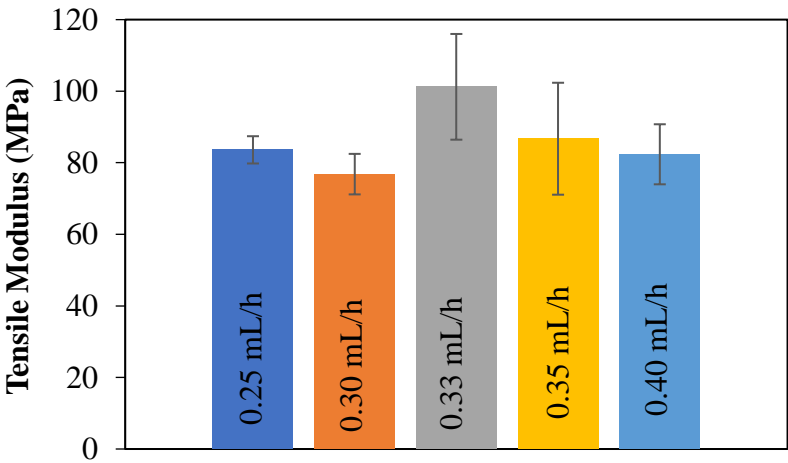


Figure 26. Tensile moduli of the nanofiber mats produced using different feed rate values.

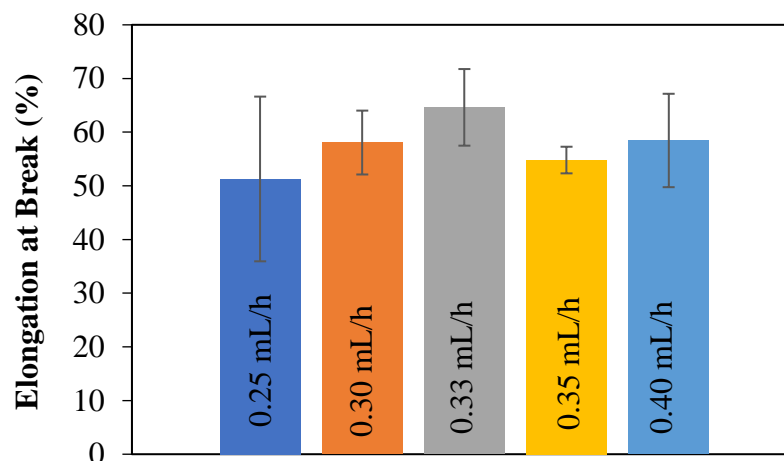


Figure 27. Elongation at break of the nanofiber mats produced using different feed rate values.

4.1.5 Tip-to-Collector Distance Optimization

The tip-to-collector distance value was optimized after the electrical potential and solution feed rate values were set to 30 kV and 0.33 mL/h, respectively. Distance was increased from 5 to 15 cm for optimization of this parameter. SEM, TGA, DSC analyses and tensile tests were used to characterize the produced nanofibers.

4.1.5.1 Scanning Electron Microscopy (SEM) Analysis

SEM micrographs are given in Figure 28 for nanofibers produced using the collection distance values of 5, 7, 9, 10, 12, and 15 cm. When the SEM images and average fiber diameters were compared, a decrease in fiber diameter was found. Increase in the time of the polymer jet to reach the collector provides a longer time for the solvent to evaporate. This is resulting in the formation of thinner fiber. However, with increasing distance, the electric field strength decreases and the polymer jet is less stretched which causes thicker fiber formation. Due to these two results, fiber diameter decreased up to a certain distance value and then increased.

The production of nanofibers at a distance of 5 cm was tried but continuous production was not possible due to the insufficient tip-to-collector distance. This was because the electric field is inversely proportional to the distance which is explained by the

equation of $E = V/d$, where E is electric field, V is voltage and d is distance. At very short distances, the polymer jet was too stretched that caused unstable jet and non-continuous fiber production [68, 69].

Nanofiber production at 7, 9, 10, 12 and 15 cm distance values was possible, but at the values of 7 and 15 cm, the shape of Taylor Cone was not preserved during production. This is due to the instability of the polymer jet at a collection distance of 7 cm. At 15 cm distance value, the electric field strength decreased and the continuity of polymer jet could not be maintained. At 9, 10 and 12 cm distance values, Taylor Cone was properly formed and the continuous production was made without needle tip blocking. However, when the average diameter values were considered, thin and uniform fibers with less standard deviation were produced at 9 cm collecting distance.

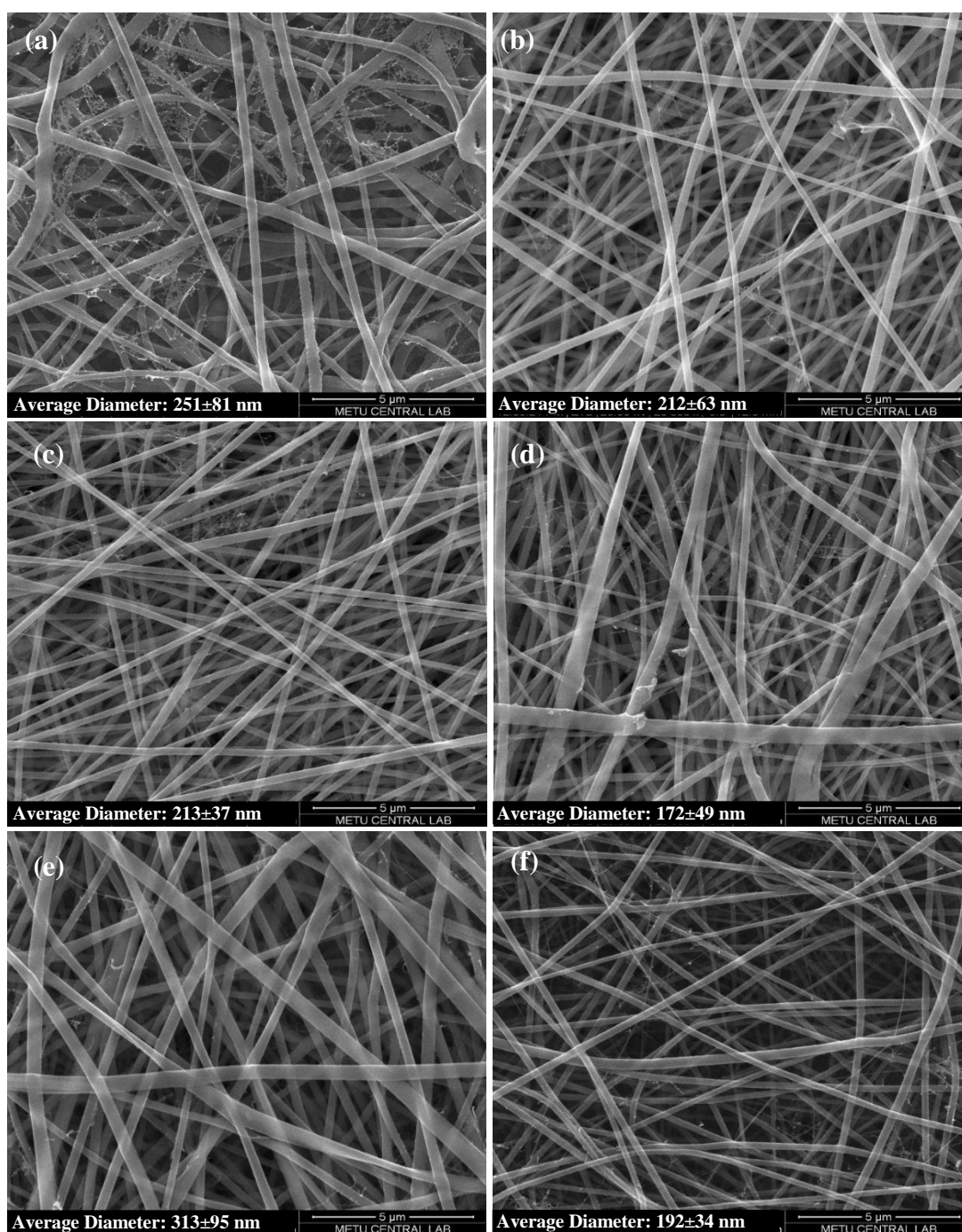


Figure 28. SEM micrograph of neat PA6 nanofibers produced using (a) 5, (b) 7, (c) 9, (d) 10, (e) 12, (f) 15 cm tip-to-collector distances.

Figure 29 shows cumulative frequency of fiber diameters of nanofibers produced with different tip-to-collector distances. The results show that there was no linear relationship between the tip-to-collection distance and the fiber diameter distribution.

Only at low and high tip-to-collector distances, the homogeneity of the fibers seemed to be reduced and a wider fiber distribution was obtained.

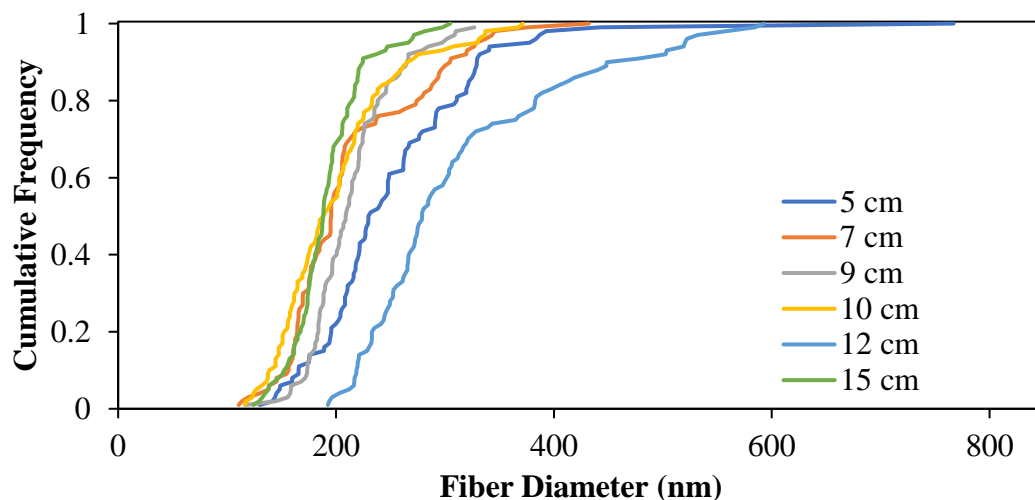


Figure 29. Cumulative frequency of fiber diameters of the nanofibers produced with different tip-to-collector distances.

4.1.5.2 Thermogravimetric Analysis (TGA)

Thermal decomposition of the produced nanofibers with different distance values were studied by TGA analysis. The weight percentage versus temperature graphs are shown in Figure 30. When the results were analyzed, it was seen that there was no significant change in the decomposition temperatures of the fibers produced at different distance values.

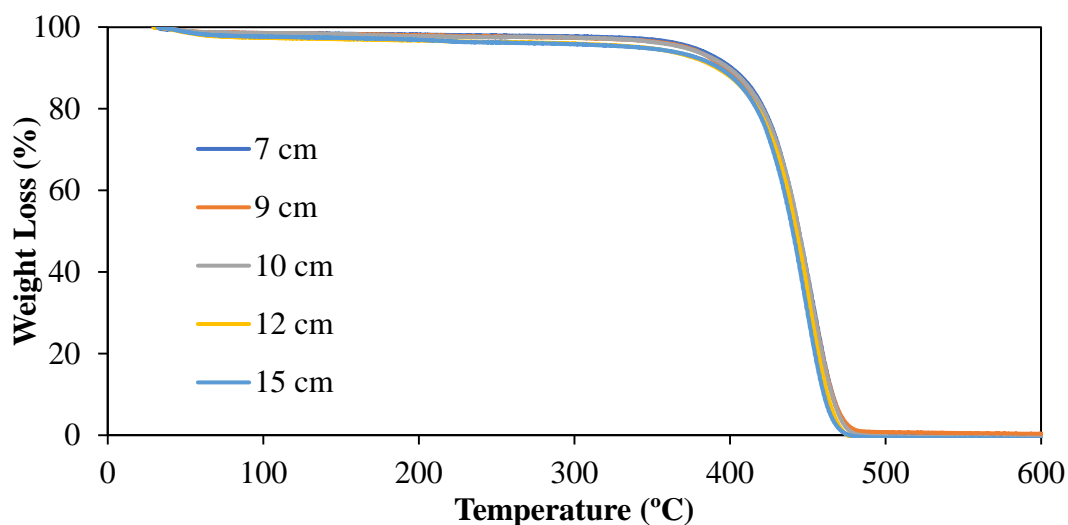


Figure 30. TGA curves of the nanofibers produced using different tip-to-collector distance values.

4.1.5.3 Differential Scanning Calorimetry (DSC) Analysis

Thermal analysis of produced nanofibers with different distance values (7, 9, 10, 12 and 15 cm) also achieved by DSC analysis. Some thermal properties such as glass transition temperature (T_g), melting temperature (T_m) and percent crystallization of the fibers are given in Table 8. The DSC curves of the samples are given in Appendix B. The DSC analysis was not carried out for the sample produced at 5 cm because sufficient sample cannot be produced.

DSC results implied that glass transition temperatures, melting temperatures did not significantly change with changing distance values. The highest degree of crystallization result was obtained at 15 cm tip-to-collector distance. Theoretically, with increasing distance, the time required for the polymer jet to reach the collector is increased and this is thought to increase molecular orientation. With increasing molecular orientation, the degree of crystallization is expected to increase [64].

Table 8. DSC data of the nanofibers produced using different feed rate values.

Distance (cm)	T _g (°C)	T _m (°C)	ΔH _f ^m (J/g)	X _c (%)
7	45.54	223.62	85.72	44.90
9	45.71	224.32	77.79	40.74
10	46.12	225.16	84.85	44.44
12	45.62	224.44	86.21	45.15
15	43.66	224.69	88.68	46.45

4.1.5.4 Tensile Test Results

The tensile test results of PA6 nanofiber mats produced at different tip-to-collector distance values are given in Figures 31-33 and detailed tensile test data is tabulated in Table C.3 of Appendix C. When all results were examined, it was seen that the standard deviation was larger in the sample produced with a collection distance of 15 cm. This showed that high collection distance values are not suitable for smooth and continuous sample production. Among all the mechanical properties, lower tensile strength, elongation at break and tensile modulus values were obtained at 7 cm and 15 cm tip-to-collector distance values as expected. When 9, 10 and 12 cm distance values were compared, the highest tensile strength and elongation at break results were obtained at 10 and 9 cm, respectively. Ensuring smooth and continuous fiber production at 9 and 10 cm collection distance increased the orientation of the polymer chains and consequently higher mechanical properties were obtained. Observations made during the production were considered when comparing the values of collection distance of 9 and 10 cm. At a distances of 9 and 10 cm, the productions could be continued for a longer period of time and the shape of the Taylor Cone could be maintained. Taking all this into consideration, it was decided that the collection distance of 9 and 10 cm should be chosen as the optimum values.

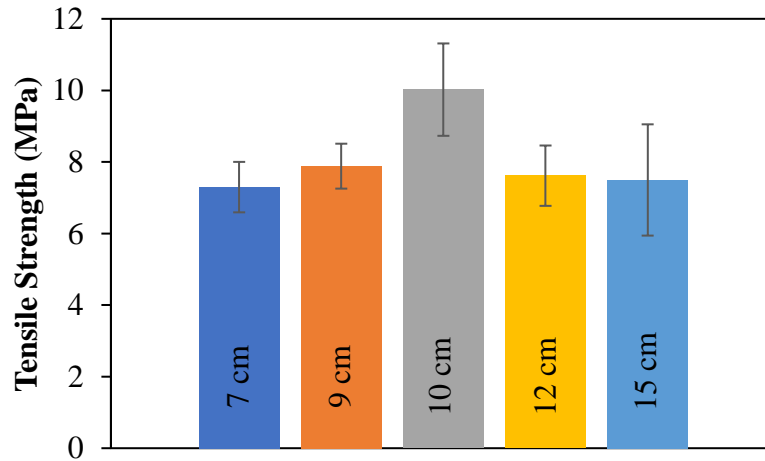


Figure 31. Tensile strengths of the nanofiber mats produced using different tip-to-collector distance values.

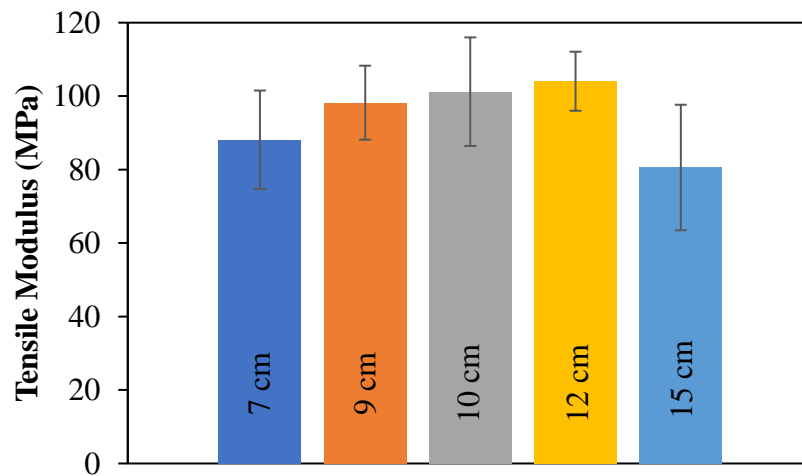


Figure 32. Tensile moduli of the nanofiber mats produced using different tip-to-collector distance values.

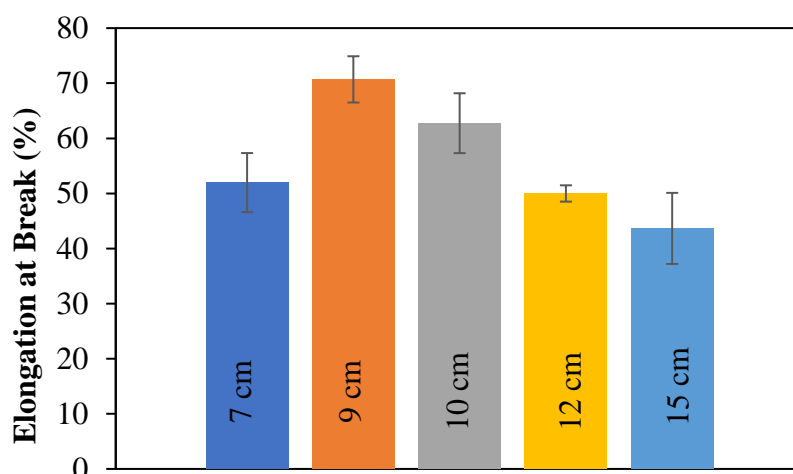


Figure 33. Elongation at break of the nanofiber mats produced using different tip-to-collector distance values.

4.2 Preparation and Characterization of Electrospun Fibers of PA6/HNTs Nanocomposites

Determination of the HNTs concentration studies were carried out simultaneously with the electrospinning parameter optimization. HNTs were mixed with PA6 and composite production was performed. In order to find the appropriate HNTs concentration and investigate the effects of surface modification of nanotubes, 1, 2, 4, 6 and 8 wt.% unmodified and modified HNTs were added to the PA6 matrix. 30 kV voltage, 0.3 mL/h feed rate and 10 cm tip-to-collector distance values were used to produce composite nanofiber. The samples were characterized by SEM, TEM, DSC, TGA analyses and tensile test and the results are discussed below.

4.2.1 Scanning Electron Microscopy (SEM) Analysis

SEM micrographs are given in Figures 34-38 for nanocomposites produced using unmodified HNTs (un-HNTs). Looking at the SEM micrographs, the white points at 1000x magnifications show HNTs agglomerations. The number of agglomerations increased with increasing HNTs concentration. In Figure 34, HNTs adhered to single nanofibers at 1 wt.% un-HNTs which was the lowest concentration. Contrary to this, the HNTs agglomerations with a diameter of 2-3 μm can be seen clearly at 6 wt.% un-

HNT concentration. These agglomerations showed unmodified HNTs prefer each other instead of PA6 matrix.

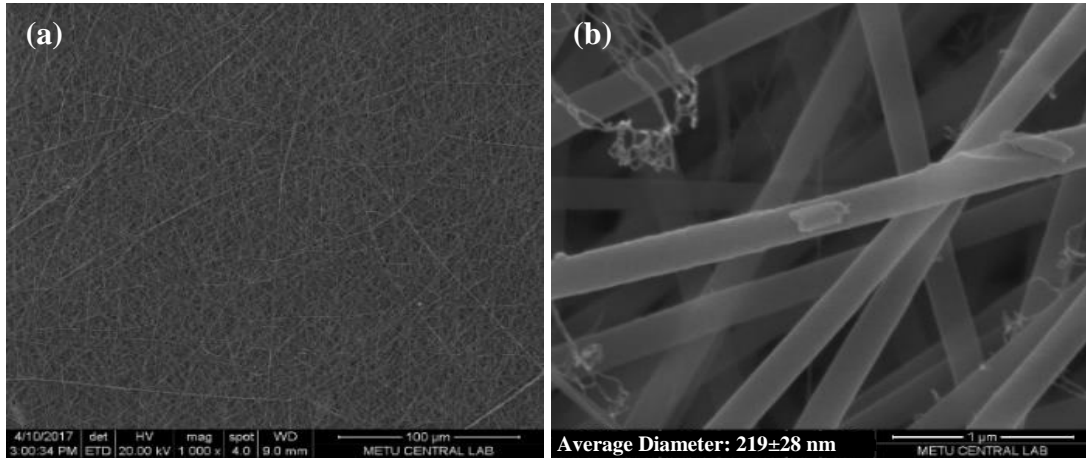


Figure 34. SEM micrograph of the composite containing 1 wt.% un-HNTs (a) SEM micrograph at 1000x magnification (b) at 100000x magnification.

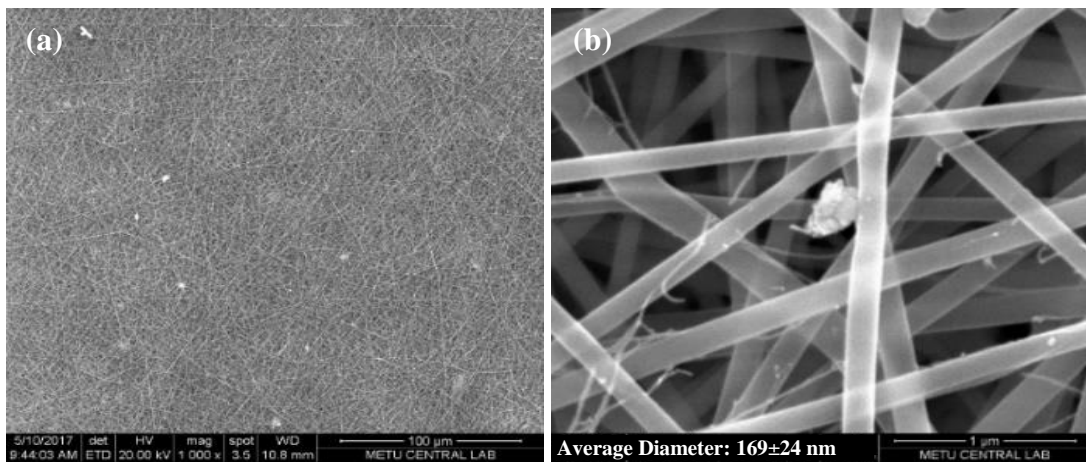


Figure 35. SEM micrograph of the composite containing 2 wt.% un-HNTs (a) SEM micrograph at 1000x magnification (b) at 100000x magnification.

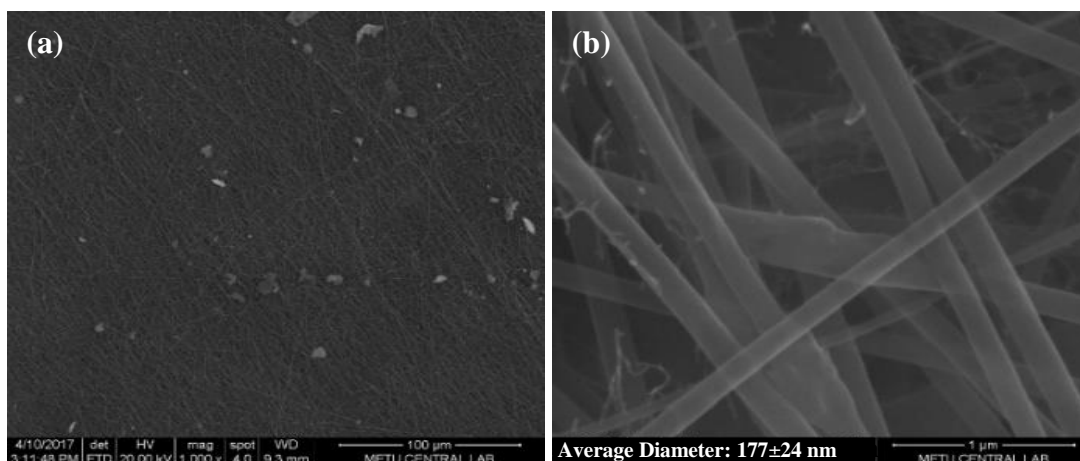


Figure 36. SEM micrograph of the composite containing 4 wt.% un-HNTs (a) SEM micrograph at 1000x magnification (b) at 100000x magnification.

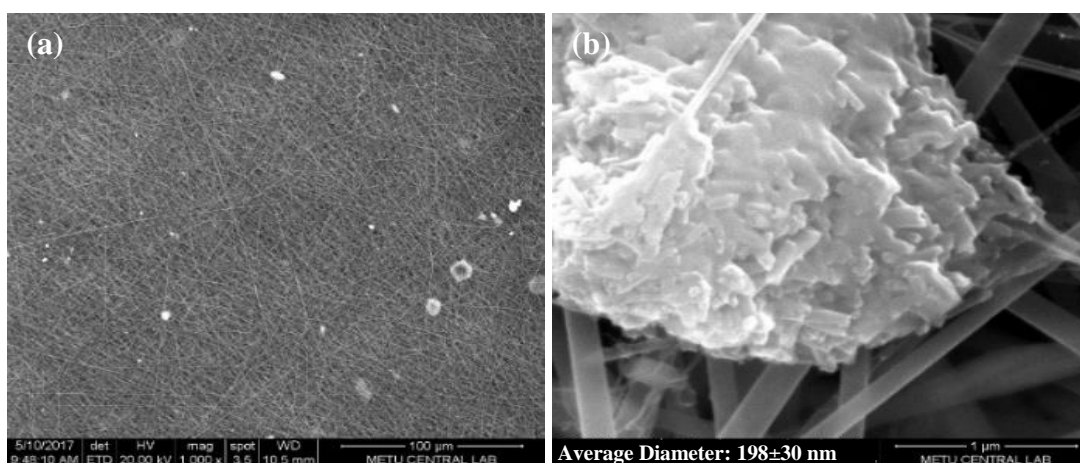


Figure 37. SEM micrograph of the composite containing 6 wt.% un-HNTs (a) SEM micrograph at 1000x magnification (b) at 100000x magnification.

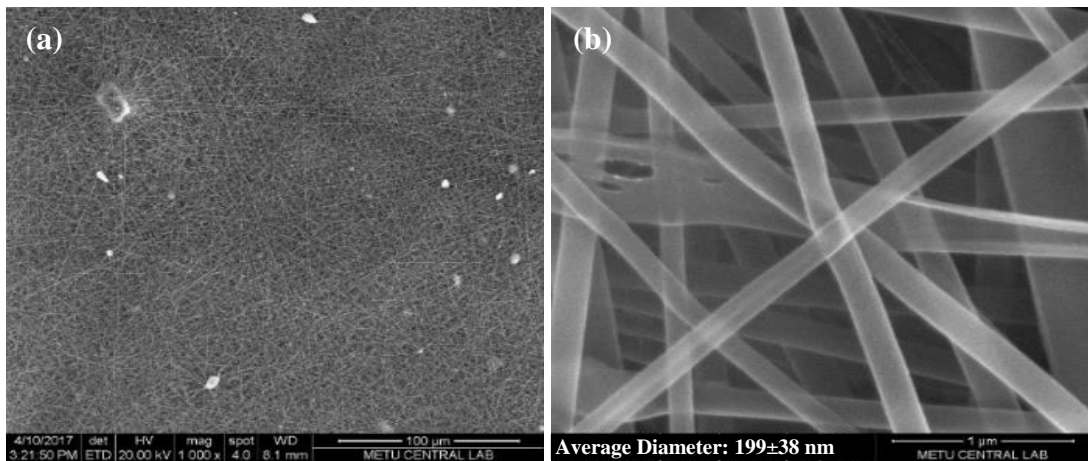


Figure 38. SEM micrograph of the composite containing 8 wt.% un-HNTs (a) SEM micrograph at 1000x magnification (b) at 100000x magnification.

Figure 39 shows cumulative frequency of fiber diameters of nanofiber nanocomposites containing different un-HNT concentration. It is seen that the larger diameters were obtained and the fiber distribution became wider in the samples containing 1 and 8 wt.% un-HNTs.

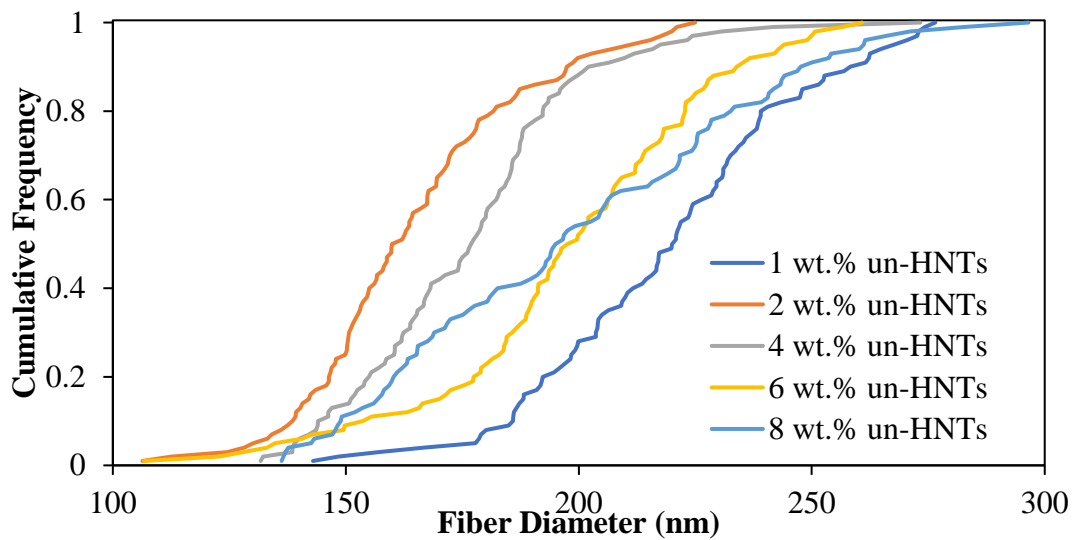


Figure 39. Cumulative frequency of fiber diameters of the nanofiber nanocomposites containing different un-HNT concentration.

In order to produce modified HNTs (m-HNTs), 1 wt.% APTES was used to prevent formation of agglomeration. SEM micrographs and diameter distribution graphs are given in Figures 40-44 for nanocomposites produced using modified HNTs. The number and size of the HNTs agglomerations were reduced compared to the composites produced with the unmodified HNTs. Although surface modification reduces the formation of agglomerations, at high concentrations HNTs prefers each other and agglomerations become visible that can be seen in Figures 43 and 44 at 1000x magnifications. As can be seen in Figure 40 (b), smooth and non-beaded fibers were obtained with the lowest amount of reinforcement. Figure 41 (b) shows the structure of the 2 wt.% m-HNTs adhering to certain regions of the fibers. Structure of 4 wt.% m-HNT containing composite is shown in Figure 42 (b). Single HNTs was found inside a fiber and determined by EDS analysis. Similar formations were seen in the samples containing 6 and 8 m-HNTs. At these concentrations, however, the number of agglomerations increased. In addition, the fiber diameter increased in the regions where the nanotubes get into the fiber that is seen in Figures 42 and 43 (b). It can be concluded that modified HNTs interacted more with polymer matrix than unmodified HNTs.

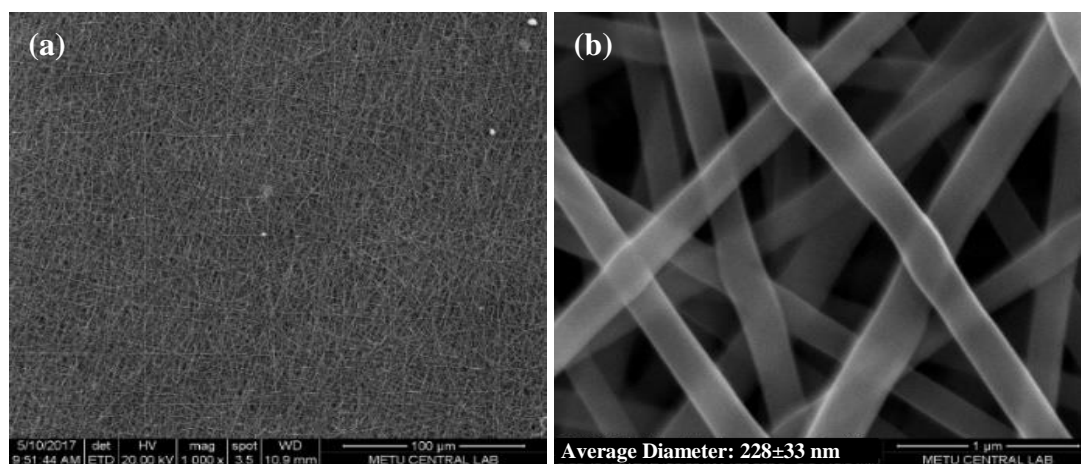


Figure 40. SEM micrograph of the composite containing 1 wt.% m-HNTs (a) SEM micrograph at 1000x magnification (b) at 100000x magnification.

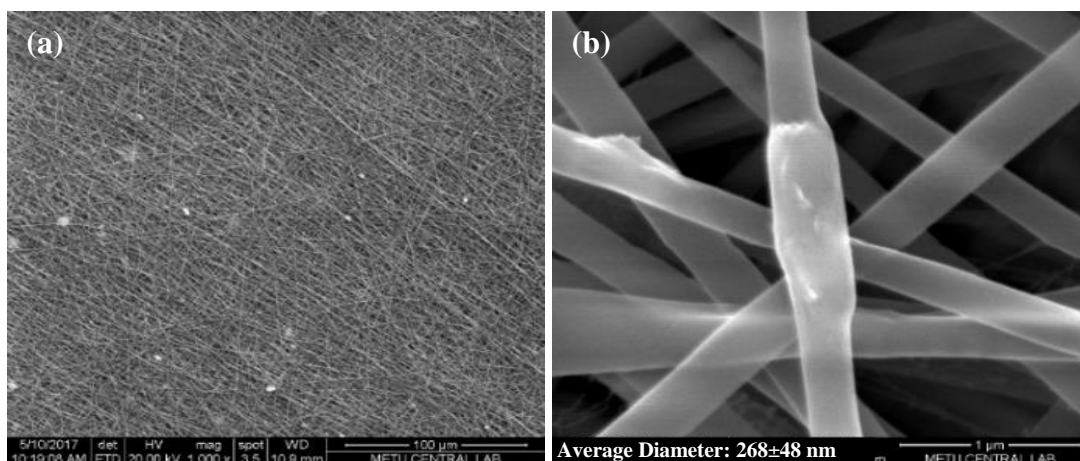


Figure 43. SEM micrograph of the composite containing 6 wt.% m-HNTs (a) SEM micrograph at 1000x magnification (b) at 100000x magnification.

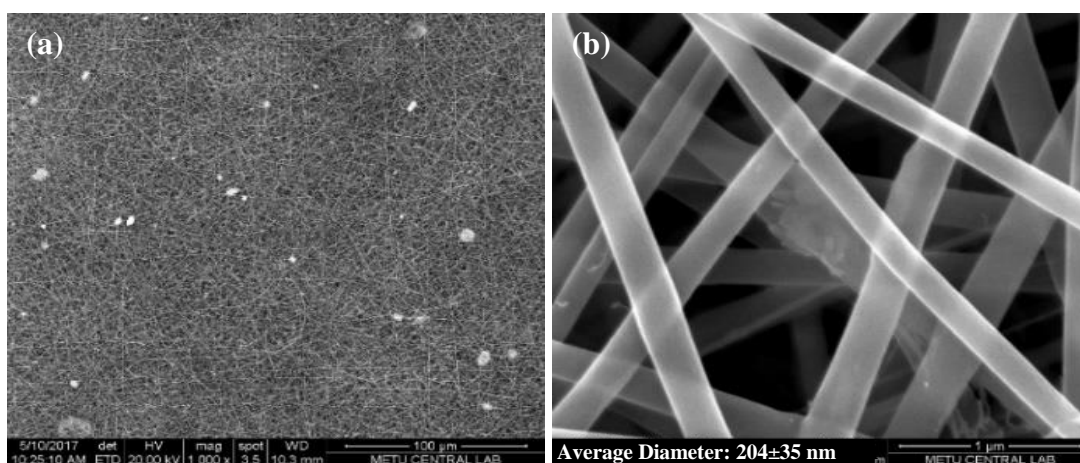


Figure 44. SEM micrograph of the composite containing 8 wt.% m-HNTs (a) SEM micrograph at 1000x magnification (b) at 100000x magnification.

Figure 45 shows cumulative frequency of fiber diameters of nanofiber nanocomposites containing different m-HNT concentration. Results showed that there was no linear relationship between HNTs amount and average fiber diameters or diameter distributions. 6 wt.% m-HNTs containing sample has the highest average diameter and the widest fiber distribution. The results of the other samples seemed to be similar to each other.

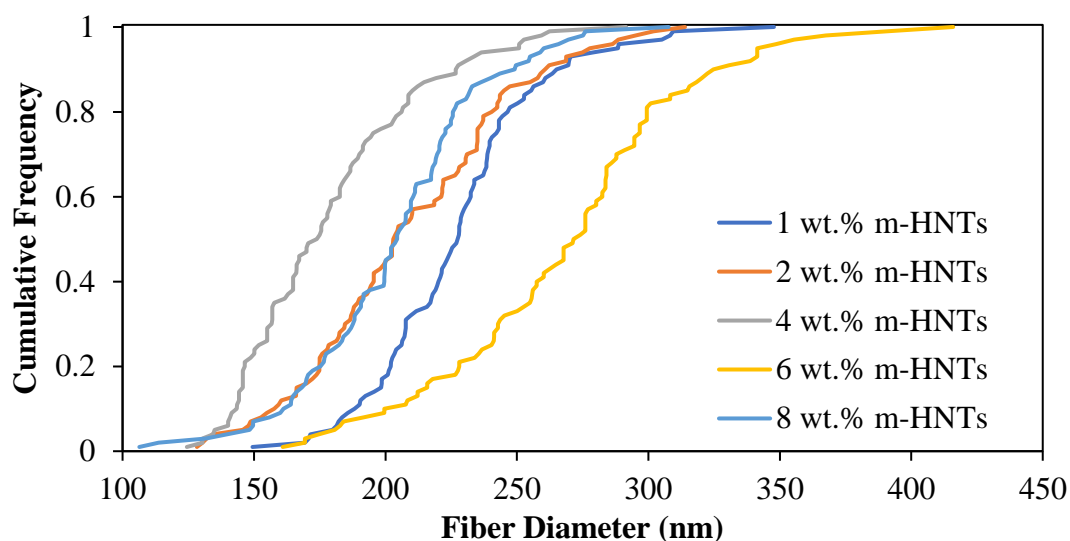


Figure 45. Cumulative frequency of fiber diameters of the nanofiber nanocomposites containing different un-HNT concentration.

4.2.2 Transmission Electron Microscopy (TEM) Analysis

Transmitted electron microscopy (TEM) micrographs are given in Figures 46 and 47 for nanocomposite fibers produced using 1 and 8 wt.% m-HNT, respectively. Selection of 1 and 8 wt.% m-HNTs concentrations was based on revealing the morphological differences between low and high filler concentrations. TEM micrographs showed HNTs embedded in the fiber. There was no significant change in the diameters of fibers containing 1 wt.% m-HNT. On the contrary, fibers containing 8 wt.% m-HNT showed a regional diameter increase due to agglomeration formed by HNTs. As a conclusion, the nanotubes were oriented in the fibers containing 1 wt.% m-HNT.

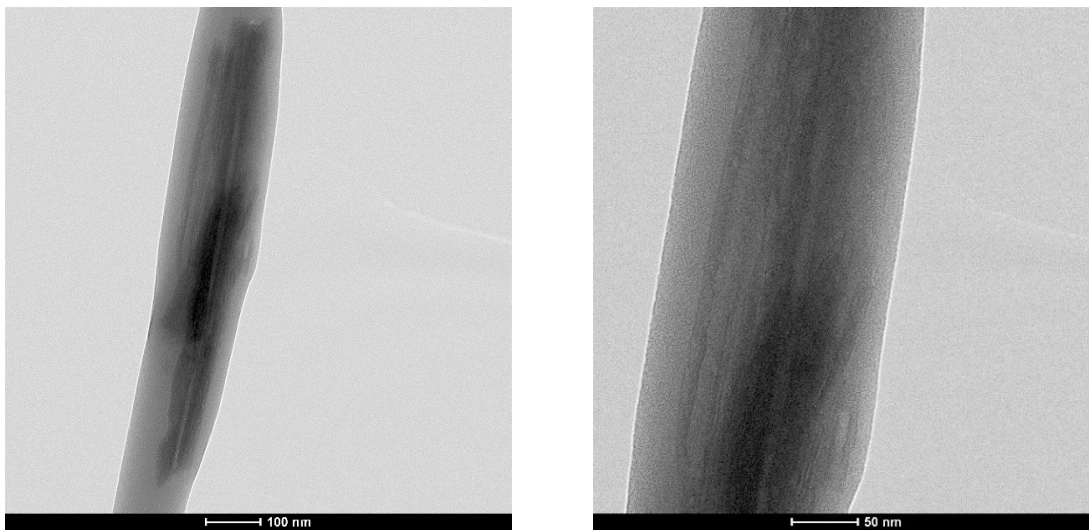


Figure 46. TEM micrographs of the composite nanofibers containing 1 wt.% m-HNTs at different magnifications.

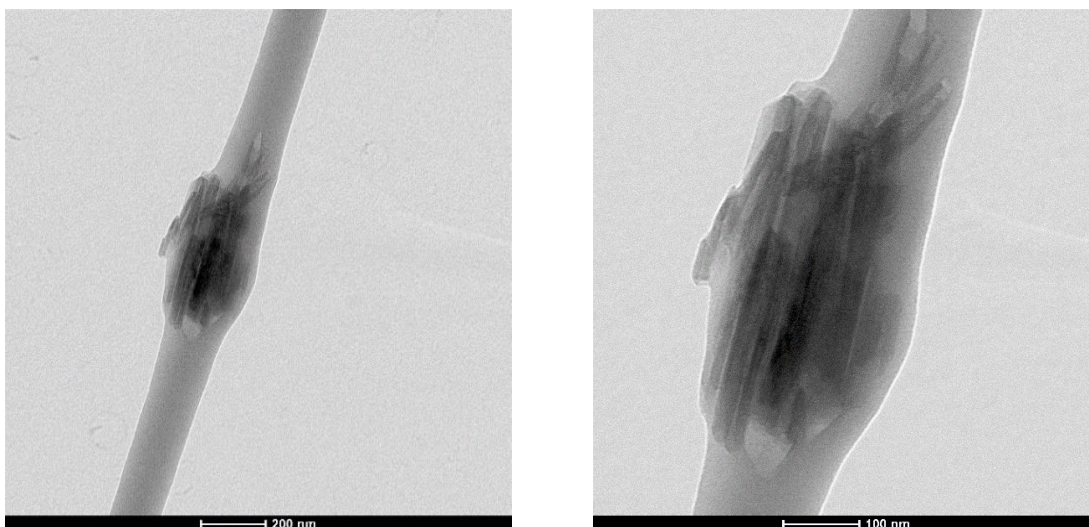


Figure 47. TEM micrographs of the composite nanofibers containing 8 wt.% m-HNTs at different magnifications.

4.2.3 Thermogravimetric Analysis (TGA)

The thermal properties of composite nanofibers were investigated using TGA analysis. Figures 48 and 49 show the TGA graphs of composite nanofibers which were produced with different unmodified and modified HNT amounts. In Figures 48 and 49, curves

overlapped and almost a single line was seen around 450°C that indicated that there was no significant change in degradation temperatures according to TGA analysis. These results are also given in Table 9. It is thought that the thermal properties did not change significantly because HNTs may not act as thermal barrier in polymer matrix [70, 71]. In addition to this, HNTs may form bundles in certain regions and may not be distributed uniformly throughout the matrix. This may lower the possibility of the existence of HNTs in every region of the matrix.

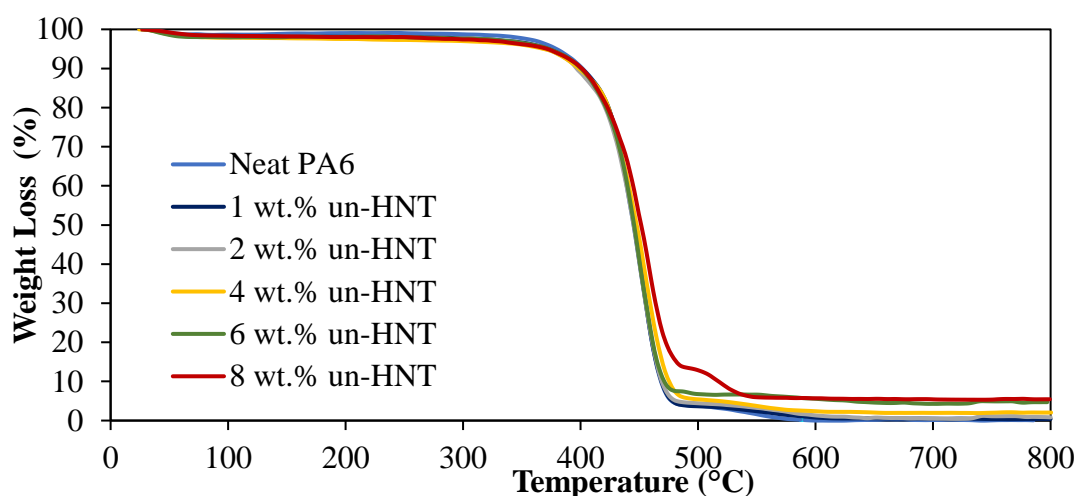


Figure 48. TGA graphs of the nanofiber nanocomposites containing different un-HNTs.

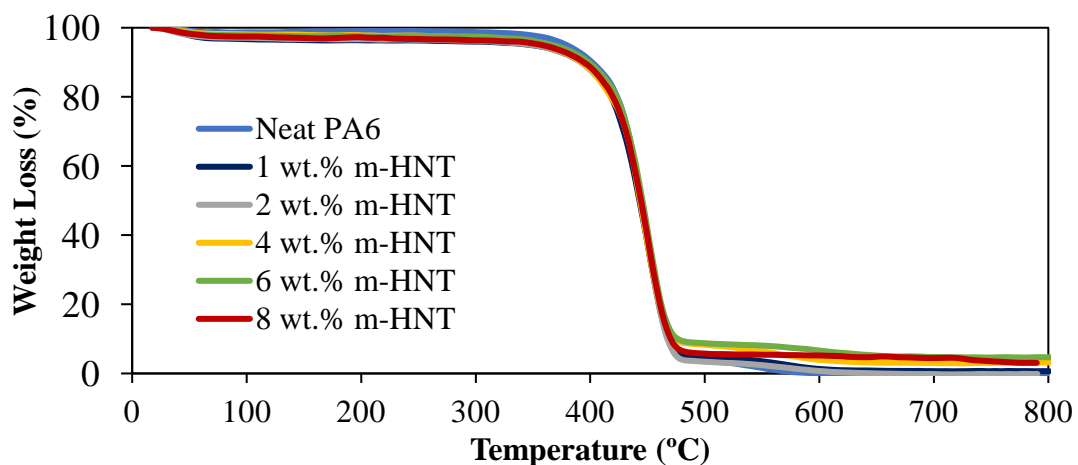


Figure 49. TGA graphs of the nanofiber nanocomposites containing different m-HNTs.

Table 9. Decomposition temperatures of un-HNTs and m-HNTs containing composite nanofibers.

Sample	Decomposition Temperature (°C)
PA6	453.53
1 wt.% un-HNT	453.92
2 wt.% un-HNT	453.00
4 wt.% un-HNT	456.05
6 wt.% un-HNT	451.51
8 wt.% un-HNT	457.31
1 wt.% m-HNT	451.92
2 wt.% m-HNT	451.44
4 wt.% m-HNT	450.29
6 wt.% m-HNT	451.43
8 wt.% m-HNT	451.91

4.2.4 Differential Scanning Calorimetry (DSC) Analysis

Thermal properties of the samples were investigated using DSC. T_g and T_m of the neat PA6 and PA6/HNTs composite nanofibers were presented in Table 10. As can be seen from the results, the addition of unmodified and modified HNTs did not cause a significant change in both T_g and T_m . The polymer chains cannot pack the nanotubes in all dimensions, and gaps may form around the nanotubes. The gaps cause to form free volume in the nanometer scale for the polymer chains. This situation is considered as the reason for unchanged T_g values [71].

Table 10. DSC data of un-HNTs and m-HNTs containing composite nanofibers.

Sample	Tg(°C)	Tm(°C)
PA6	51.79	220.79
1 wt.% un-HNT	54.38	221.09
2 wt.% un-HNT	51.73	221.73
4 wt.% un-HNT	52.91	220.60
6 wt.% un-HNT	52.51	219.77
8 wt.% un-HNT	52.86	221.27
1 wt.% m-HNT	51.80	222.88
2 wt.% m-HNT	52.16	221.17
4 wt.% m-HNT	51.44	220.12
6 wt.% m-HNT	52.27	220.84
8 wt.% m-HNT	51.91	220.92

4.2.5 Tensile Test Results

A representative tensile stress-strain graph of nanofiber mat produced using neat PA6 by electrospinning method is given in Figure 50. A similar trend was obtained for all the samples in the study. Stress-strain graphs of PA6 nanofiber mat composed of two stages. The first region shows linear elastic deformation and the second region corresponds large plastic deformation. Figure 50 indicate that the ductile like failiure of PA6 and PA6/HNTs containing samples.

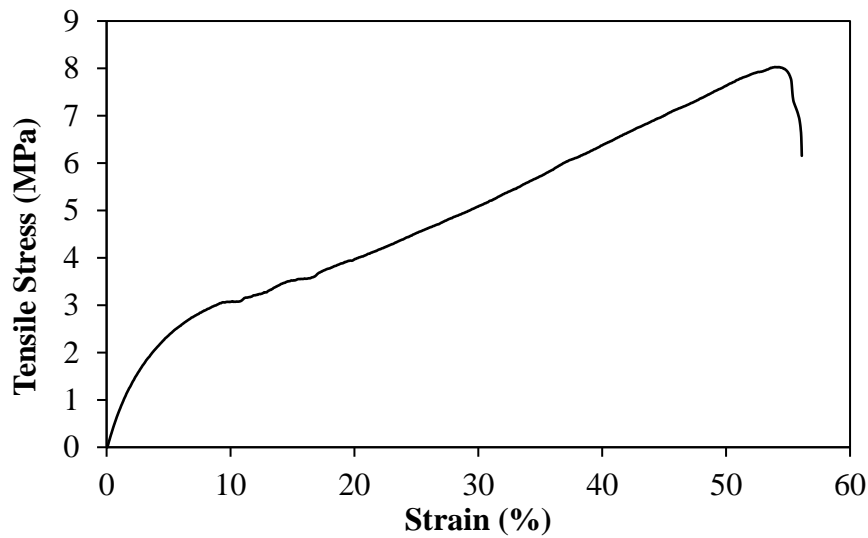


Figure 50. Representative stress-strain graph of the nanofiber mat produced using neat PA6.

Effect of different HNTs concentrations which are 1, 2, 4, 6 and 8 wt.% on tensile properties of composite nanofiber mats are illustrated in Figure 51-53 and detailed tensile test data is tabulated in Table C.4 of Appendix C. According to the tensile test results of the composites prepared using modified and unmodified HNT, tensile strength was not statistically significant change with the addition of HNTs when standard deviations were considered. It is seen from Figure 52 that the composite prepared with 1 wt.% m-HNTs has better tensile modulus value than the other composites which nearly have same modulus results. Elongation at break of 1 wt.% m-HNTs sample was slightly lower than other samples. In addition, the results of elongation at breaks were found to be lower in modified HNT additive samples compared to unmodified HNT additive samples at each concentration. The mechanical properties of composite materials depend on the effective load transfer from the matrix to the reinforcing material. This load transfer can be achieved after matrix and reinforcement have interaction each other and good dispersion. The mechanism of a strong interaction can be explained with micromechanical interlocking and chemical bond formation [40, 72].

According to the results, there was no improvement in the mechanical properties at high HNTs concentrations due to poor dispersion of nanotubes in PA6 matrix. Only the tensile modulus of the sample containing 1 wt.% m-HNTs increased slightly by the use of low amounts of HNTs and the surface modification of the nanotubes which increase the possible interaction between matrix and reinforcement. Elongation at break values were lower in samples containing modified HNTs because modification provides better distribution resulted in limited chain motions of PA6.

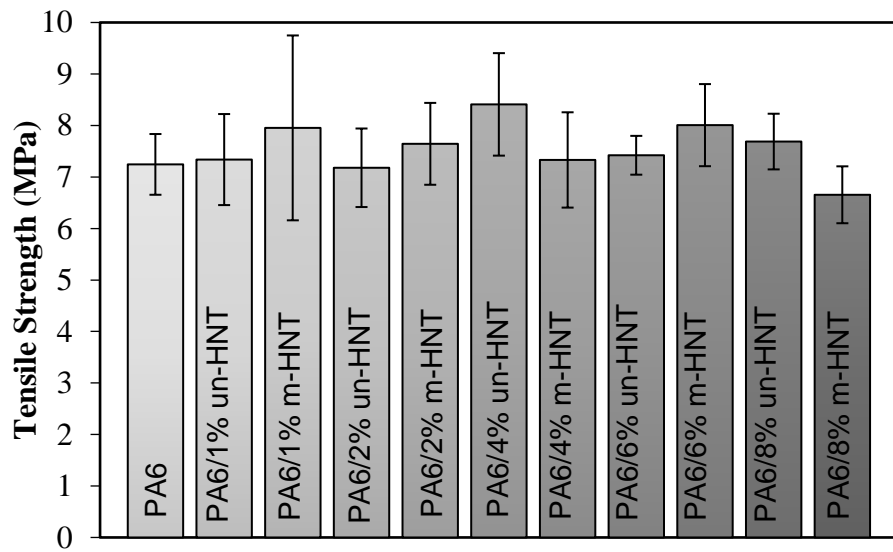


Figure 51. Tensile strengths of un-HNTs and m-HNTs containing composite nanofiber mats.

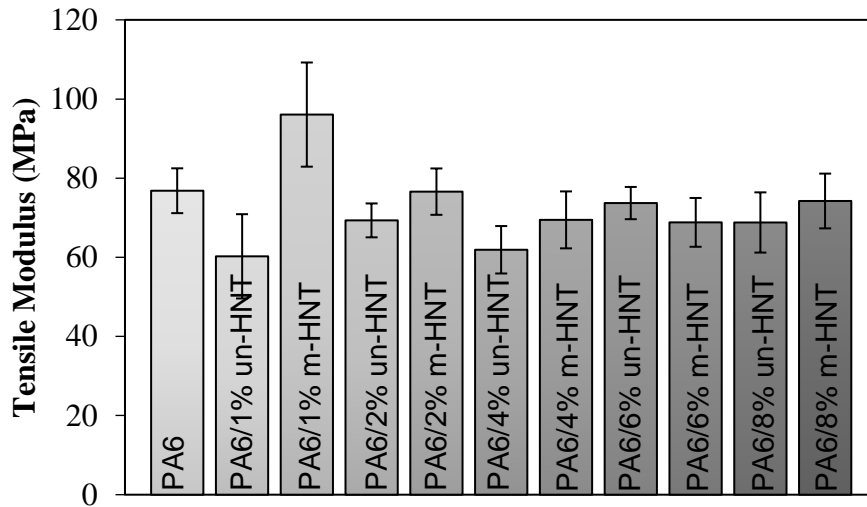


Figure 52. Tensile moduli of un-HNTs and m-HNTs containing composite nanofiber mats.

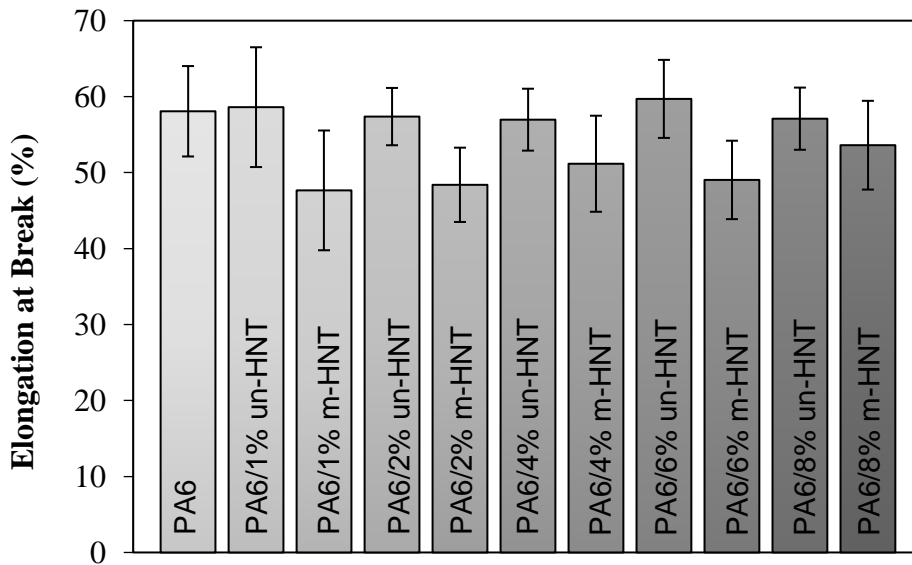


Figure 53. Elongation at break of un-HNTs and m-HNTs containing composite nanofiber mats.

Morphological characterization was performed by SEM analysis to the rupture surface of fibers. The SEM images of these surfaces are shown in Figures 54-59. Figure 54 shows the SEM image obtained from the rupture surface of the neat PA6 sample. When

the surfaces of HNTs containing samples were examined, agglomerations were not observed in samples including 1 wt.% un-HNTs and m-HNTs (Figure 55). When SEM images given for higher concentrations were analyzed (Figure 56-59), agglomerations on the rupture surfaces were clearly seen, especially in un-HNT containing samples. Although agglomerations decreased by surface modification applied to HNTs, they were not sufficient to improve mechanical properties. Therefore, the best tensile modulus value was obtained in the sample containing 1% m-HNTs. The fibers in this sample were more uniform and agglomerations were not observed on the rupture surfaces according to SEM analysis.

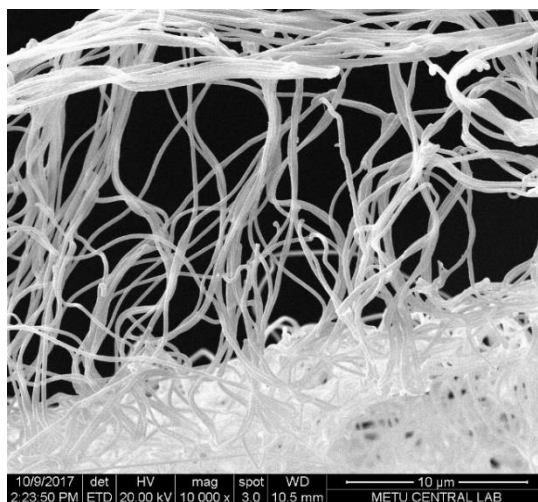


Figure 54. SEM micrograph of the rupture surface of the neat PA6 sample after tensile test.

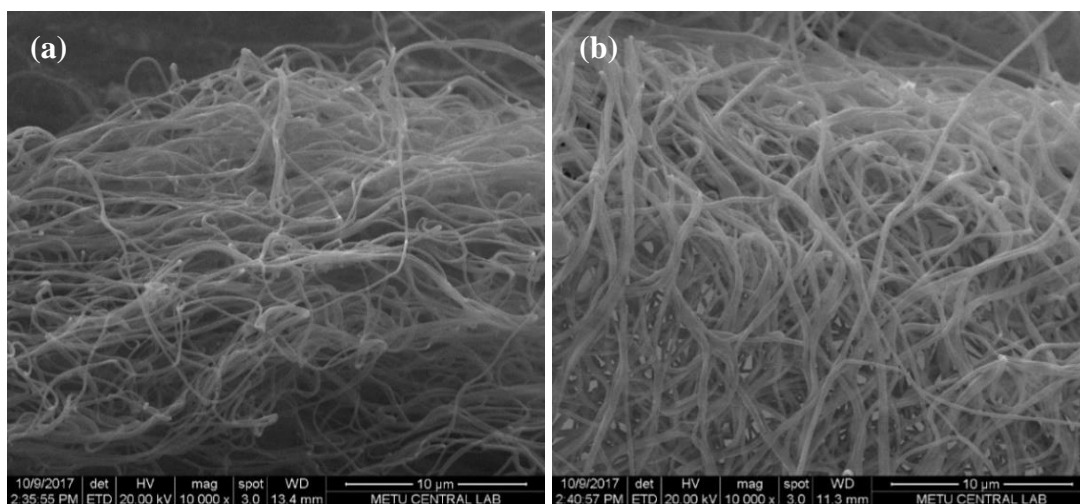


Figure 55. SEM micrograph of the rupture surface of the composite nanofibers containing 1 wt.% (a) un- HNTs, (b) m-HNTs after tensile test.

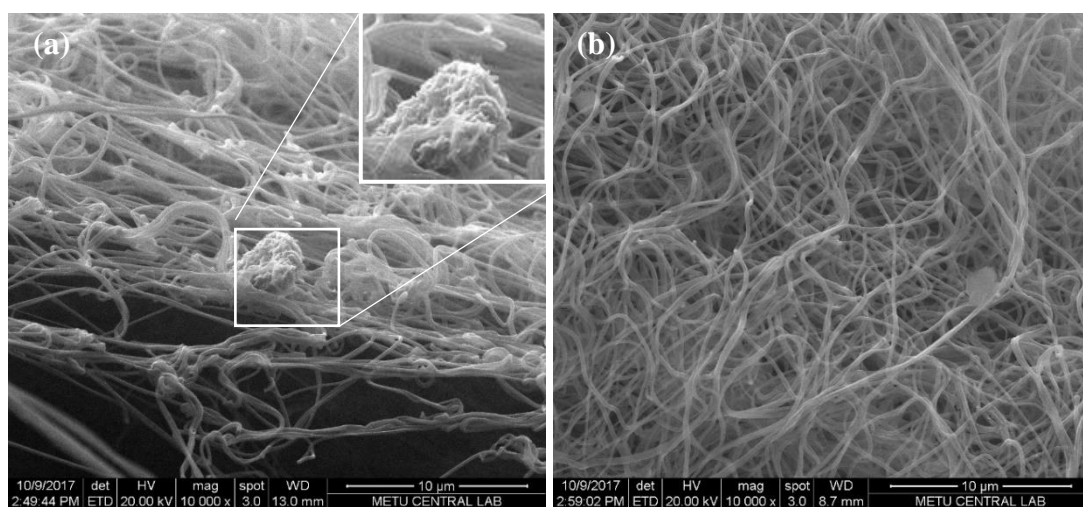


Figure 56. SEM micrograph of the rupture surface of the composite nanofibers containing 2 wt.% (a) un- HNTs, (b) m-HNTs after tensile test

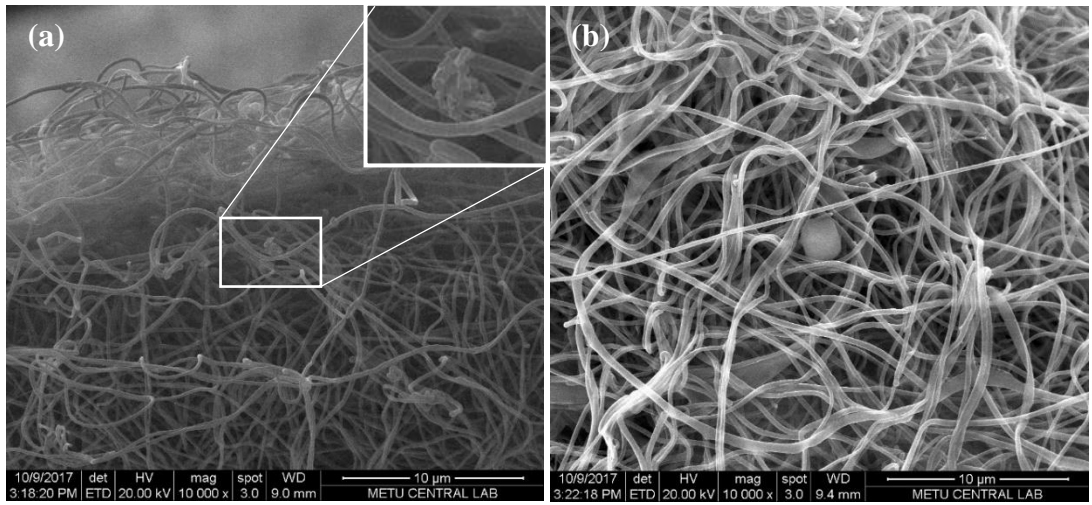


Figure 57. SEM micrograph of the rupture surface of the composite nanofibers containing 4 wt.% (a) un- HNTs, (b) m-HNTs after tensile test

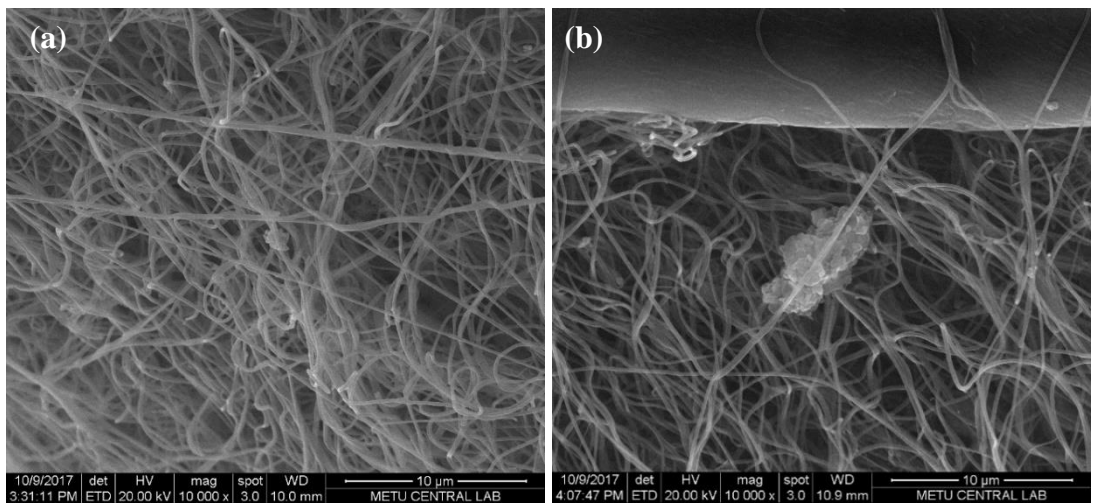


Figure 58. SEM micrograph of the rupture surface of the composite nanofibers containing 6 wt.% (a) un- HNTs, (b) m-HNTs after tensile test

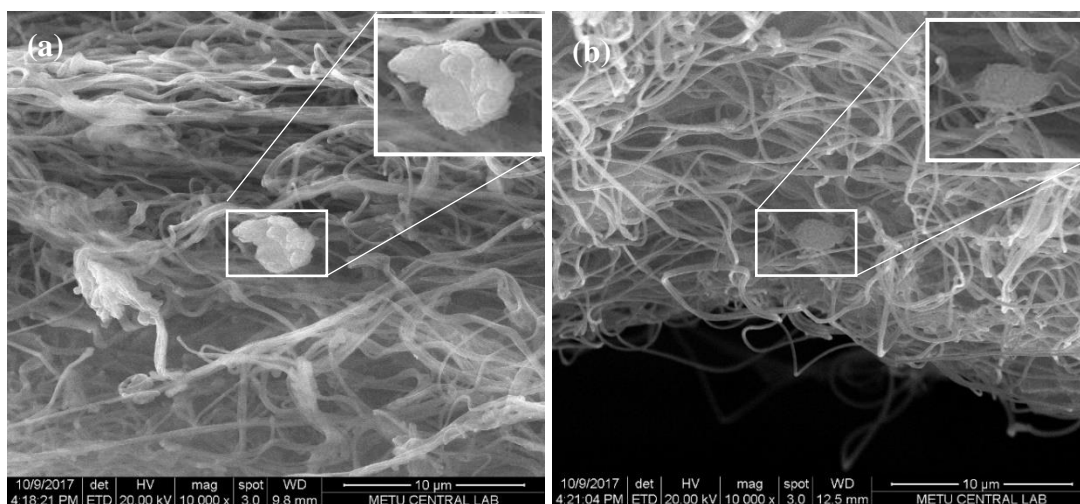


Figure 59. SEM micrograph of the rupture surface of the composite nanofibers containing 8 wt.% (a) un- HNTs, (b) m-HNTs after tensile test

As a result of tensile tests, it was concluded that the addition of 1 wt.% m-HNTs to PA6 increased the tensile modulus 25% with respect to pure PA6. This showed that HNTs made the polymer matrix more rigid and strong. In this sample, the elongation at break value decreased 18% compared to PA6. The reason for this can be explained by the good distribution of HNTs within the polymer matrix. Well-dispersed HNTs were reduced the elongation at break by restricting the movement of nanofibers.

4.3 Degradation of Electrospun Mats under Chemical Vapors

As a result of the optimization studies, a total of 30 nanofiber mats, 10 of each including PA6 and PA6 composite nanofibers containing 1 and 8 wt.% m-HNTs were exposed to HCl, acetone, toluene and water vapors. During the measurements, the samples were hanged via clips on the sample holder that was previously mentioned in the experimental part. Produced mats were weighed with clips attached on and mass change was recorded. The mass change was calculated by subtracting the initial weight (M_i) from the weight (M_t) at the time of measurement. Weight change of the samples versus time graphs are given in Figures 60-63.

Figure 60 shows the change in the weight of the samples, which were exposed to the aqueous HCl solution mixture. Graph showed that there was a linear increase in the

weight of the samples with time. The reason for this rapid and linear increase was the increase of the weight of the clips due to corrosion in the acid environment. The weight change in the samples could not be determined due to the increase in the mass of the clips because samples weighed with clips.

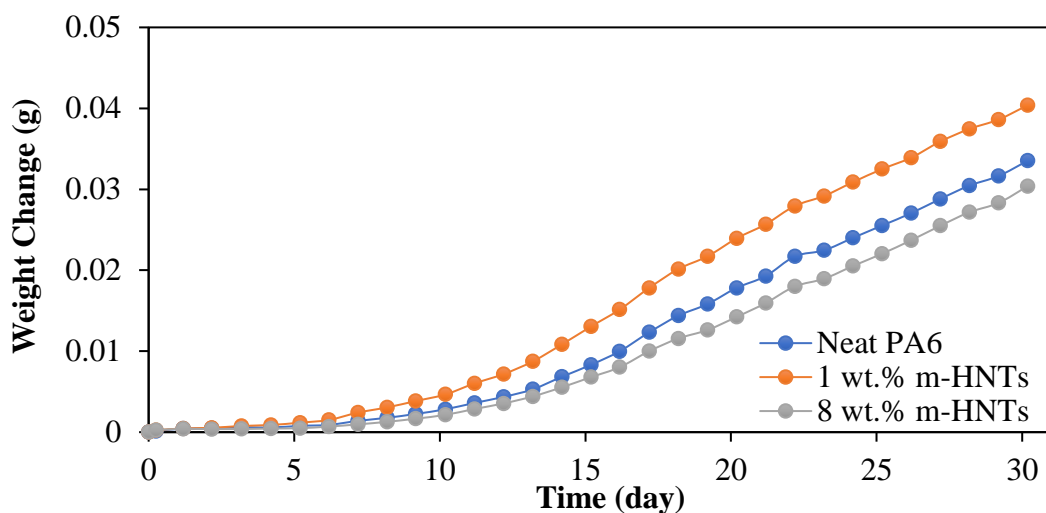


Figure 60. Weight change graph of the samples exposed to HCl vapor.

Figure 61 shows the change in the weight of the samples in the aqueous acetone solution mixture. There was no increase in the weight of the clips in the acetone vapor environment. The weight increase in the samples was calculated and found that mass increase in neat PA6 mats was higher than HNTs containing samples. This can be explained by the increase of the degradation resistance of PA6 against acetone vapor by the addition of HNTs. In addition, weight increase in the samples containing 1 wt.% m-HNTs was more than the samples containing 8 wt.% m-HNTs. Since HNTs have a high aspect ratio, it creates pathways within the polymer matrix and reduces water uptake [72].

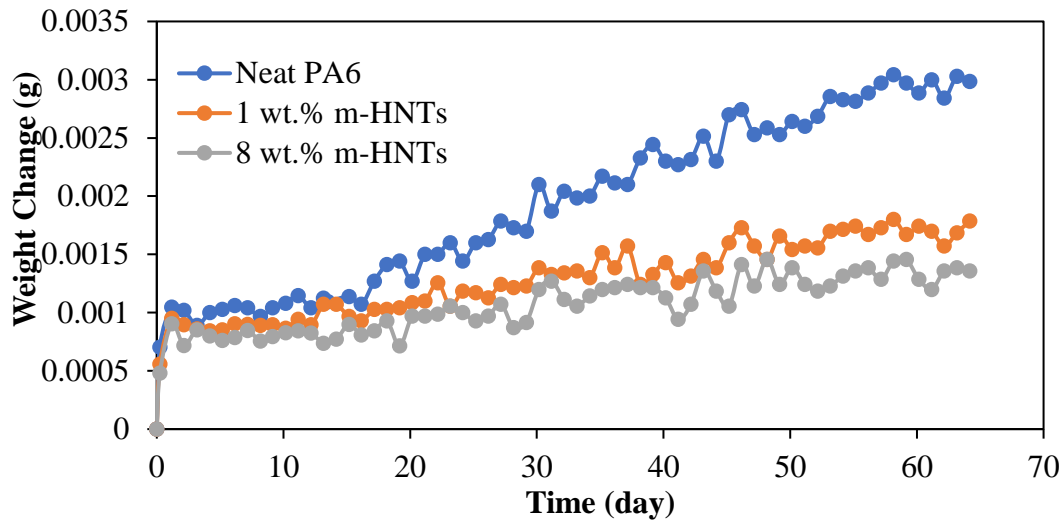


Figure 61. Weight change graph of the samples exposed to acetone vapor.

Figure 62 shows the change in the weight of the samples in the toluene vapor. Graphs showed that weight change slowed for all concentrations after 10 days. Weight change in neat PA6 samples was higher than composite fibers and this is an expected trend. However, the non-polar solvent, toluene, has less or no interaction with the PA6, which is a polar polymer [73].

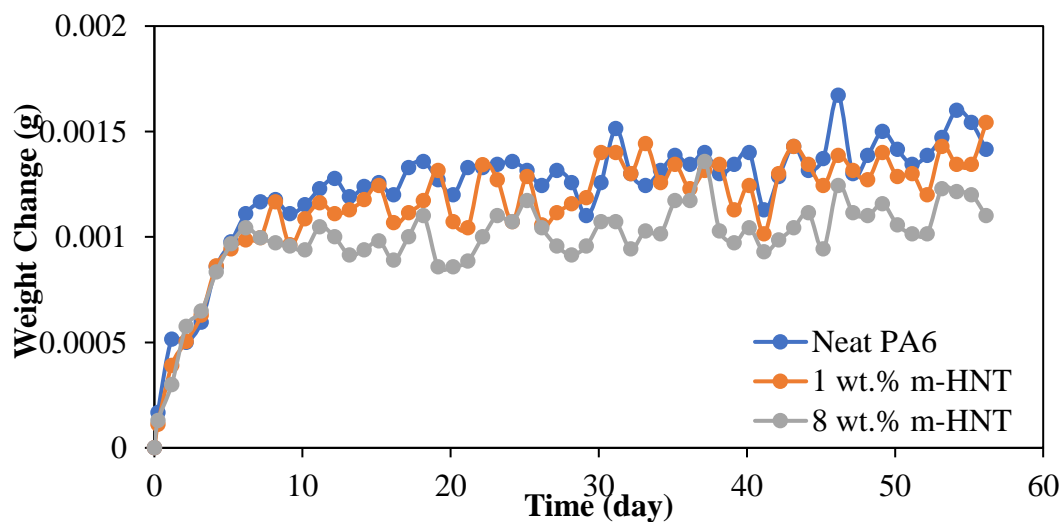


Figure 62. Weight change graph of the samples exposed to toluene vapor.

Figure 63 shows the change in the weight of the samples which were exposed to the water vapor. In the figure, weight changes fluctuated which may be caused by degradation of PA6 in the water environment. Water vapor can pass through the porous structure of the mats and rapid evaporation of solvent can occur during the measurement due to high surface area of nanofibers. Because of these fluctuations, mass changes could not be interpreted clearly. However, in general, it is seen that the change in weight of neat PA6 was the lowest and the weight of the samples containing 1 and 8 wt.% m-HNTs changed almost equally. PA6 is known to be degraded in water vapor environment. Degradation of polymers is generally determined by a decrease in molecular weight [74]. It is thought that the weight change in neat PA6 samples was less than the HNTs containing samples because of this decrease in the molecular weight due to degradation.

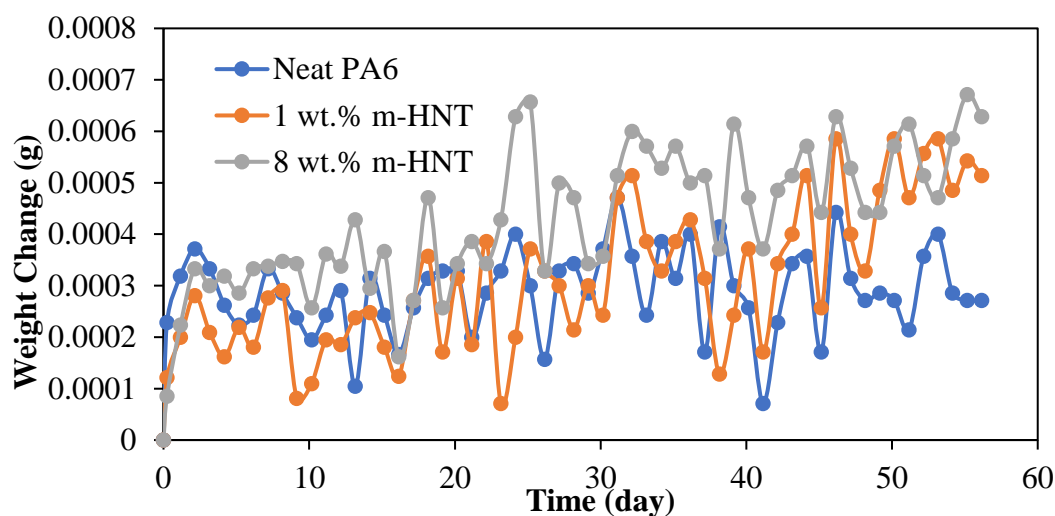


Figure 63. Weight change graph of the samples exposed to water vapor.

In order to eliminate the mentioned problems on determination of weight change and minimize the fluctuations in the weight change graphs, new setup was prepared and the chemical vapor degradation tests were repeated. Neat PA6 and the composites containing 1 and 8 wt.% m-HNTs were exposed to hydrochloric acid, acetone, toluene and water vapors for one week. While selecting the one-week experiment period, the

previous studies were taken into consideration and the time of weight change was fixed. Weight change graphs for new setup are given in Figures 64-67. Each point in the graphs shows the daily average of the measurements made at the intervals specified in the experimental studies part.

Figure 64 shows the weight change (%) of the samples exposed to HCl vapor. The highest increase in weight was found in the samples containing 1 wt.% m-HNTs. It is seen that the results of neat PA6 and 8 wt.% m-HNTs containing samples were close to each other, but the increase in the mass of neat PA6 nanofibers is higher. The reason of increase in the weight of the samples containing 1 wt.% m-HNTs that was higher than the neat samples were thought to be due to the decrease in the molecular weight of the neat fibers due to degradation [75]. The decrease in molecular weight reduced the weight increase.

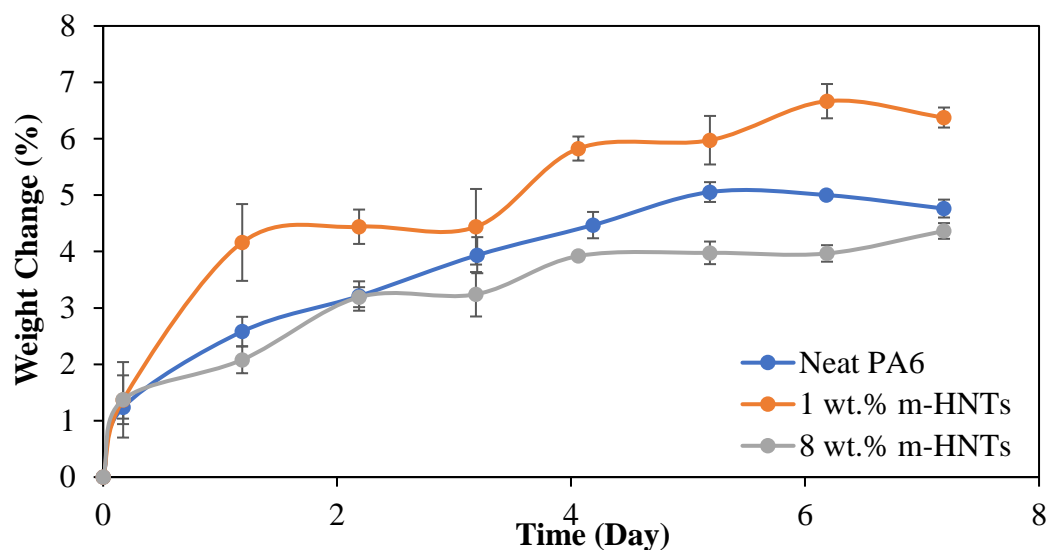


Figure 64. Percent weight change graph of the samples exposed to HCl vapor.

The weight change (%) graph of the samples exposed to acetone vapor is given in Figure 65 for the new setup. The graph showed that the increase in weight in neat samples was higher than other concentrations especially after 4 days of exposure. Furthermore, weight change in the samples containing 1 wt.% m-HNTs was higher

than 8 wt.% m-HNTs containing ones. This is explained by the increase in the resistance to degradation by increasing the amount of HNTs.

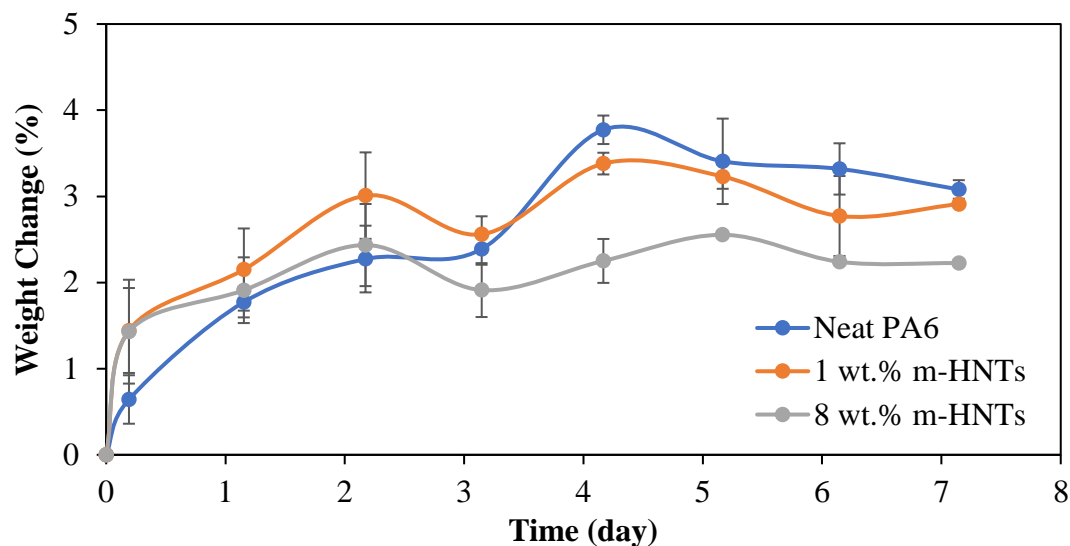


Figure 65. Percent weight change graph of the samples exposed to acetone vapor.

The weight change (%) graph of the samples exposed to toluene vapor for the new setup is given in Figure 66. Results showed that weight increase in the neat PA6 and 8 wt.% m-HNTs containing samples were close to each other and higher than the 1 wt.% m-HNTs containing samples. An apparent trend could not be obtained since only weak interaction occurs between toluene and polymer matrix. The effect of these weak interactions become more obvious as there are always structural differences between electrospun mats even when the same production parameters are used.

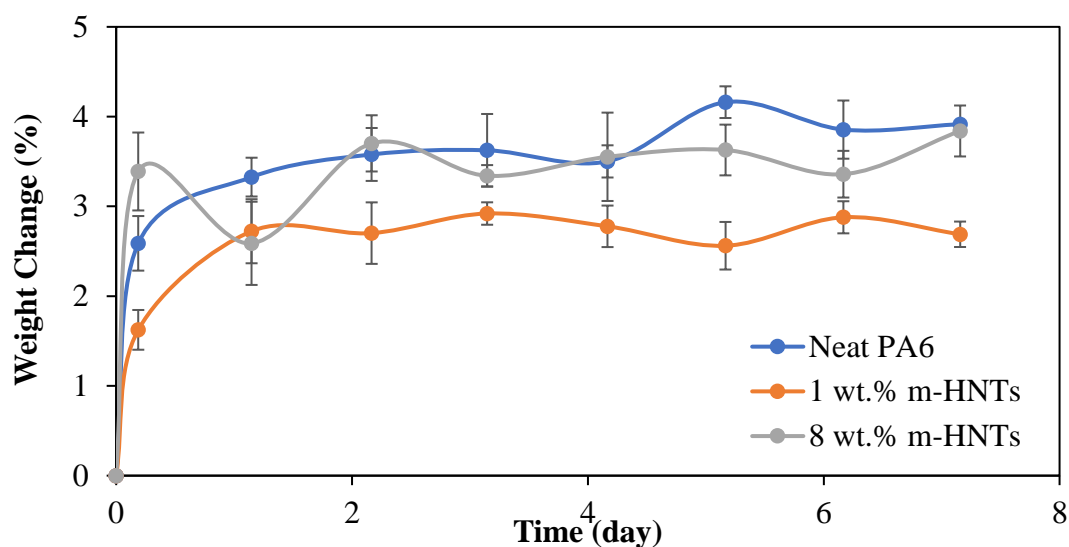


Figure 66. Percent weight change graph of the samples exposed to toluene vapor.

Figure 67 shows the weight change (%) graph of the samples exposed to water vapor for the new setup. The highest weight change (%) result was obtained at neat PA6 samples which indicated that neat polymer is more sensitive to water vapor than the composite nanofibers. When 1 and 8 wt.% m-HNTs containing samples were compared, 8 wt.% m-HNTs containing samples gave higher weight change (%) results. This can be explained that in the sample containing 1 wt.% m-HNTs, HNTs showed a barrier effect on mass transfer due to the better dispersion within the polymer matrix [76].

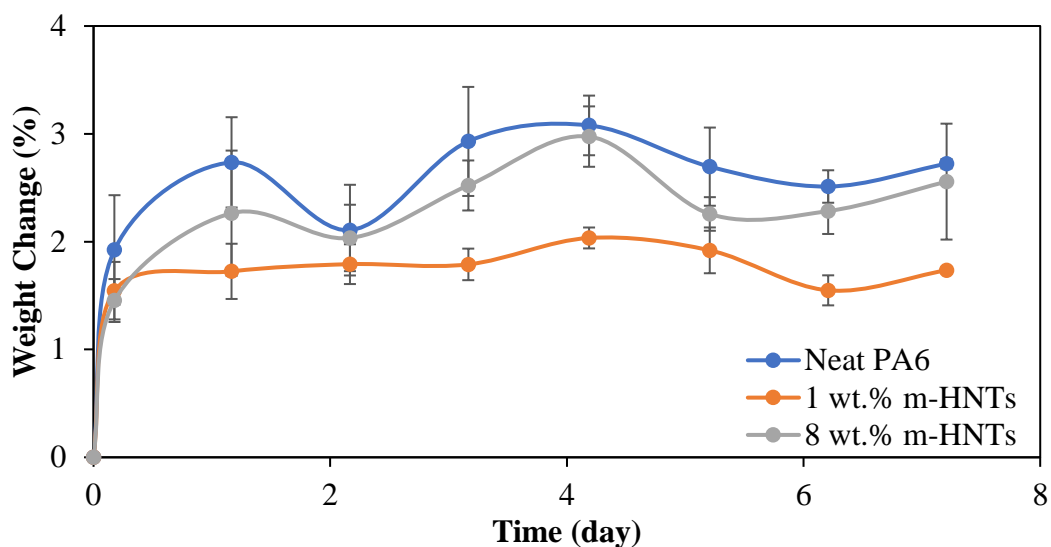


Figure 67. Percent weight change graph of the samples exposed to water vapor.

The data obtained for the polymer and the solvent system are generally expressed as normalized mass change M_t/M_∞ that is the ratio of the mass change in the time t and the mass change in the equilibrium. Fickian diffusion mechanism allows the diffusion coefficient to be obtained from the graph of normalized mass change as a function of the square root of time [53].

For the calculation of the diffusion coefficients, the normalized weight change of the samples exposed to different chemical vapors was plotted as a function of square root of time and shown in Figures 68-71. Sample calculation of the diffusion coefficient was given in Appendix D. In addition, the weight changes in the equilibrium (M_∞) which was obtained by taking the average of the last 3 measurements due to the fluctuations and calculated diffusion coefficient values for all samples exposed to different chemical vapors are given in Table 11. The diffusion coefficient can be used to compare the diffusion rate of solvents into neat polymers with composites and to determine the time required to achieve the equilibrium weight change of the sample [44].

Figure 68 shows that the normalized weight change of HCl exposed samples as a function of square root of time. At initial state, graph is linear and M_t/M_∞ value in this

stage should be less than 0.5 to obey the Fickian diffusion. Graph showed that the initial weight gains were close to each other. According to the results which are reported in Table 11, diffusion coefficient decreased as the HNTs amount increased for HCl vapor exposed samples. This can be explained by the fact that the average path required for the solvent to move through the sample increases due to barrier effect in the presence of HNTs [44, 77]. When the weight changes in the equilibrium were compared, it was seen that 1 wt.% m-HNTs containing sample had highest result which determined from the average of the last three point. The reason of the lower increase in weight of the neat sample can be explained by the degradation of the polymer in the strong acid vapor environment resulting in the decrease in the molecular weight [53].

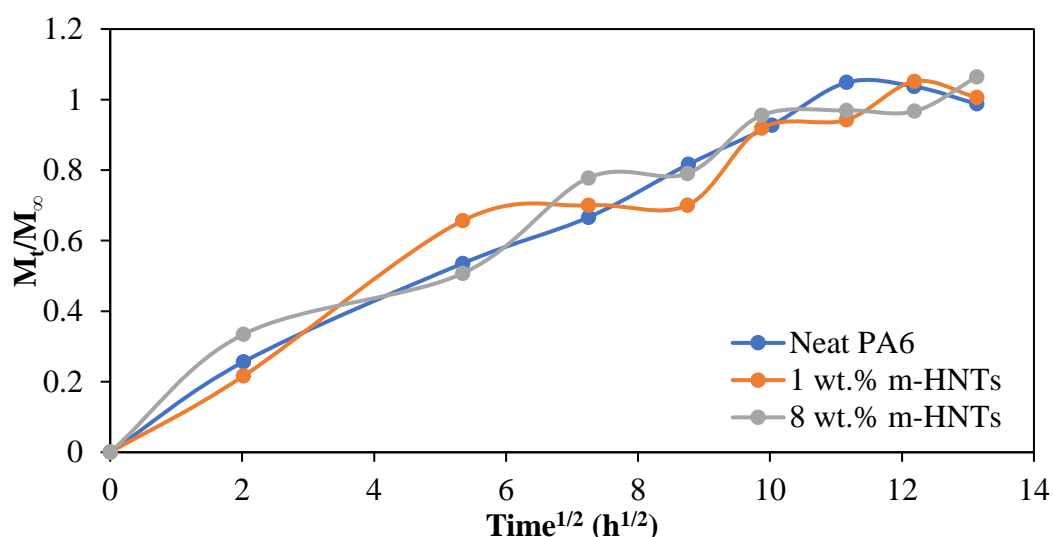


Figure 68. Normalized weight increase as a function of square root of time for HCl exposed samples.

The graphs on normalized weight change of acetone exposed samples as a function of square root of time of the samples exposed to acetone vapor (Figure 69) shows that the slope in the initial state was the highest for 8 wt.% m-HNTs containing samples and the lowest for neat samples. When the calculated diffusion coefficients were compared (Table 11), similar results were obtained. The reason of higher diffusion coefficient at high HNTs concentration can be explained by gaps in the structure located around agglomerations. These spaces caused the evaporated solvent could enter the structure

rapidly [77]. Acetone that has low boiling point was able to fill faster in the gaps at the beginning of experiment. Although the diffusion coefficient was lower for the neat PA6, the weight change in equilibrium was highest for this sample. This shows that the presence of HNTs limited the mass change of the material in equilibrium and less solvent was retained in the structure.

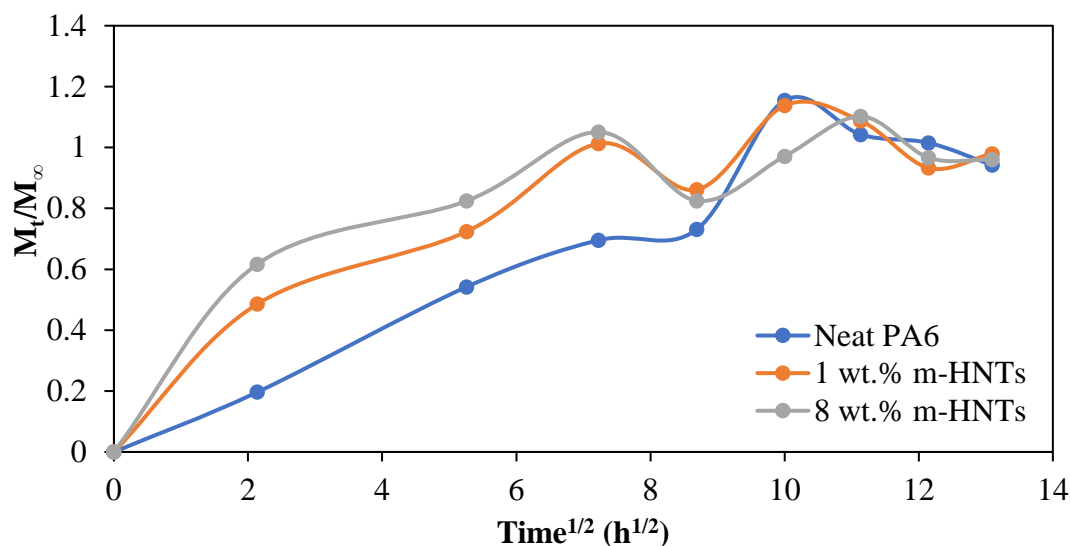


Figure 69. Normalized weight increase as a function of square root of time for acetone exposed samples.

Normalized weight change of toluene exposed samples as a function of square root of time is seen in Figure 70. The slope in the initial state was the highest for 8 wt.% m-HNTs and the lowest for 1% m-HNTs containing samples. Similar results were obtained for calculated diffusion coefficients. It is thought that toluene, a non-polar solvent, may only have a physical interaction with PA6. Therefore, differences in the structure, which can come from the nature of the electrospinning method, can be shown as the reason of the changes in diffusion coefficients and weight change in equilibrium.

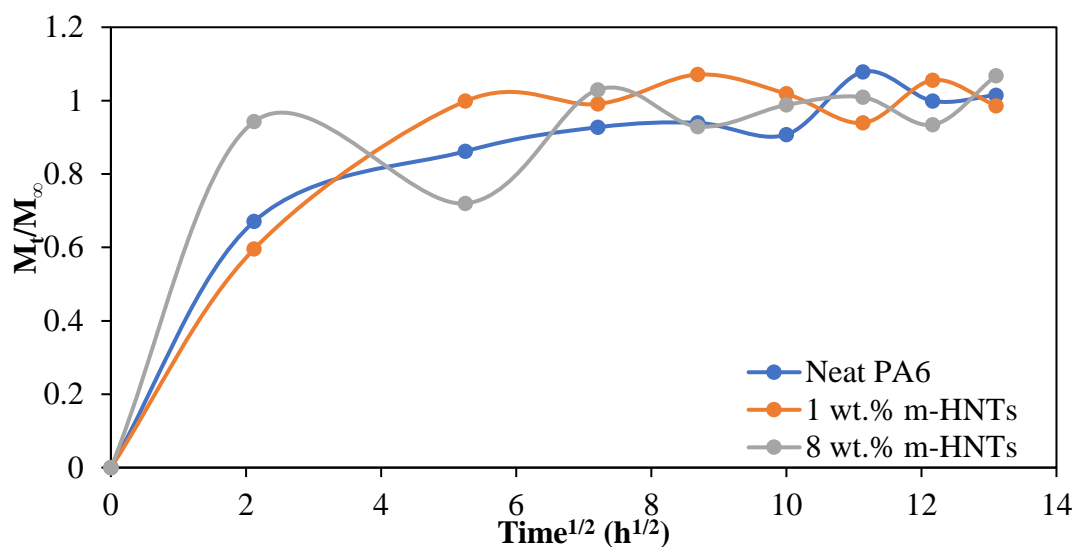


Figure 70. Normalized weight increase as a function of square root of time for toluene exposed samples.

When the results of the samples exposed to water vapor are examined, it can be seen in Figure 71 that the slope in the initial state was the highest for the 1 wt.% m-HNTs and the lowest for the 8 wt.% m-HNTs containing samples. The same trend was obtained for the diffusion coefficients. The fact that 1 wt.% m-HNTs containing composite kept water in the structure faster than others in the early times can be explained by the differences in the structure of the mats produced by electrospinning in each production. The increase of gaps in the structure may be related to the acceleration of the diffusion in the early times. In addition to these, increase in the weight changes were compared and the highest increase was obtained in neat sample and lowest increase was obtained in 1 wt.% m-HNTs containing sample. The high HNTs concentration was resulting in weight increase in the samples containing 8 wt.% m-HNTs was higher than the 1 wt.% m-HNT containing samples. HNTs have a highly hydrophilic structure [78] and this feature is reduced by surface modification. In our previous study, water contact angle measurements were conducted to understand the effect of surface modification. After modification contact angle of HNTs increased from 13.90° to 26.30° [79]. These results showed that the hydrophobic properties of HNTs increased with modification. However, it is thought that HNTs do not

completely lose its hydrophilic character. As a result, at the high additive concentrations, HNTs keep the water in its structure and weight change increase can occur s by this way [44].

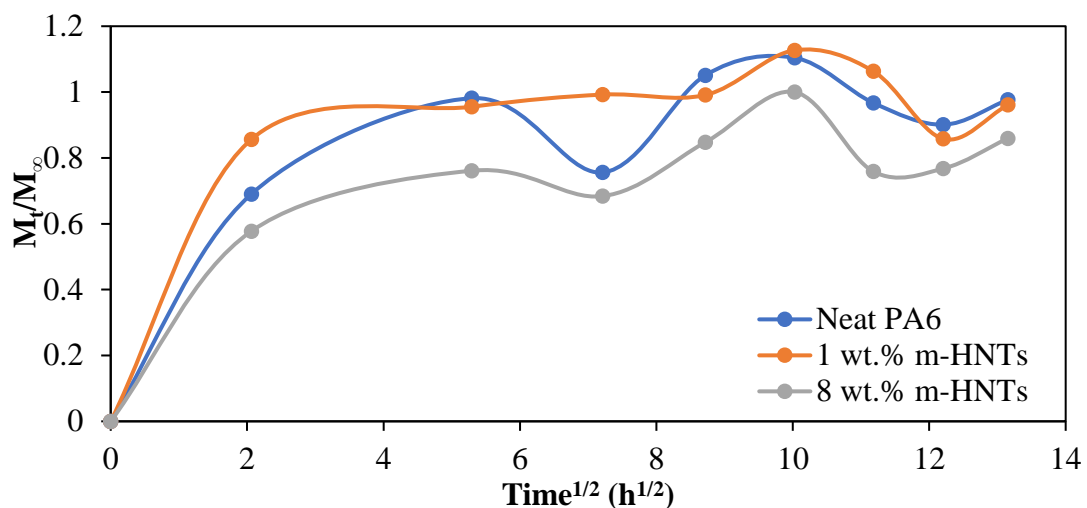


Figure 71. Normalized weight increase as a function of square root of time for water exposed samples.

Table 11. Weight changes at equilibrium and diffusion coefficients of the samples exposed to different chemical vapors.

Sample	HCl		Acetone		Toluene		Water	
	M_{∞} [%]	D [m^2/s] x 10^{15}	M_{∞} [%]	D [m^2/s] x 10^{15}	M_{∞} [%]	D [m^2/s] x 10^{15}	M_{∞} [%]	D [m^2/s] x 10^{15}
0%	4.82	2.76	3.27	2.29	3.86	15.69	2.79	11.36
1%	6.34	1.43	2.97	4.94	2.73	7.36	1.81	15.40
8%	4.10	0.94	2.32	6.32	3.59	25.89	2.52	8.77

4.3.1 Fourier Transformed Infrared (FTIR) Spectroscopy Analysis

FTIR characterization was performed to observe the structural differences between unexposed and chemical vapor exposed electrospun mats. Infrared (IR) spectra is used to characterize the structure and package form of the polymer chains and crystallinity

of semi-crystalline polymers [80]. Analyses show changes in the molecular structure after potential chemical interaction.

The expected FTIR bands for PA6 are listed in Table 12. FTIR analysis gives the characteristic peaks of PA6 at wavenumbers of 1540, 1640 and 3300 cm^{-1} which represent amide II band (N–H deformation and stretching vibration of the C–N bond), amide (C=O axial deformation) and N-H stretching band, respectively. In addition, wavenumber of 1201 cm^{-1} represents amide III crystalline peak: symmetrical angular deformation out of plane.

Table 12. The expected FTIR bands for PA6 [80, 81].

Wavenumber (cm^{-1})	Definition
1201	amide III, crystalline peak: symmetrical angular deformation out of plane
1263	C-O stretching
1440	CH ₂ deformation
1460	C=C atomic stretching
1540	N–H bending vibration and C–N axial deformation, amide II
1640	C=O axial deformation, amid I
2858	CH ₂ axial deformation
2926	CH ₂ axial deformation
3080	N–H angular deformation in the plane
3300	N–H stretching

The FTIR spectra for the samples exposed to different chemical vapors in old setup are given in Figures 72-75, for samples used in the setup are given in Figures 76-79. It can be seen from the figures, there was a slight decrease in absorbance of some characteristic bands after exposing to hydrochloric acid, acetone and water vapors. In addition, some slight shifts of bands were determined after chemical vapor exposure. In order to be able to see these changes better, the comparative plots were drawn for related regions and given in Figures 72- 75 (b), respectively, for the samples exposed to HCl, acetone, toluene and water vapors in the old setup. For the new setup, the

comparative graphs are presented in Figures 76-79 (b), respectively, for the samples exposed to HCl, acetone, toluene and water vapors, respectively. FTIR spectra obtained from the analyses of the samples from the old and the new setup had the same results.

FTIR analyses show that the absorbance values in the bands of 1640 cm^{-1} , 1540 cm^{-1} and 1440 cm^{-1} decreased after chemical interaction. The decrease in absorbance of characteristic peaks indicates that functional groups were spent during degradation [50]. However, presence of HNTs slightly prevented the decrease in absorbance of characteristic peaks. In addition, changes in the bands of 1201 cm^{-1} and 1260 cm^{-1} can be responsible for the changes in the crystalline structure of the samples after interaction with chemical vapors. After degradation of polymers, crystalline structure can change and thermal and mechanical properties of the materials cannot be maintained.

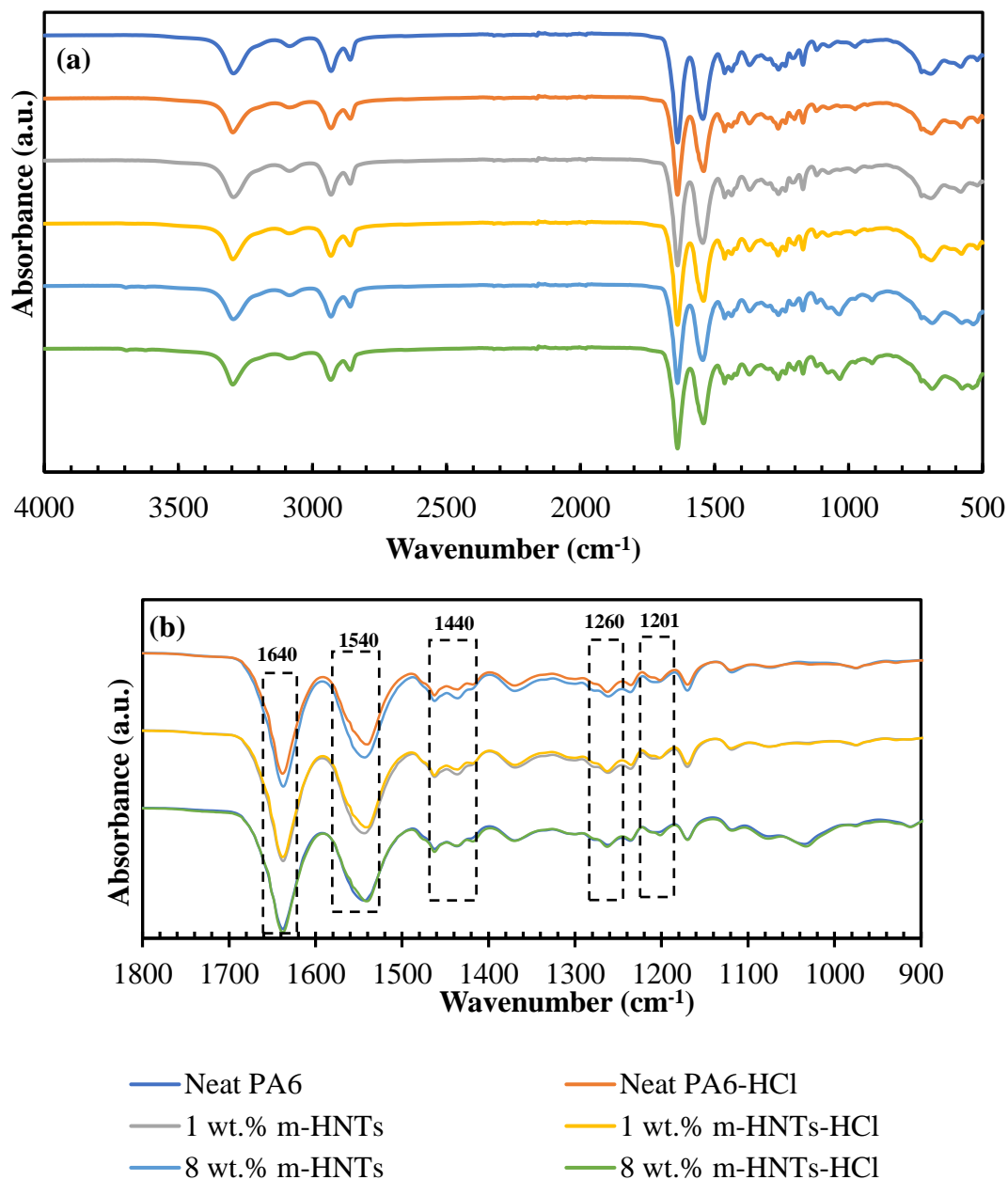


Figure 72. (a) FTIR graphs (b) zoomed FTIR graphs of the samples exposed to HCl vapor in the old setup.

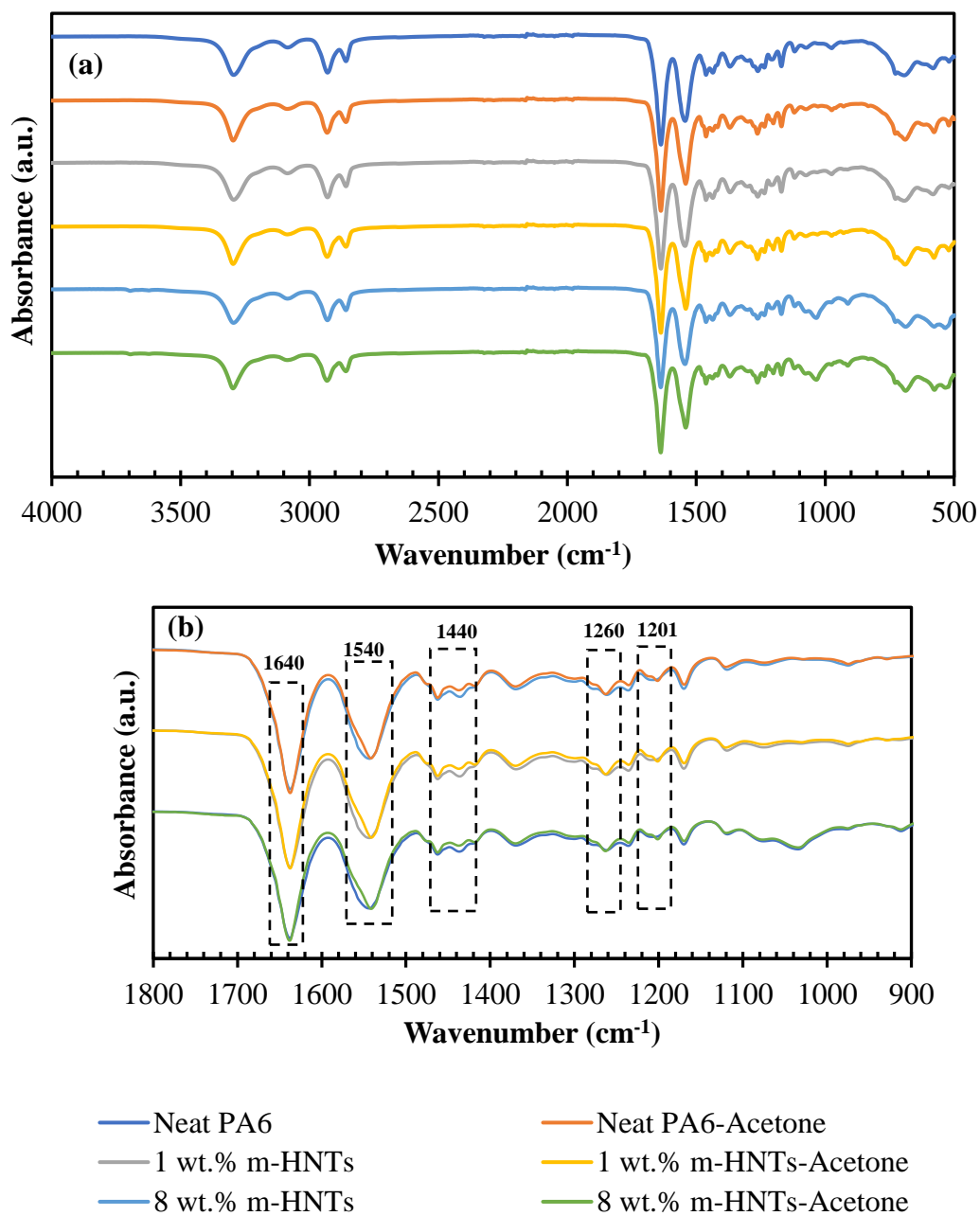


Figure 73. (a) FTIR graphs (b) zoomed FTIR graphs of the samples exposed to acetone vapor in the old setup.

When FTIR spectra of the samples exposed to toluene vapor were examined, it was seen that there was no significant change in bond absorption and positions. Toluene is a non-polar solvent and interactions of polyamides with less polar or non-polar

solvents such as toluene are limited or weak. The type of the solvent and interaction between the polymer and the solvent have an importance role on nylons permeability [73].

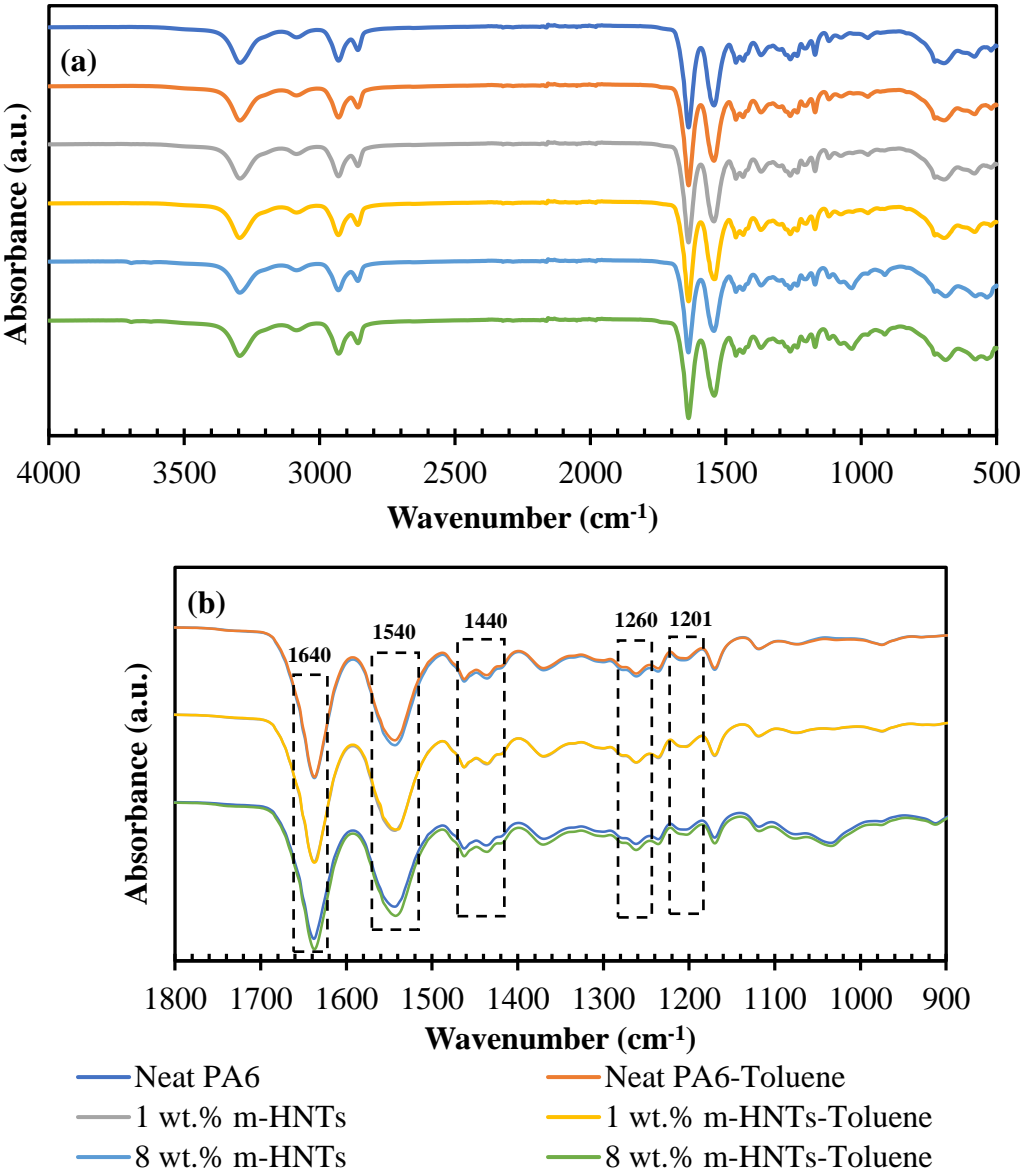
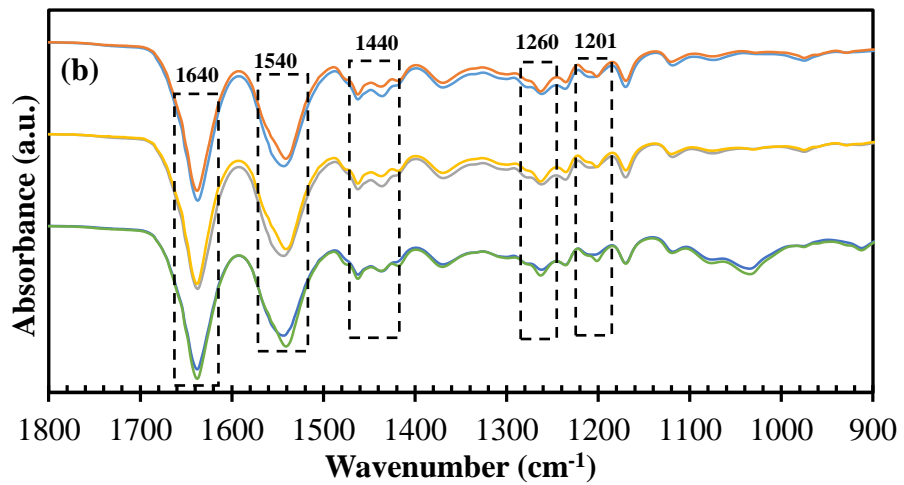
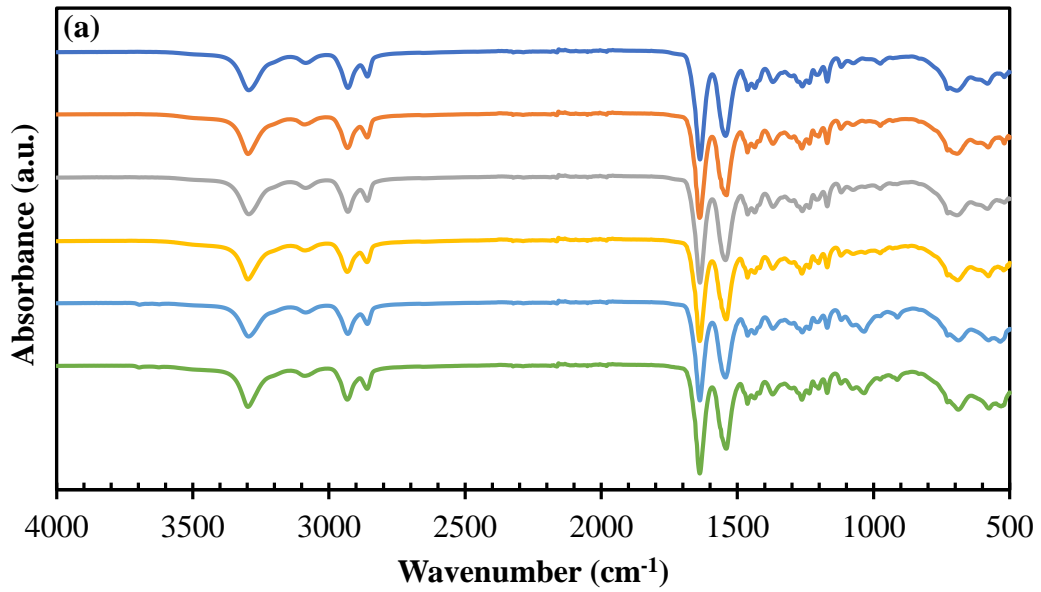


Figure 74. (a) FTIR graphs (b) zoomed FTIR graphs of the samples exposed to toluene vapor in the old setup.



- Neat PA6
 - 1 wt.% m-HNTs
 - 8 wt.% m-HNTs
- Neat PA6-Water
 - 1 wt.% m-HNTs-Water
 - 8 wt.% m-HNTs-Water

Figure 75. (a) FTIR graphs (b) zoomed FTIR graphs of the samples exposed to water vapor in the old setup.

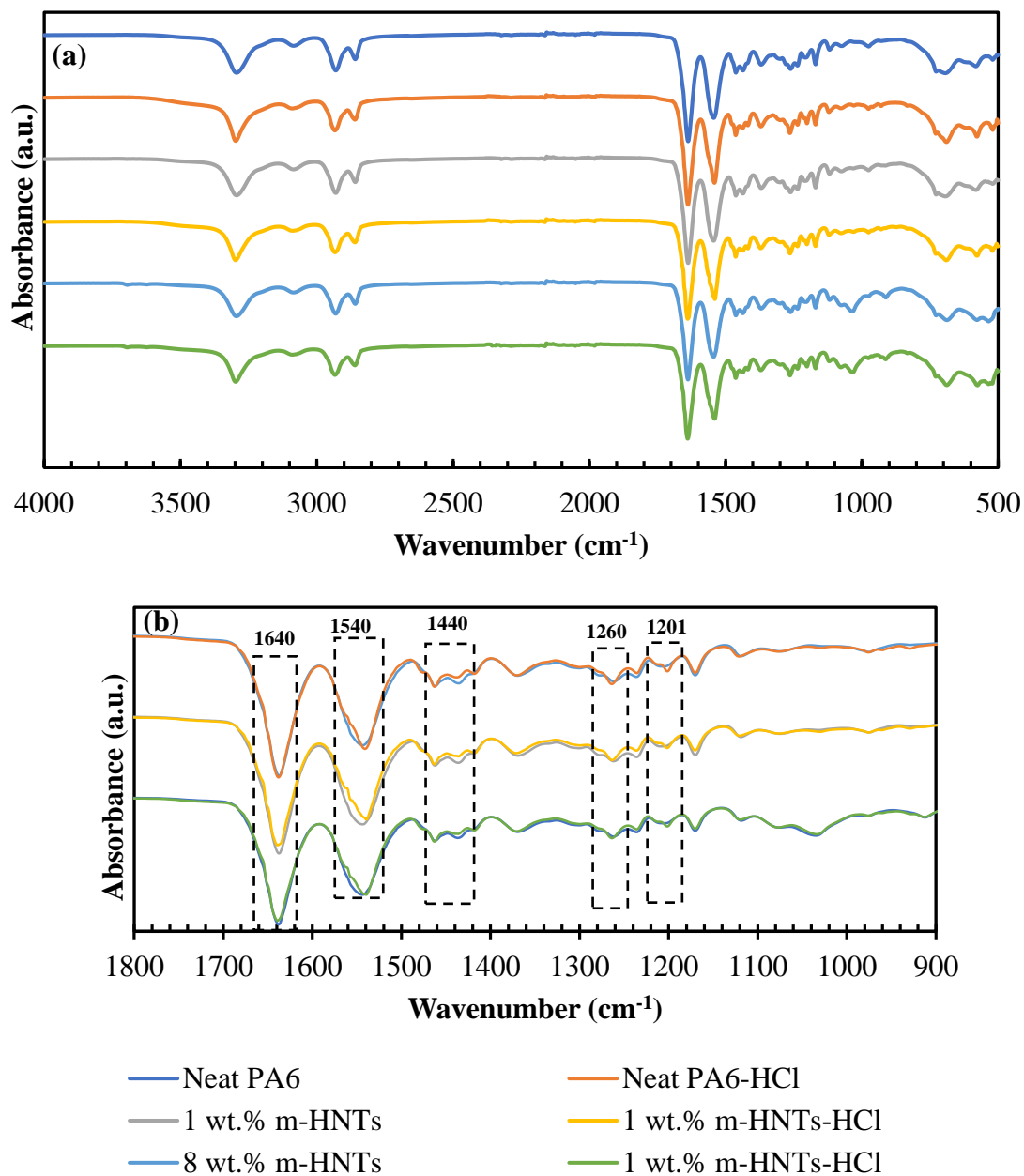


Figure 76. (a) FTIR graphs (b) zoomed FTIR graphs of the samples exposed to HCl vapor in the new setup.

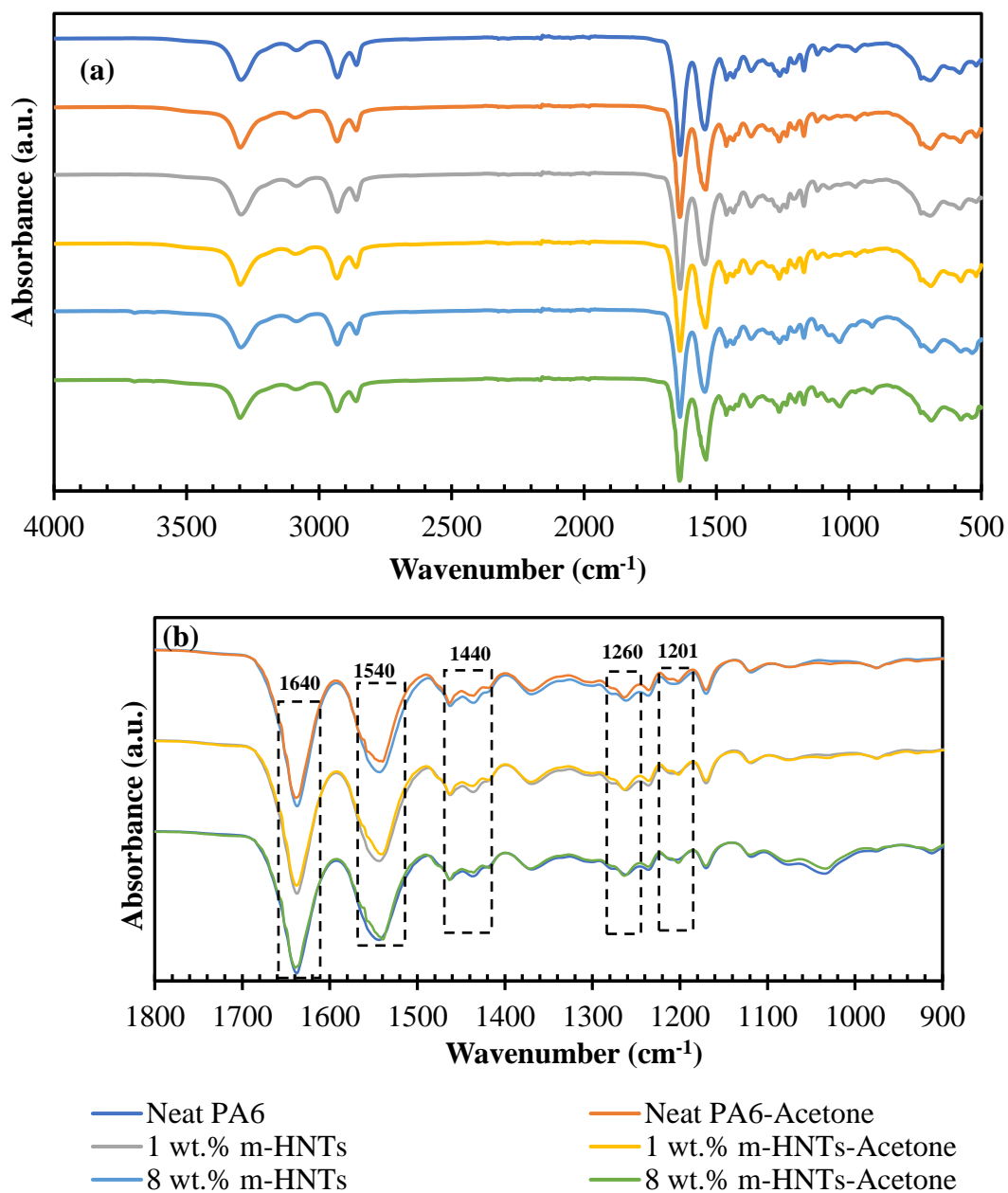
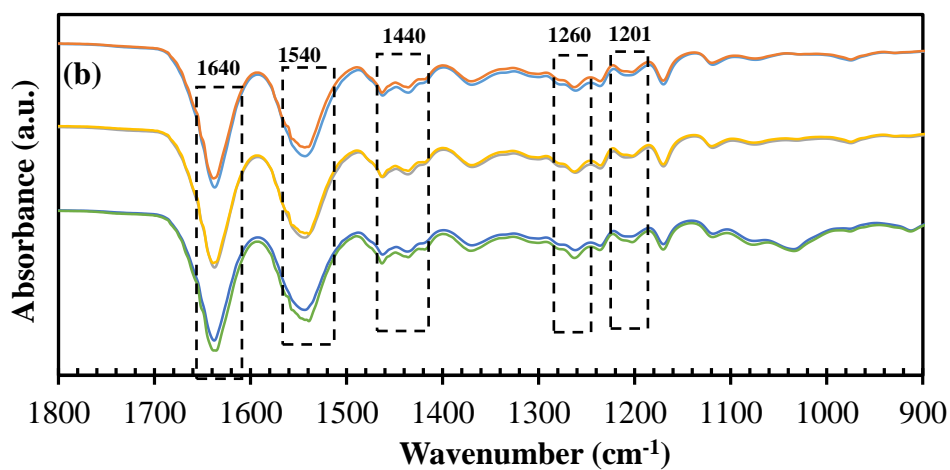
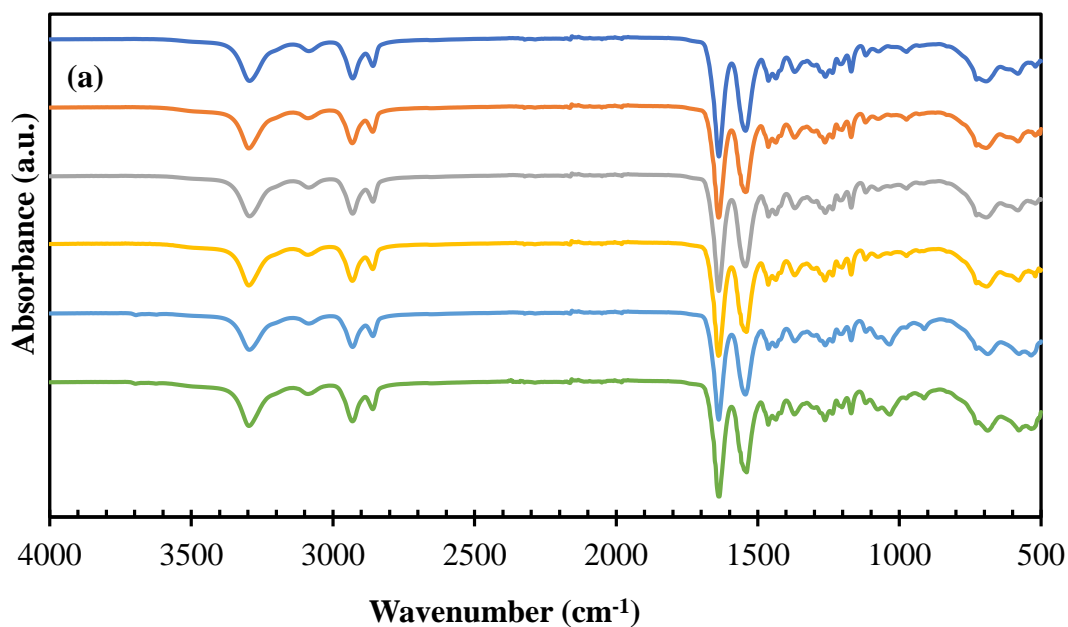


Figure 77. (a) FTIR graphs (b) zoomed FTIR graphs of the samples exposed to acetone vapor in the new setup.



- Neat PA6
- Neat PA6-Toluene
- 1 wt.% m-HNTs
- 1 wt.% m-HNTs-Toluene
- 8 wt.% m-HNTs
- 8 wt.% m-HNTs-Toluene

Figure 78. (a) FTIR graphs (b) zoomed FTIR graphs of the samples exposed to toluene vapor in the new setup.

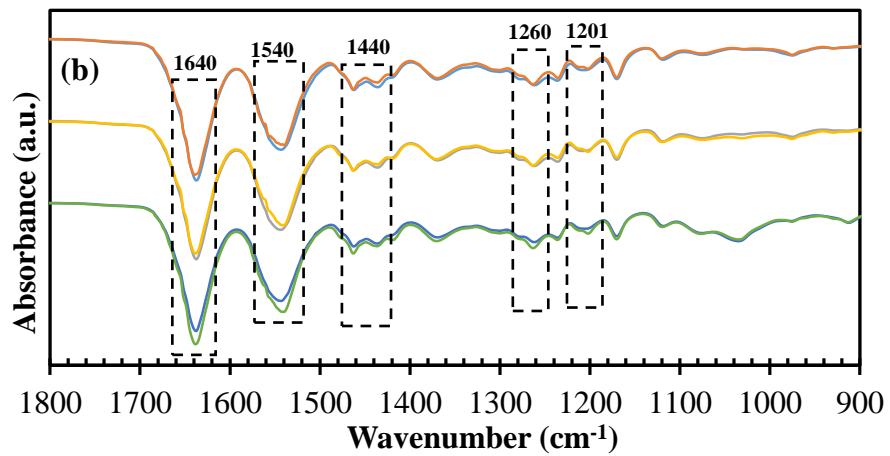
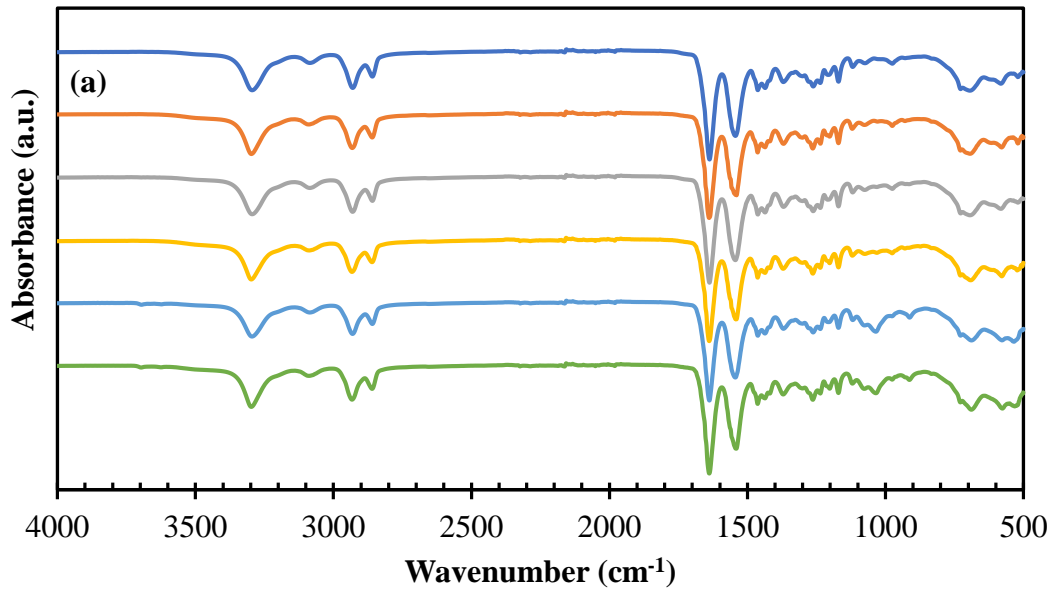


Figure 79. (a) FTIR graphs (b) zoomed FTIR graphs of the samples exposed to water vapor in the new setup.

4.3.2 Scanning Electron Microscopy (SEM) Analysis

SEM analysis was used to analyze the surface properties of neat PA6 and composite nanofibers exposed to different chemical vapors. SEM micrographs of unexposed and HCl, acetone, toluene and water vapors exposed samples in the old setup are given in Figure 80. Cumulative frequency plots of fiber diameter of the samples exposed to different chemical vapors in the old setup are given in Appendix E.

When SEM micrographs of the samples exposed to HCl vapor in the old setup (Figure 80 (d), (e) and (f)) were examined, it was seen that the morphology of the neat PA6 fibers changed significantly. Fibers were stick together with the effect of acid exposure and the structure was almost deformed. This indicates that PA6 fibers were not resistant to strong acid vapor. With the addition of HNTs, changes in the structure of the nanofibers decreased and the fiber morphology was preserved (Figure 80 (e) and (f)). As a result, it can be said that HNT increased the degradation resistance of PA6 fibers against acid vapor.

When SEM micrographs (Figure 80 (g)-(l)) of the samples exposed to acetone and toluene vapor in the old setup were examined, it was obtained that there was no significant change in the mean fiber diameter. However, some changes were observed in the structure of neat PA6 fibers. These changes were an increase in the diameter of the fiber locally and the adhesion of the fibers to each other. In addition, the semitransparent cloud structure between the fibers are seen in Figures 80 (g). On the other hand, this structure is not seen in the SEM micrographs of HNTs containing samples.

Figures 80 (m)-(o) show the SEM micrographs of the samples exposed to water vapor. In Figures 80 (m), the semitransparent cloud structure formation was detected more intensively. In addition, it is seen in Figure 80 (n) that nanofibers containing 1 wt.% m-HNTs stuck together from the specific regions of the fibers due to degradation in the water vapor environment.

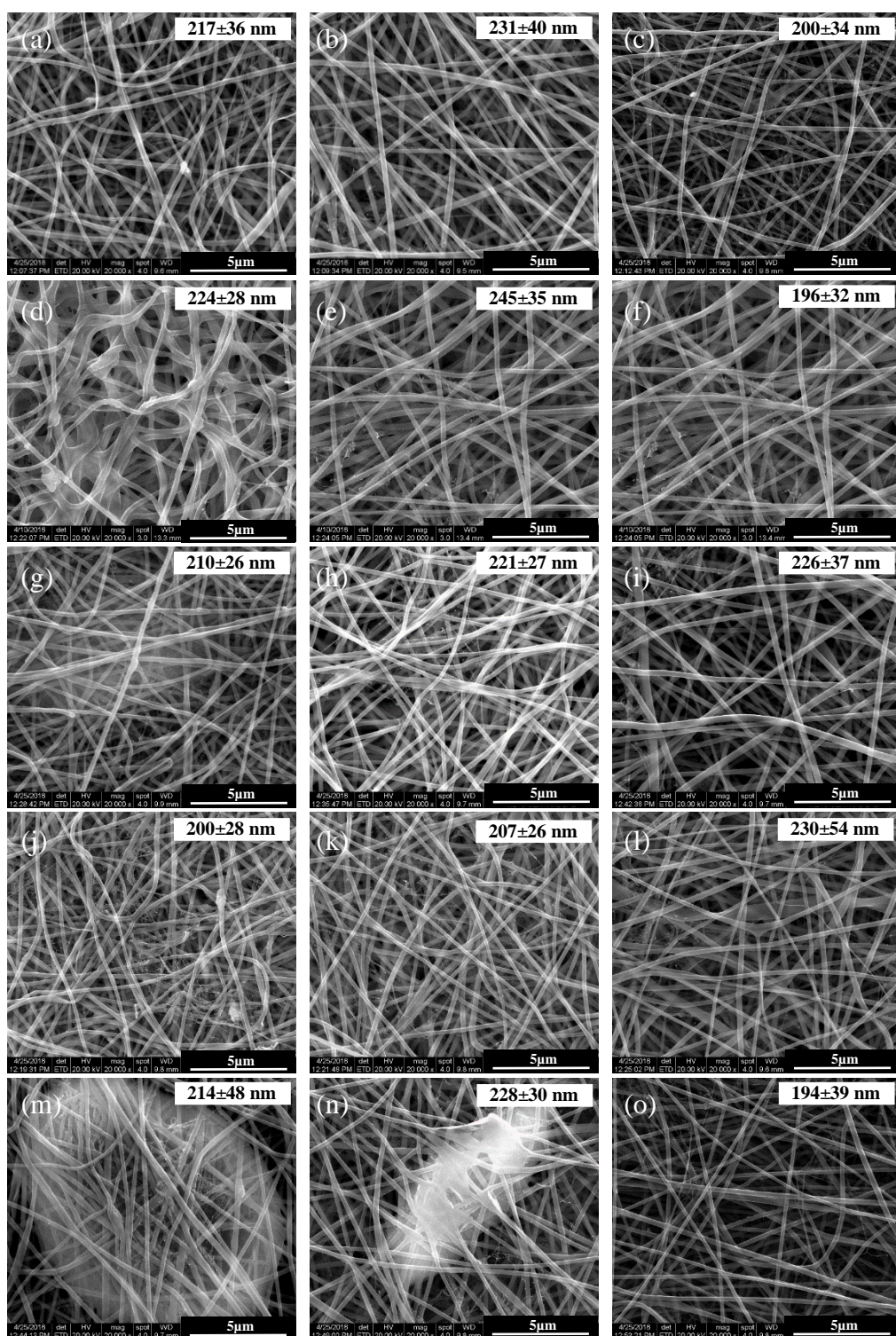


Figure 80. SEM images of **unexposed** (a) neat PA6 (b) 1 wt.% m-HNTs (c) 8 wt.% m-HNTs; **HCl exposed** (d) neat PA6 (e) 1 wt.% m-HNTs (f) 8 wt.% m-HNTs; **acetone exposed** (g) neat PA6 (h) 1 wt.% m-HNTs (i) 8 wt.% m-HNTs; **toluene exposed** (j) neat PA6 (k) 1 wt.% m-HNTs (l) 8 wt.% m-HNTs; **water exposed** (m) neat PA6 (n) 1 wt.% m-HNTs (o) 8 wt.% m-HNTs samples in the old setup.

SEM micrographs of unexposed and HCl, acetone, toluene and water vapors exposed samples in the new setup are given in Figure 81. Cumulative frequency plots of fiber diameter of the samples exposed to different chemical vapors in the new setup are given in Appendix E.

SEM micrographs of the samples exposed to HCl, acetone, toluene and water vapors in the new setup are given in Figure 81 (a)-(c). Structure of neat PA6 fibers exposed to HCl vapor was damaged and fibers stacked together in some regions. There was no significant change in the fiber morphology of 1 wt.% m-HNT containing samples and the presence of the semitransparent clouds was detected in 8 wt.% m-HNT containing samples. It was concluded that the structure of neat PA6 fibers was deformed with the effect of HCl and this was prevented by HNTs addition. When the average fiber diameters were compared by considering standard deviations, it can be said that there was not any significant change compared to the unexposed samples.

When SEM micrographs and diameter distribution results of the samples exposed to acetone vapor were examined (Figure 81 (d)-(f)), it can be said that there was no significant change in the morphology of the neat PA6 samples and fibers only were loosened by the effect of chemical vapor. In the samples containing 1 and 8 wt.% m-HNTs, the presence of semitransparent cloud shaped structures were observed, however no significant change in fiber diameters were obtained.

Morphologies of neat PA6 and the nanofibers containing 1 wt.% m-HNTs were not changed significantly after toluene vapor exposure. In the samples containing 8 wt.% m-HNTs, the formation of semitransparent cloud structures was observed. These clouds may be formed by remaining solvent in the structure due to gaps which were created by HNTs agglomerations.

SEM micrographs (Figures 81 (m)-(o)) of the samples exposed to water vapor demonstrated that PA6 fibers stuck to each other locally. In addition, the structure of the samples containing 8 wt.% m-HNT was significantly deformed and semitransparent clouds were observed due to agglomerations at high concentrations. Structural deformations were less in 1 wt.% m-HNTs containing samples, but the semitransparent clouds were still present in the structure.

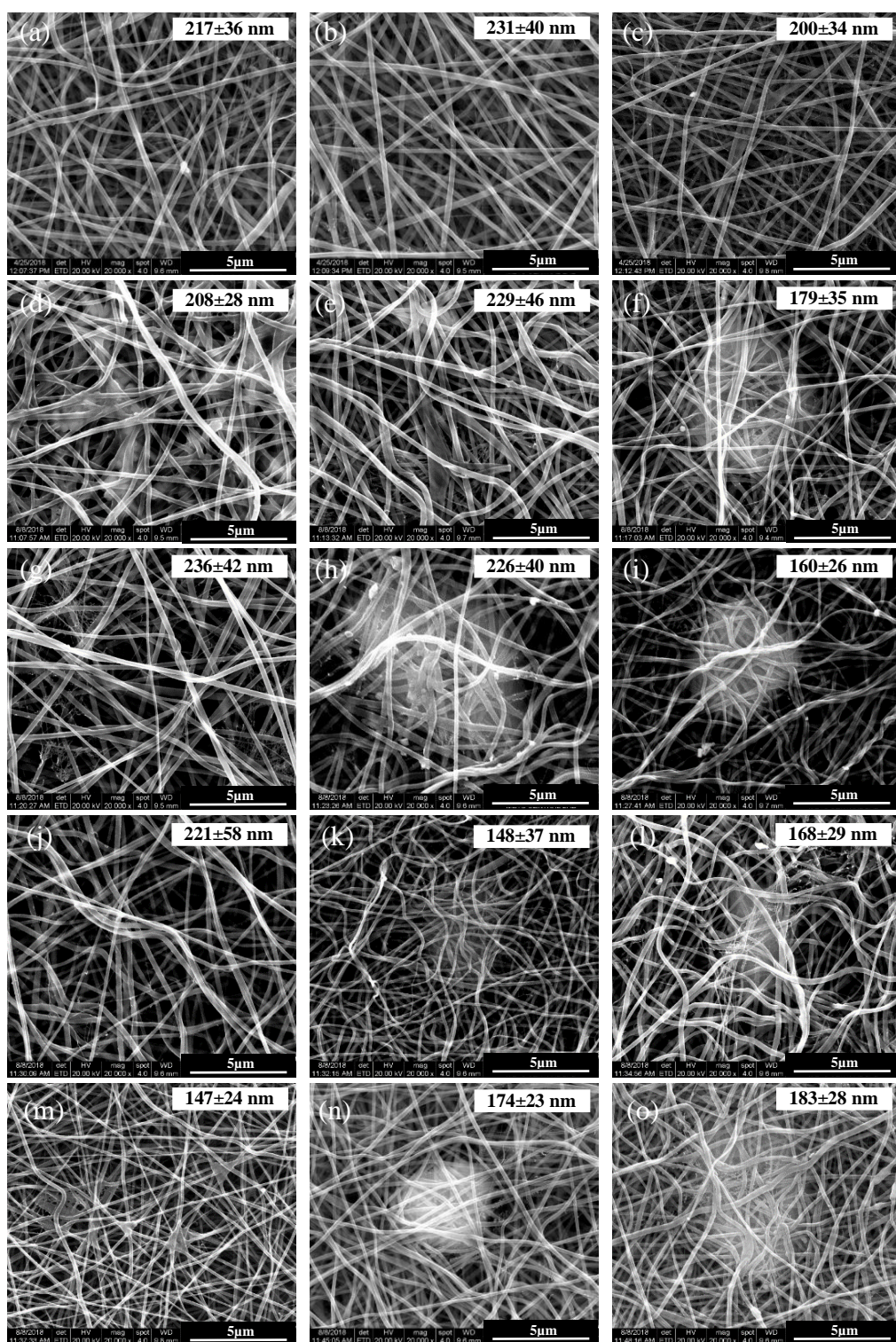


Figure 81. SEM images of **unexposed** (a) neat PA6 (b) 1 wt.% m-HNTs (c) 8 wt.% m-HNTs; **HCl exposed** (d) neat PA6 (e) 1 wt.% m-HNTs (f) 8 wt.% m-HNTs; **acetone exposed** (g) neat PA6 (h) 1 wt.% m-HNTs (i) 8 wt.% m-HNTs; **toluene exposed** (j) neat PA6 (k) 1 wt.% m-HNTs (l) 8 wt.% m-HNTs; **water exposed** (m) neat PA6 (n) 1 wt.% m-HNTs (o) 8 wt.% m-HNTs samples in the new setup.

4.3.3 Thermogravimetric Analysis

TGA analyses were performed to determine the changes in thermal stability of nanofibers after exposing them to different chemical vapors. The curves are given for the old setup in Figure 82-85. In addition, the decomposition temperatures obtained for the samples from the old setup are given in Table 13.

TGA analysis demonstrated that the decomposition temperatures of unexposed samples were around 455°C and there was no significant change with the addition of HNTs. When results of the samples exposed to chemical vapors were evaluated, HCl interaction significantly reduced the decomposition temperatures, but decrease in the decomposition temperatures was prevented to a certain extent with the addition of HNTs. After acetone vapor interaction, decomposition temperature of neat PA6 samples reduced while the results of the samples containing HNTs remained constant. When the thermal behaviors of the samples exposed to toluene vapor were evaluated, it was seen that the decomposition temperatures decreased for the all samples. Considering that toluene has less interaction with PA6 than the other chemicals due to its nonpolar structure, this decrease was more than expected. Finally, results of water vapor exposed samples showed that water vapor decreased the decomposition temperatures of the all samples. However, 1 wt.% m-HNTs containing sample gave higher result (449.38°C) than other concentrations. Well-dispersed HNTs in the polymer matrix may restrict the interaction between water and polymer, which provided higher thermal stability.

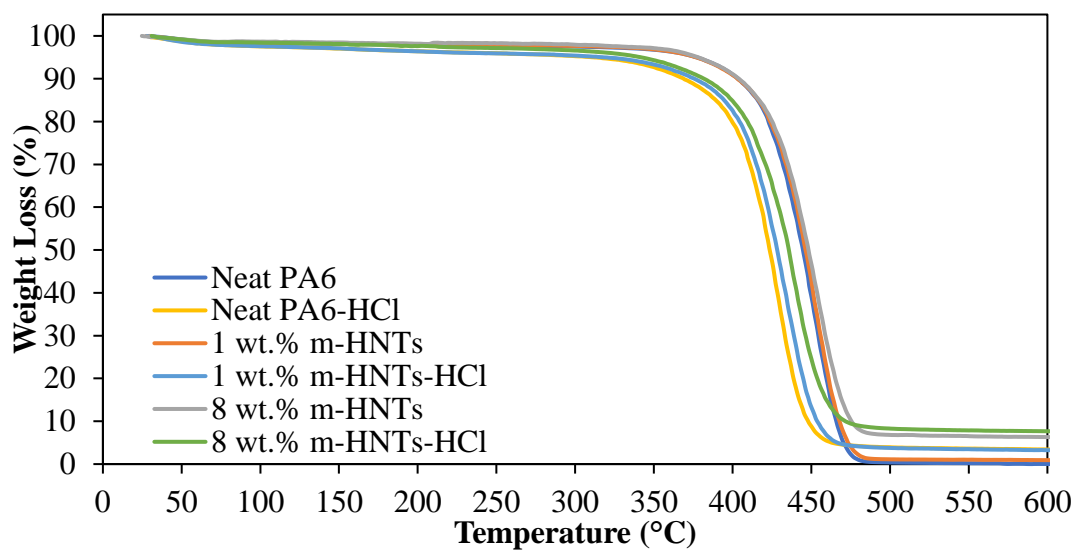


Figure 82. TGA graphs of the samples exposed to HCl vapor in the old setup.

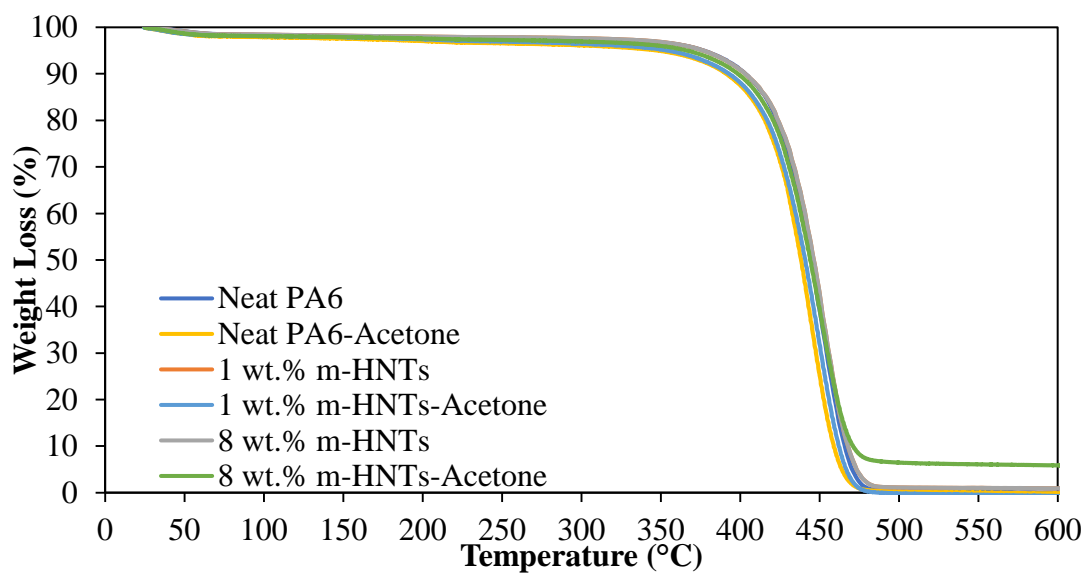


Figure 83. TGA graphs of the samples exposed to acetone vapor in the old setup.

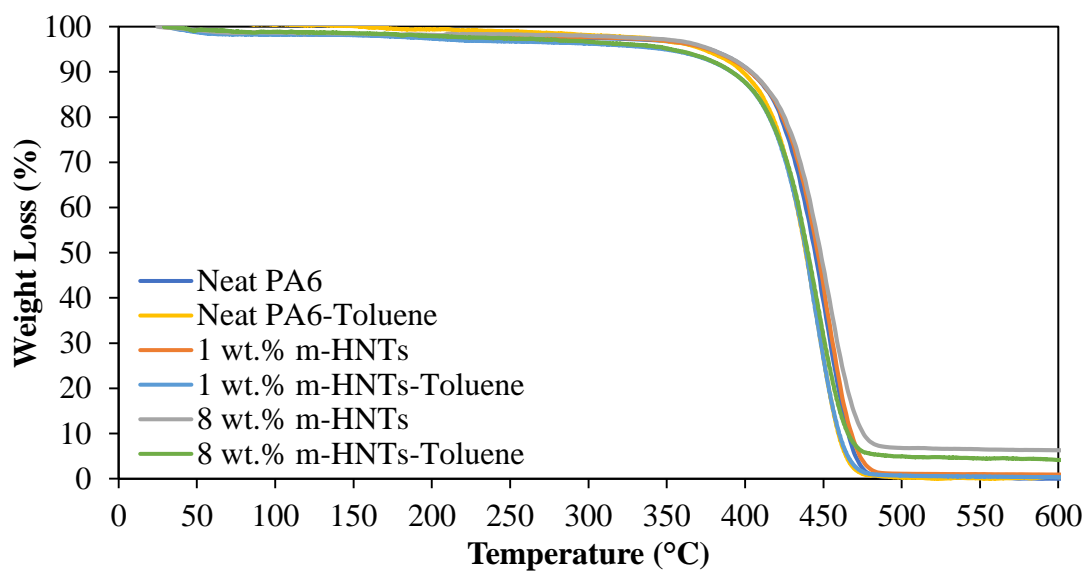


Figure 84. TGA graphs of the samples exposed to toluene vapor in the old setup.

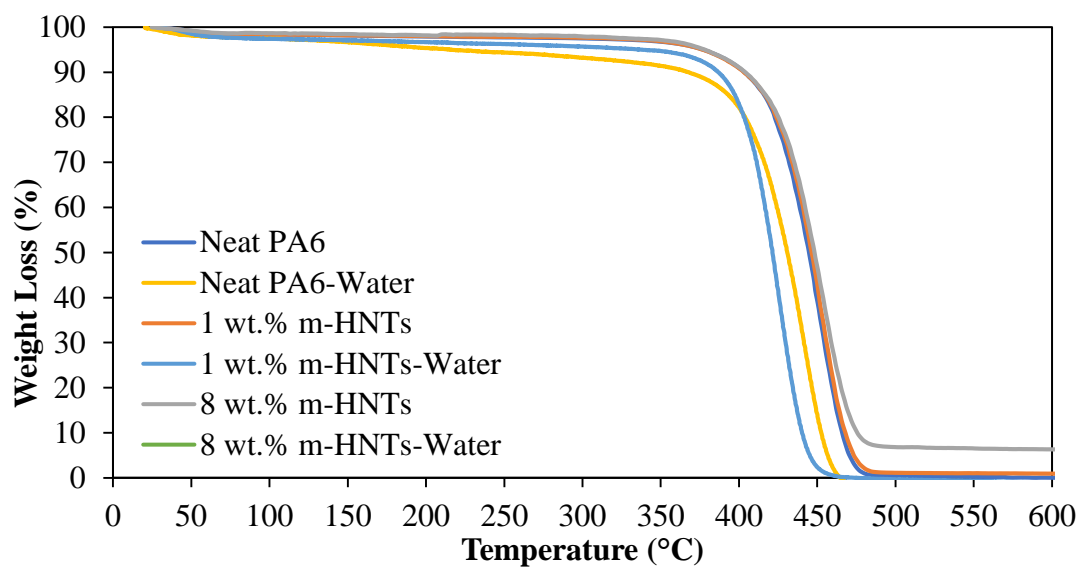


Figure 85. TGA graphs of the samples exposed to water vapor in the old setup.

Table 13. Decomposition temperatures of the samples exposed to different chemical vapors in the old setup.

	Decomposition Temperature (°C)		
	Neat PA6	1 wt.% m-HNTs	8 wt.% m-HNTs
Unexposed	453.93	455.95	455.38
HCl	429.29	431.83	436.28
Acetone	446.06	450.24	452.08
Toluene	448.71	440.70	447.75
Water	441.89	449.38	442.81

The TGA curves and decomposition temperatures of the samples tested in the new setup are given in Figures 86-89 and Table 14, respectively. When results of the samples exposed to chemical vapors were evaluated, it was seen that HCl interaction again significantly reduced the decomposition temperatures due to changes in characteristics of material after degradation. Similar results were obtained for acetone vapor exposed samples. After toluene vapor exposure, it was seen that there was no significant change in the decomposition temperatures compared to the unexposed samples. This result showed that toluene did not affect the PA6 structure after one week. The samples exposed to water vapor gave the similar results with the results of TGA analyses from the old setup and it was found that decomposition temperatures of all samples decreased after water exposure. When all the results were assessed, it can be concluded that the decomposition temperatures of samples reduced with the effect of chemical vapors and the thermal stability was preserved to a certain extent with HNTs addition.

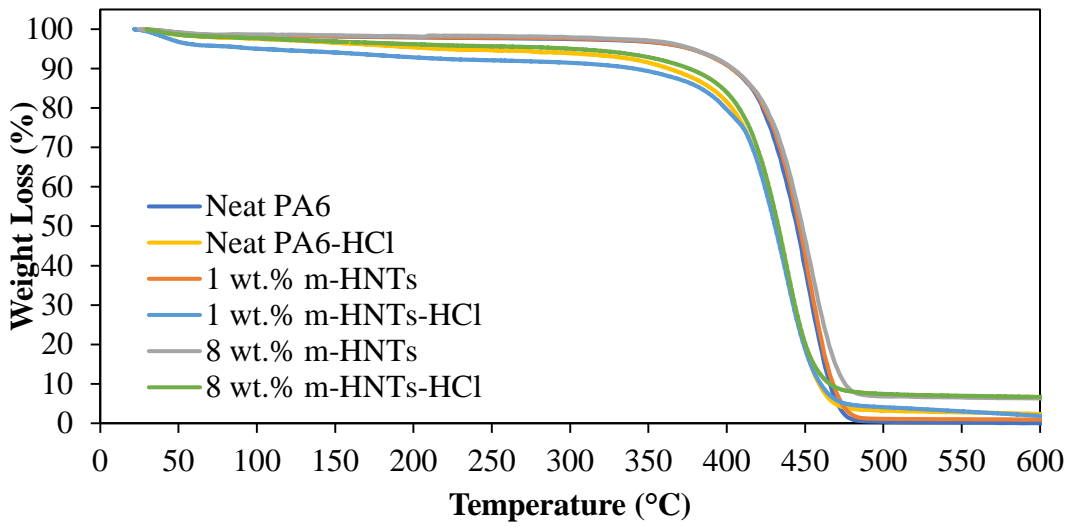


Figure 86. TGA graphs of the samples exposed to HCl vapor in the new setup.

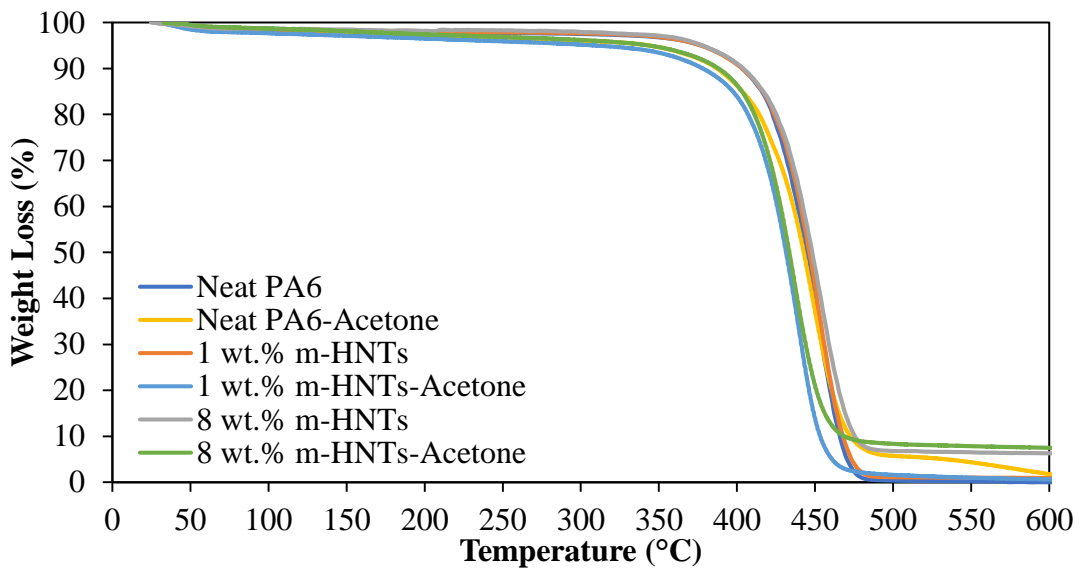


Figure 87. TGA graphs of the samples exposed to acetone vapor in the new setup.

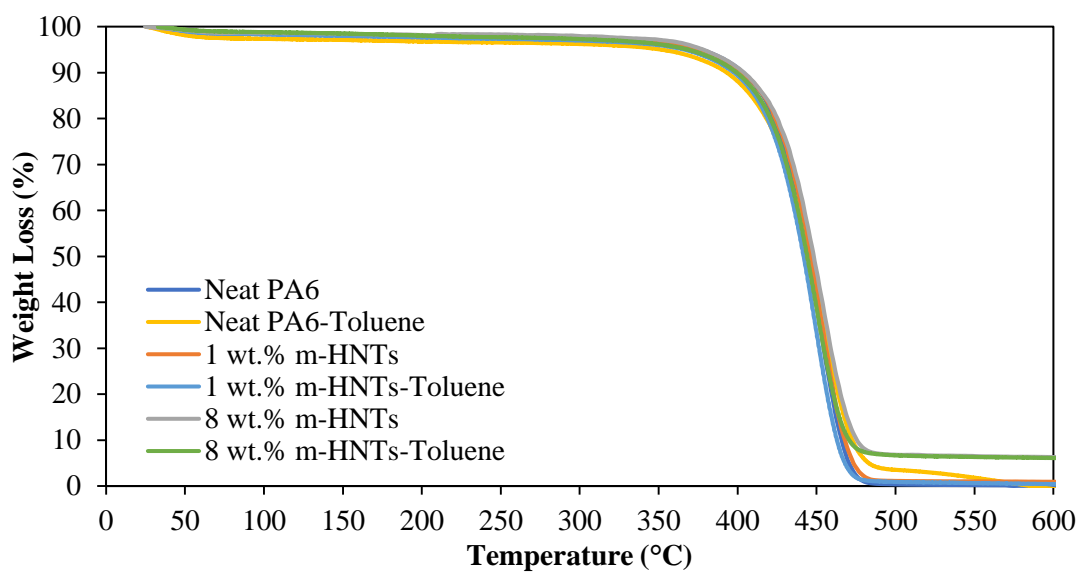


Figure 88. TGA graphs of the samples exposed to toluene vapor in the new setup.

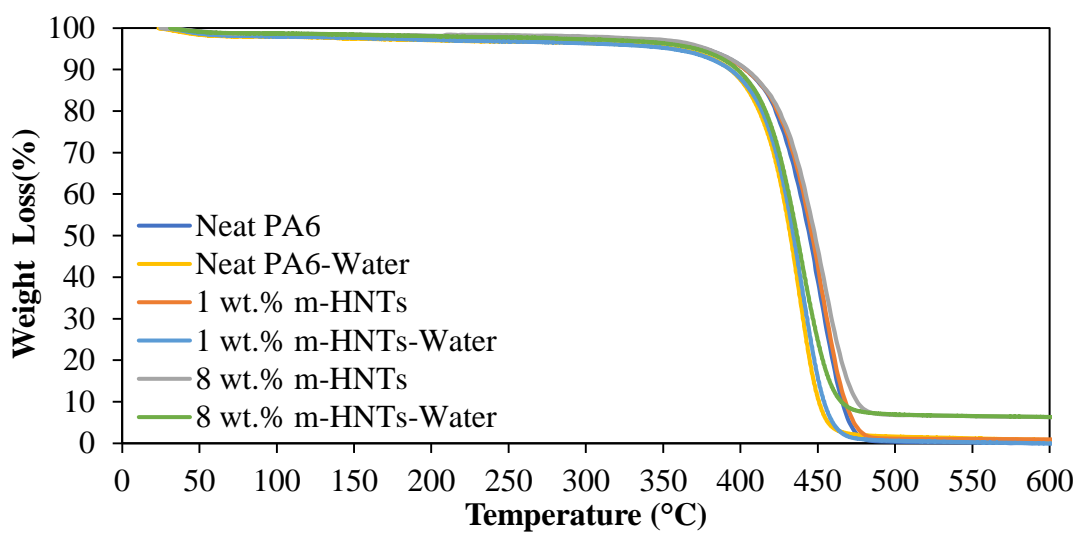


Figure 89. TGA graphs of the samples exposed to water vapor in the new setup.

Table 14. Decomposition temperatures of the samples exposed to different chemical vapors in the new setup.

	Decomposition Temperature (°C)		
	Neat PA6	1 wt.% m-HNTs	8 wt.% m-HNTs
Unexposed	453.93	455.95	455.38
HCl	434.10	438.42	438.55
Acetone	449.93	441.35	444.61
Toluene	456.29	452.40	451.60
Water	439.92	441.12	440.41

4.3.4 Differential Scanning Calorimeter

DSC analysis was performed for the electrospun mats exposed to different chemical vapors and some thermal properties such as glass transition and melting temperatures are given in Table 15 for the samples from the old setup, while the results of the samples exposed to different chemical vapors for the new setup are given in Table 16. The results showed that the glass transition temperatures reduced for the samples exposed to HCl, acetone and water vapors. The decrease in glass transition temperature after water absorption is significant for polyamides. PA6 is a hydrophilic polymer and the absorption of water is not homogeneous in the whole structure, in particular in amorphous regions. Water interaction causes the displacement of hydrogen bonds in PA6 structure resulting in lower glass transition temperature [82]. In addition, PA6 may contain a small amount of monomer (ϵ -caprolactam) and the solubility of this monomer in water is very high. After interaction with water, the water-soluble monomer can act as a plasticizer [83]. HCl and acetone solvents also contain water in large amount in the solution. The drop in glass transition temperature can be associated with the presence of this water. The glass transition temperature values for the samples exposed to non-polar toluene vapor did not change as it was expected. In addition, it was observed that the melting temperatures of the samples did not change with the chemical vapor exposure to the samples.

Table 15. DSC data of the samples exposed to different chemical vapors in the old setup.

Samples	Neat PA6		1 wt.% m-HNTs		8 wt.% m-HNTs	
	T _g (°C)	T _m (°C)	T _g (°C)	T _m (°C)	T _g (°C)	T _m (°C)
Unexposed	50.22	222.84	54.08	222.61	53.94	222.20
HCl	46.19	221.79	46.11	220.76	49.82	220.99
Acetone	44.64	222.91	45.09	223.03	45.84	223.57
Toluene	52.41	221.90	49.64	221.81	53.06	223.18
Water	42.67	224.03	46.30	223.42	50.90	222.67

Table 16. DSC data of the samples exposed to different chemical vapors in the new setup.

Samples	Neat PA6		1 wt.% m-HNTs		8 wt.% m-HNTs	
	T _g (°C)	T _m (°C)	T _g (°C)	T _m (°C)	T _g (°C)	T _m (°C)
Unexposed	50.22	222.84	54.08	222.61	53.94	222.20
HCl	48.04	219.33	45.34	221.57	43.61	220.45
Acetone	46.52	221.38	45.63	220.86	47.74	221.20
Toluene	46.23	225.31	47.32	226.77	45.79	224.30
Water	45.59	222.74	49.64	223.48	43.93	224.03

4.3.5 Tensile Test Results

The tensile test results of the samples exposed to different chemical vapors in the old setup are given in Figures 90-92 and detailed tensile test data is tabulated in Table C.5 of Appendix C. The tensile test results of the HCl vapor exposed samples had a significant decrease compared to the unexposed samples. A significant decrease in the elongation at break was observed because of deformations formed after acid interaction in some parts of the samples. Likewise, the tensile modulus results of the neat PA6 and nanofibers containing 1% m-HNTs samples decreased significantly, but the tensile modulus of 8 wt.% m-HNTs containing sample was almost the same as the unexposed samples. This shows that high HNTs concentration prevented the decrease in the tensile modulus due to its rigid structure when compared to PA6.

Tensile test results of acetone vapor exposed samples demonstrated that there was a slight decrease in the tensile strength results considering the standard deviations. However, there was a significant decrease in the elongation at break values compared to the unexposed sample. When the results of the tensile moduli of the nanofiber mats were compared, it was seen that the results decreased due to the fact that the aqueous acetone vapor penetrated the polymer structure and weakens the polymer chains.

The tensile strength and elongation at break results did not change statistically after toluene vapor exposure. However, tensile modulus of neat PA6 and 8 wt.% m-HNTs containing samples decreased compared to unexposed samples. The reason for this was that toluene vapor penetrated into the polymer structure and negatively affected the structural integrity.

Finally, results of the samples exposed to water vapor showed that the tensile strength decreased significantly for neat PA6 nanofiber mat. This reduction was inhibited with HNTs presence and 1 and 8 wt.% m-HNTs containing samples gave similar results with the unexposed samples containing. Elongation at break results indicated a significant decrease in all of the samples. Similarly, tensile modulus results showed a significant decrease in neat PA6 and 1 wt.% m-HNTs containing samples.

As mentioned in many studies in the literature, water acts as a natural plasticizer in the PA6 structure, which is a polar polymer. The plasticizers cause glass transition

temperature and the percent of crystallization to decrease and the dilution of the amorphous phase. As a result, the tensile strength and modulus of the plasticized polymer are expected to decrease, while the elongation at break is expected to increase [82,83]. When the results obtained were considered, reduction in the tensile strength and modulus values of the samples exposed to water and aqueous solvents were observed as expected. However, the elongation at break was lower than expected. This is due to the fact that the material tired after being exposed to chemical vapors for a two month and cannot show its properties due to degradation.

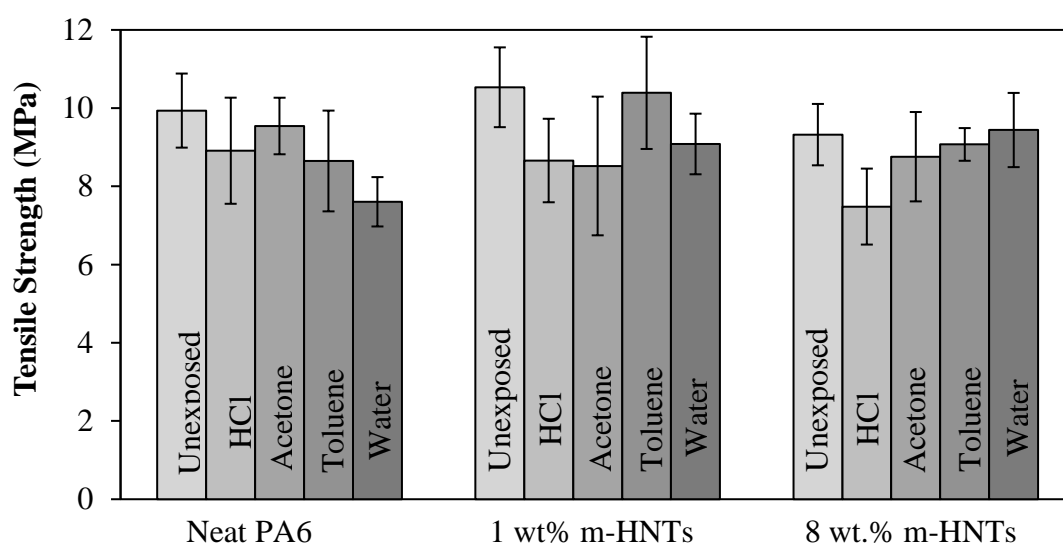


Figure 90. Tensile strengths of the samples exposed to different chemical vapors in the old setup.

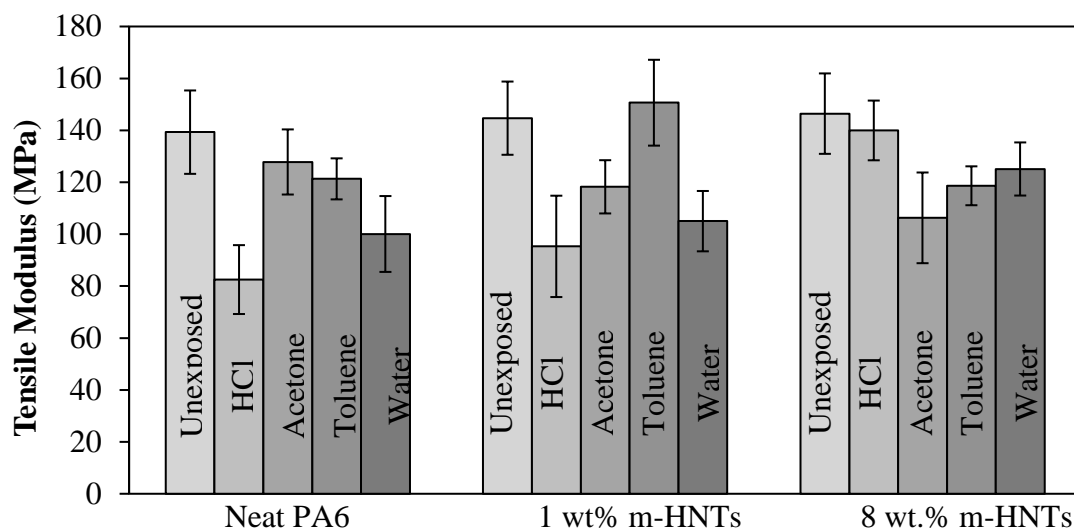


Figure 91. Tensile moduli of the samples exposed to different chemical vapors in the old setup.

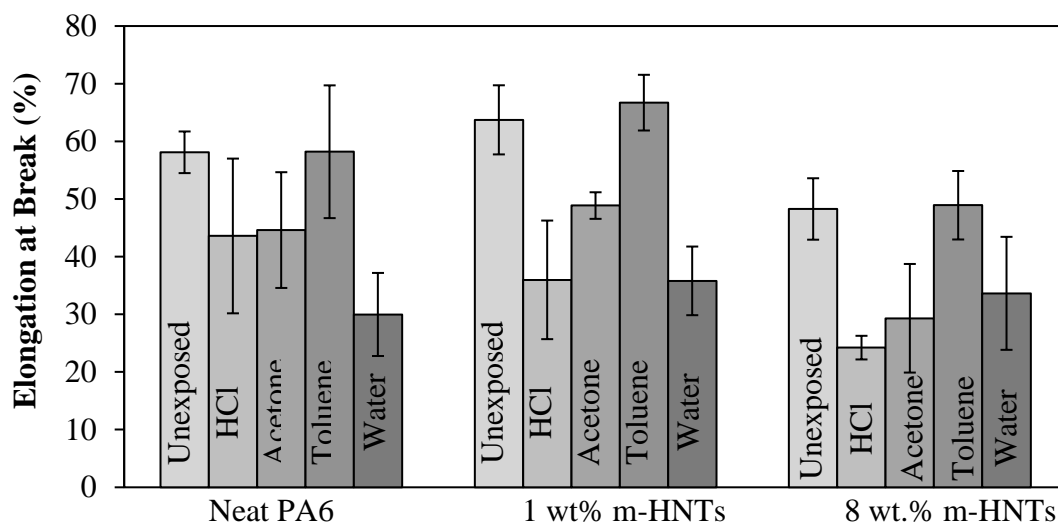


Figure 92. Elongation at break of the samples exposed to different chemical vapors in the old setup.

Tensile test results of the nanofiber mats exposed to different chemical vapors in the new setup are given in Figures 93-95 and detailed tensile test data are tabulated in Table C.6 of Appendix C. Results showed that there was a significant decrease in

tensile strength, tensile modulus and elongation at break values of the neat PA6 and 8 wt.% m-HNTs containing samples after HCl vapor exposure. On the contrary, there was not a significant change in the tensile strength and modulus results of 1 wt.% m-HNT containing samples considering the standard deviations. 1 wt.% HNTs was the optimum concentration and dispersed HNTs in the PA6 nanofibers prevented the permeation of chemical vapor by acting as a barrier in the polymer matrix.

After acetone vapor exposure, while tensile strength and elongation at break results of the neat PA6 and 8 wt.% m-HNTs containing samples decreased, results of 1 wt.% m-HNTs containing samples were almost unchanged. The tensile modulus results showed a significant decrease in all of the samples with respect to unexposed samples.

The tensile strength and elongation at break results of the samples which were exposed to toluene were almost equal to the results of the unexposed samples results. The tensile modulus of the sample containing 8 wt.% m-HNTs decreased after toluene vapor exposure. Similar results were obtained in the old setup for toluene vapor.

After water vapor interaction, the tensile strength was not significantly changed for neat PA6 and 8 wt.% m-HNTs containing samples. However, there was a decrease in tensile strength of 1 wt.% m-HNTs containing samples. When elongation at break and tensile modulus results were analyzed, a significant decrease was found in all samples. The decrease in mechanical properties could not be prevented by HNTs addition. This is explained that water acts as a plasticizer and reduces the interfacial strength between the matrix and the reinforcing material [84].

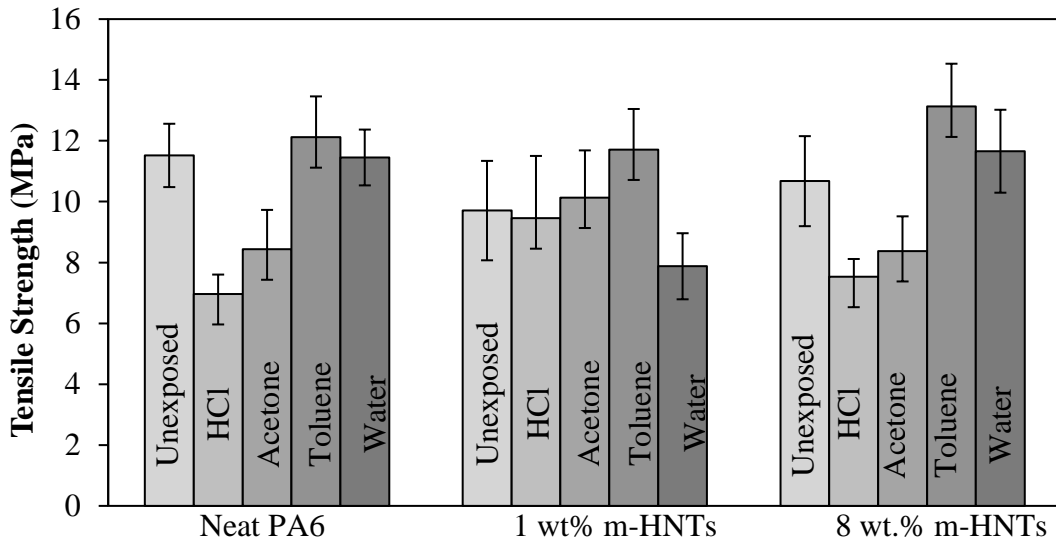


Figure 93. Tensile strengths of the samples exposed to different chemical vapors in the new setup.

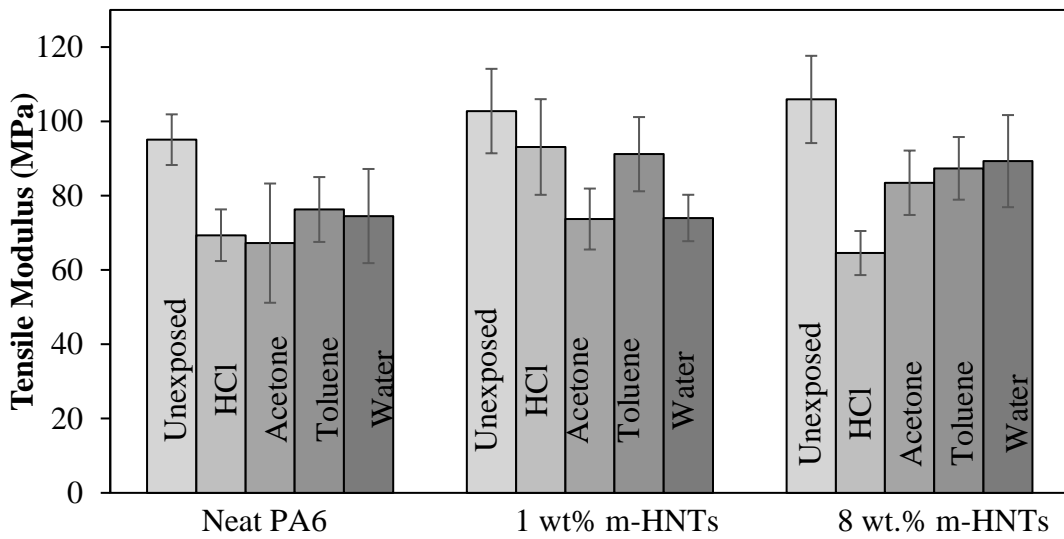


Figure 94. Tensile moduli of the samples exposed to different chemical vapors in the new setup.

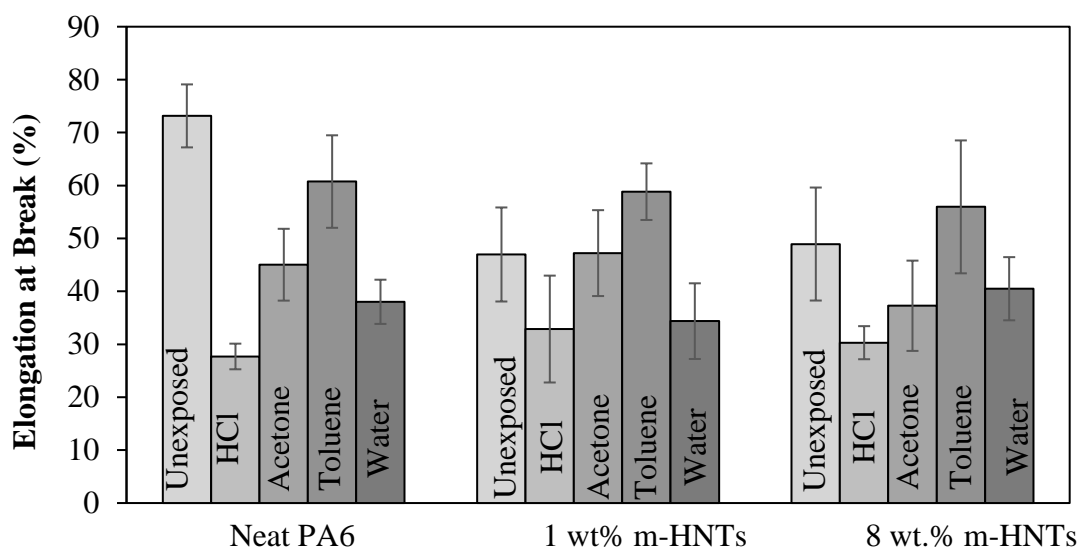


Figure 95. Elongation at break of the samples exposed to different chemical vapors in the new setup.

4.4 Limiting Oxygen Index Test

In order to determine the flame retardant properties of the composite nanofiber mats, LOI tests were conducted. The specimens with 60 mm length and 10 mm width were cut in accordance with the prepared frame (Figure 3) and the first 5 cm sections were marked. The LOI value required for the 5 cm of the samples to be fully burned was accepted as a result. When determining the sample sizes, the length and width values of the Type-I specimens in ASTM D2863-06a standard were used. Due to the fact that sample could not be produced in the required thickness for the Type-I specimen by the electrospinning method, the 180 seconds value required for the sample to burn out was not taken into consideration.

In order to minimize the effect of the thickness differences of the produced samples on the LOI, the nanofiber mats produced using the rotating cylinder were removed from the middle region where the thicknesses are most homogeneous. . In order to determine the LOI values of neat PA6, 1 and 8 wt.% m-HNTs containing samples produced by electrospinning method, 10 samples were produced and tested for each concentration. In addition to this, the LOI value of neat PA6 and 1 wt.% m-HNTs

containing samples with the same thickness as electrospun mats were produced by compression molding to investigate the effects of production method.

As a result of the LOI tests, 5 mm part of the pure PA6 fiber mat produced by electrospinning was burned at 31% O₂ value. According to this result, the LOI value for neat PA6 was accepted as 31% O₂. For the samples containing 1 wt.% m-HNTs, the LOI value was again found as 31% O₂. LOI value of the samples including 8 wt.% m-HNTs was 30% O₂. These results show that the addition of HNTs did not change the flame retardant properties of the electrospun mats. In addition, thin pure PA6 samples produced by compression molding were burned at 27% O₂ value. For molded thin films containing 1 wt.% m-HNTs, the LOI value was found as 29% O₂. PA6/1 wt.% m-HNTs composites were produced by melt mixing method provided higher LOI value than the neat PA6 from the same method that shows the effects of HNTs on the flame retardancy. This effect cannot be seen in the mats produced by the electrospinning method and that can be explained with the existence of very low amount of HNTs in the PA6 nanofibers. However, the orientation and the porous structure of the fibers produced by electrospinning may have a preventive effect during burning. SEM analyses were performed to investigate the morphology of the fibers after the LOI test and the images were given in Figure 96. When these images are examined, it is thought that the network layer formed by the adhesion of the fibers during the burning process may have a preventive effect on the flame propagation.

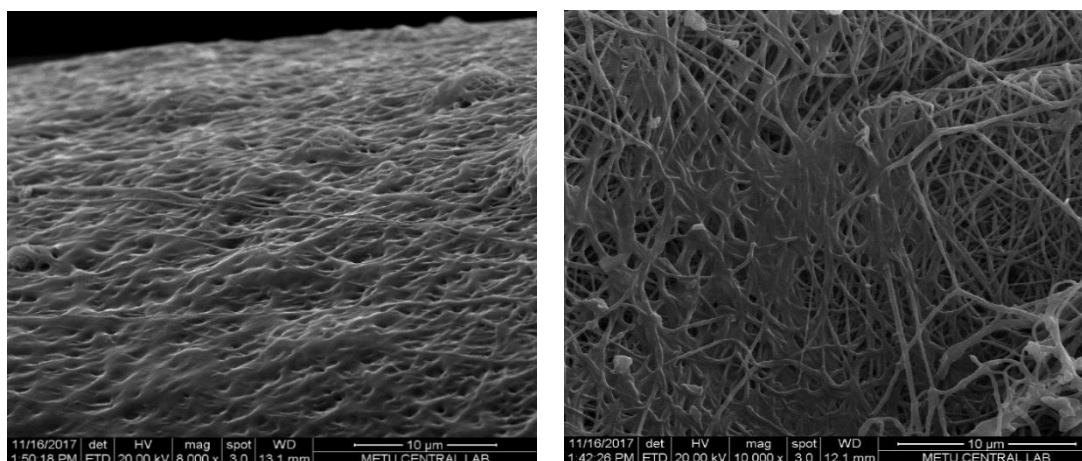


Figure 96. SEM micrographs of the neat PA6 nanofiber mat on which the LOI test applied.

CHAPTER 5

CONCLUSIONS

When all the experiments conducted within the scope of the thesis were evaluated, the following results were obtained:

1. The neat PA6 and PA6/HNTs composite nanofiber mats were successfully produced.
2. Effects of polymer solution concentration and solvent type on the fiber morphology were identified. It was found that fiber diameter increased with the polymer solution concentration. As a result, 15 wt.% PA6 solution concentration and the solvent mixture of FA and AA in 4:1 ratio was selected as suitable solution parameters.
3. Optimization of parameters such as the applied voltage and solution feed rate and tip-to-collector distance were successfully completed. The optimum conditions for electrospinning of PA6 fibers were found out as 30 kV of applied voltage, 0.33 ml/h of flowrate, and both 9 cm and 10 cm of tip-to-collector distance.
4. The surface modification of the HNTs was carried out using 1% APTES silane coupling agent. Then, 1, 2, 4, 6 and 8 wt.% of modified and unmodified HNTs containing composites were successfully prepared and characterized to assess the amount of HNTs in the matrix. It was observed that HNTs agglomerations were reduced in the composites produced with surface modified HNTs. As a result of the characterization, it was concluded that the sample containing 1 wt.% m-HNT gave better results in terms of morphology and mechanical properties.

5. The optimum parameters used in the production of the neat PA6 fibers were also successfully used in the production of the PA6/HNTs composite nanofibers.
6. Chemical vapor degradation experiments were carried out to investigate the performances of the electrospun mats. HCl (10 wt.% aqueous mixture), acetone (50 wt.% aqueous mixture), toluene and water were used as chemical vapors. As a result of the experiments carried out at different time intervals in two different setups, most of the structure of the neat PA6 and composite nanofibers changed, and their thermal and mechanical properties decreased after chemical vapor exposure. However, the samples containing 1% m-HNTs prevented some of the reductions in the properties due to the good dispersion in the PA6 matrix. At high HNTs concentrations, agglomerations were formed and HNTs did not show its superior features to prevent chemical degradation.
7. Diffusion coefficients were calculated to investigate the diffusion properties of the chemical vapors in the samples. The calculated diffusion coefficient values were in the range of 10^{-15} m²/s.
8. Comparing the resistance of the samples to chemical vapors, it was concluded that toluene vapor did not chemically alter the structure of PA6, which is a highly polar polymer.
9. LOI experiments were performed by designing a frame to characterize thin nanofiber mats and the effect of nanofiber structure on the flame retardant properties was investigated. As a result of these studies, it was found that the mats produced by electrospinning method (31% O₂) were burned at higher oxygen concentration than those produced by compression molding method (27% O₂). This result showed that the orientation and porous structure of the fibers may have a preventive effect on the flame propagation during burning.

REFERENCES

- [1] S. Ramakrishna, K. Fujihara, W.-E. Teo, T.C. Lim, Z. Ma, *An Introduction to Electrospinning and Nanofibers*, World Scientific Publishing Co. Pte.Ltd., (2005). doi:10.1142/5894.
- [2] R. Kamble, M. Ghag, S. Gaikwad, B.K. Panda, Review article halloysite nanotubes and applications : A review, *J. Adv. Sci. Res.* 3 (2012) 25–29.
- [3] P. Yuan, D. Tan, F. Annabi-Bergaya, Properties and applications of halloysite nanotubes: recent research advances and future prospects, *Appl. Clay Sci.* 112–113 (2015) 75–93. doi:10.1016/j.clay.2015.05.001.
- [4] Y.C. Ahn, S.K. Park, G.T. Kim, Y.J. Hwang, C.G. Lee, H.S. Shin, J.K. Lee, Development of high efficiency nanofilters made of nanofibers, *Curr. Appl. Phys.* 6 (2006) 1030–1035. doi:10.1016/j.cap.2005.07.013.
- [5] D. Cho, E. Zhmayev, Y.L. Joo, Structural studies of electrospun nylon 6 fibers from solution and melt, *Polymer* 52 (2011) 4600–4609. doi:10.1016/j.polymer.2011.07.038.
- [6] Y.J. Ryu, H.Y. Kim, K.H. Lee, H.C. Park, D.R. Lee, Transport properties of electrospun nylon 6 nonwoven mats, *Eur. Polym. J.* 39 (2003) 1883–1889. doi:10.1016/S0014-3057(03)00096-X.
- [7] Z.M. Huang, Y.Z. Zhang, M. Kotaki, S. Ramakrishna, A review on polymer nanofibers by electrospinning and their applications in nanocomposites, *Compos. Sci. Technol.* 63 (2003) 2223–2253. doi:10.1016/S0266-3538(03)00178-7.
- [8] S. Agarwal, M. Burgard, A. Greiner, J. Wendorff, *Electrospinning: A Practical Guide to Nanofibers*, DE GRUYTER, 2016.
- [9] J. Stanger, N. Tucker, M. Staiger, *Electrospinning*, *J. Electrostat.* 75 (1995) 218. doi:10.1111/j.1750-3841.2010.01680.x.
- [10] W-E.Teo, *Electrospin Tech, Electrospinning Parameters.* (2012).

http://electrospintech.com/collector.html#.W4V_JegzbIU.

- [11] Z. Li, C. Wang One-Dimensional Nanostructures Electrospinning Technique and Unique Nanofibers, 2016.
- [12] Z. Li, C. Wang, One-Dimensional nanostructures, 2013. doi:10.1007/978-3-642-36427-3.
- [13] A. Haider, S. Haider, I.K. Kang, A comprehensive review summarizing the effect of electrospinning parameters and potential applications of nanofibers in biomedical and biotechnology, Arab. J. Chem. (2015) doi:10.1016/j.arabjc.2015.11.015.
- [14] S. Zhang, W.S. Shim, J. Kim, Design of ultra-fine nonwovens via electrospinning of Nylon 6: Spinning parameters and filtration efficiency, Mater. Des. 30 (2009) 3659–3666. doi:10.1016/j.matdes.2009.02.017.
- [15] S. Koombhongse, W. Liu, D.H. Reneker, Flat polymer ribbons and other shapes by electrospinning, J. Polym. Sci. Part B Polym. Phys. 39 (2001) 2598–2606. doi:10.1002/polb.10015.
- [16] Q. Yang, L.I. Zhenyu, Y. Hong, Y. Zhao, S. Qiu, C.E. Wang, Y. Wei, Influence of solvents on the formation of ultrathin uniform poly(vinyl pyrrolidone) nanofibers with electrospinning, J. Polym. Sci. Part B Polym. Phys. 42 (2004) 3721–3726. doi:10.1002/polb.20222.
- [17] R.M. Nezarati, M.B. Eifert, E. Cosgriff-Hernandez, Effects of Humidity and Solution Viscosity on Electrospun Fiber Morphology, Tissue Eng. Part C Methods. 19 (2013) 810–819. doi:10.1089/ten.tec.2012.0671.
- [18] P. Heikkilä, A. Harlin, Parameter study of electrospinning of polyamide-6, Eur. Polym. J. 44 (2008) 3067–3079. doi:10.1016/j.eurpolymj.2008.06.032.
- [19] D. Fang, Y. Liu, S. Jiang, J. Nie, G. Ma, Effect of intermolecular interaction on electrospinning of sodium alginate, Carbohydr. Polym. 85 (2011) 276–279. doi:10.1016/j.carbpol.2011.01.054.
- [20] A. Koski, K. Yim, S. Shivkumar, Effect of molecular weight on fibrous PVA

- produced by electrospinning, *Mater. Lett.* 58 (2004) 493–497. doi:10.1016/S0167-577X(03)00532-9.
- [21] H.R. Pant, M.P. Bajgai, C. Yi, R. Nirmala, K.T. Nam, W. Il Baek, H.Y. Kim, Effect of successive electrospinning and the strength of hydrogen bond on the morphology of electrospun nylon-6 nanofibers, *Colloids Surfaces A Physicochem. Eng. Asp.* 370 (2010) 87–94. doi:10.1016/j.colsurfa.2010.08.051.
- [22] V. Pillay, C. Dott, Y.E. Choonara, C. Tyagi, L. Tomar, P. Kumar, L.C. Du Toit, V.M.K. Ndesendo, A review of the effect of processing variables on the fabrication of electrospun nanofibers for drug delivery applications, *J. Nanomater.* 2013 (2013). doi:10.1155/2013/789289.
- [23] X. Zong, K. Kim, D. Fang, S. Ran, B.S. Hsiao, B. Chu, Structure and process relationship of electrospun bioabsorbable nanofiber membranes, *Polymer (Guildf)*. 43 (2002) 4403–4412. doi:10.1016/S0032-3861(02)00275-6.
- [24] T. Mazoochi, M. Hamadani, M. Ahmadi, V. Jabbari, Investigation on the morphological characteristics of nanofibrous membrane as electrospun in the different processing parameters, *Int. J. Ind. Chem.* 3 (2012) 1–8. doi:10.1186/2228-5547-3-2.
- [25] W-E. Teo, *ElectrospinTech, Voltage.* (2012). <http://electrospintech.com/voltage.html#.W6EO7OgzY-c>.
- [26] C.J. Uchko, L.C. Chen, Y. Shen, D.C. Martina, Processing and microstructural characterization of porous biocompatible protein polymer thin films, *Polymer (Guildf)*. 40 (1999) 7397–7407. doi:10.1016/S0032-3861(98)00866-0.
- [27] J. Deitzel, J. Kleinmeyer, D. Harris, N. Beck Tan, The effect of processing variables on the morphology of electrospun nanofibers and textiles, *Polymer (Guildf)*. 42 (2001) 261–272. doi:10.1016/S0032-3861(00)00250-0.
- [28] O.S. Yördem, M. Papila, Y.Z. Menceloğlu, Effects of electrospinning parameters on polyacrylonitrile nanofiber diameter: An investigation by response surface methodology, *Mater. Des.* 29 (2008) 34–44.

doi:10.1016/j.matdes.2006.12.013.

- [29] D. Fallahi, M. Rafizadeh, N. Mohammadi, B. Vahidi, Effect of applied voltage on jet electric current and flow rate in electrospinning of polyacrylonitrile solutions, *Polym. Int.* 57 (2008) 1363–1368. doi:10.1002/pi.2482.
- [30] C. Wang, W. Zhang, Z.H. Huang, E.Y. Yan, Y.H. Su, Effect of concentration, voltage, take-over distance and diameter of pinhead on precursory poly (phenylene vinylene) electrospinning, *Pigment Resin Technol.* 35 (2006) 278–283. doi:10.1108/03699420610692887.
- [31] A.H. Hekmati, A. Rashidi, R. Ghazisaeidi, J.Y. Drean, Effect of needle length, electrospinning distance, and solution concentration on morphological properties of polyamide-6 electrospun nanowebs, *Text. Res. J.* 83 (2013) 1452–1466. doi:10.1177/0040517512471746.
- [32] N. Amiraliyan, M. Nouri, M.H. Kish, Effects of some electrospinning parameters on morphology of natural silk-based nanofibers, *J. Appl. Polym. Sci.* 113 (2009) 226–234. doi:10.1002/app.29808.
- [33] F.L. Huang, Q.F. Wei, J.X. Wang, Y.B. Cai, Y.B. Huang, Effect of temperature on structure, morphology and crystallinity of PVDF nanofibers via electrospinning, *E-Polymers.* 152 (2008) 1–8. doi:152.
- [34] B. De Schoenmaker, L. Van Der Schueren, R. Zuggle, A. Goethals, P. Westbroek, P. Kiekens, T. Nyokong, K. De Clerck, Effect of the relative humidity on the fibre morphology of polyamide 4.6 and polyamide 6.9 nanofibres, *J. Mater. Sci.* 48 (2013) 1746–1754. doi:10.1007/s10853-012-6934-9.
- [35] R. Sahay, P.S. Kumar, R. Sridhar, J. Sundaramurthy, J. Venugopal, S.G. Mhaisalkar, S. Ramakrishna, Electrospun composite nanofibers and their multifaceted applications, *J. Mater. Chem.* 22 (2012) 12953–12971. doi:10.1039/c2jm30966a.
- [36] L. Li, L.M. Bellan, H.G. Craighead, M.W. Frey, Formation and properties of nylon-6 and nylon-6/montmorillonite composite nanofibers, *Polymer* 47 (2006)

6208–6217. doi:10.1016/j.polymer.2006.06.049.

- [37] M. V. Jose, B.W. Steinert, V. Thomas, D.R. Dean, M.A. Abdalla, G. Price, G.M. Janowski, Morphology and mechanical properties of Nylon 6/MWNT nanofibers, *Polymer*. 48 (2007) 1096–1104.
doi:10.1016/j.polymer.2006.12.023.
- [38] D. Tao, Y. Higaki, W. Ma, H. Wu, T. Shinohara, T. Yano, A. Takahara, Chain orientation in poly(glycolic acid)/halloysite nanotube hybrid electrospun fibers, *Polym. (United Kingdom)*. 60 (2015) 284–291.
doi:10.1016/j.polymer.2015.01.048.
- [39] C. Zhilin, Q. Xixi, Q. Dunzhong, Electrospinning Preparation and Mechanical Properties of Polymethyl Methacrylate (PMMA)/Halloysite Nanotubes (HNTs) Composite Nanofibers, 18 (2016) 52–56.
- [40] N. Cai, Q. Dai, Z. Wang, X. Luo, Y. Xue, F. Yu, Toughening of electrospun poly(l-lactic acid) nanofiber scaffolds with unidirectionally aligned halloysite nanotubes, *J. Mater. Sci.* 50 (2015) 1435–1445. doi:10.1007/s10853-014-8703-4.
- [41] J. Wang, V. Planz, B. Vukosavljevic, M. Windbergs, Multifunctional electrospun nanofibers for wound application – Novel insights into the control of drug release and antimicrobial activity, *Eur. J. Pharm. Biopharm.* 129 (2018) 175–183. doi:10.1016/j.ejpb.2018.05.035.
- [42] S. Moon, J. Lee, Electrospun poly(ethylene oxide)/hydrated iron oxide/sodium alginate composite nanofibers with multi-functional properties, *Polym. Eng. Sci.* 53 (2013) 1321–1326. doi:10.1002/pen.23431.
- [43] M. Karimi, *Diffusion in Polymer Solids and Solutions*, *Mass Transf. Chem. Eng. Process.* (2011). doi:10.5772/23436.
- [44] N. Abacha, M. Kubouchi, T. Sakai, Diffusion behavior of water in polyamide 6 organoclay nanocomposites, *Express Polym. Lett.* 3 (2009) 245–255. doi:10.3144/expresspolymlett.2009.31.

- [45] J. Boulton, D.L. Jackson, The Fluidity of Nylon Solutions in m-Cresol: Measurement of Chemical Damage in Nylon Textiles, *J. Soc. Dye. Colour.* 59 (1943) 21–26.
- [46] J.S. Shelley, P.T. Mather, K.L. DeVries, Reinforcement and environmental degradation of nylon-6/clay nanocomposites, *Polymer.* 42 (2001) 5849–5858. doi:10.1016/S0032-3861(00)00900-9.
- [47] Abastari, T. Sakai, H. Sembokuya, M. Kubouchi, K. Tsuda, Study on permeation behavior and chemical degradation of PA66 in acid solution, *Polym. Degrad. Stab.* 92 (2007) 379–388. doi:10.1016/j.polymdegradstab.2006.12.002.
- [48] M. Makaremi, R.T. De Silva, P. Pasbakhsh, Electrospun nanofibrous membranes of polyacrylonitrile/halloysite with superior water filtration ability, *J. Phys. Chem. C.* 119 (2015) 7949–7958. doi:10.1021/acs.jpcc.5b00662.
- [49] M. Ghanbari, D. Emadzadeh, W.J. Lau, H. Riazi, D. Almasi, A.F. Ismail, Minimizing structural parameter of thin film composite forward osmosis membranes using polysulfone/halloysite nanotubes as membrane substrates, *Desalination.* 377 (2016) 152–162. doi:10.1016/j.desal.2015.09.019.
- [50] E.S. Gonçalves, L. Poulsen, P.R. Ogilby, Mechanism of the temperature-dependent degradation of polyamide 66 films exposed to water, *Polym. Degrad. Stab.* 92 (2007) 1977–1985. doi:10.1016/j.polymdegradstab.2007.08.007.
- [51] J. Crank, *The mathematics of diffusion*, Oxford University Press, Ely House, London W.I, (1975). doi:10.1016/0306-4549(77)90072-X.
- [52] D.P.N. Vlasveld, J. Groenewold, H.E.N. Bersee, S.J. Picken, Moisture absorption in polyamide-6 silicate nanocomposites and its influence on the mechanical properties, *Polymer.* 46 (2005) 12567–12576 doi:10.1016/j.polymer.2005.10.096.
- [53] F.M. Preda, A. Alegría, A. Bocahut, L.A. Fillot, D.R. Long, P. Sotta, Investigation of Water Diffusion Mechanisms in Relation to Polymer Relaxations in Polyamides, *Macromolecules.* 48 (2015) 5730–5741. doi:10.1021/acs.macromol.5b01295.

- [54] Tecomid NB40 NL E Technical Data Sheet, (2012). http://www.eurotec-ep.com/s/1404/i/TDS_Tecomid_NB40_NL_E.pdf.
- [55] Halloysite Nanotubes Properties, (n.d.). <https://www.sigmaaldrich.com/catalog/product/aldrich/685445?lang=en®ion=TR>.
- [56] D. Budak, G. Bayram, Che-499 Report, Topics in Chemical Engineering-Surface Modification of Halloysite Nanotubes and Their Characterization, (2017).
- [57] Ne 300 Technical Information, (n.d.). <http://www.inovenso.com/ne300.pdf>.
- [58] Q. Li, D. Gao, Q. Wei, M. Ge, W. Liu, L. Wang, K. Hu, Thermal stability and crystalline of electrospun polyamide 6/organo-montmorillonite nanofibers, *J. Appl. Polym. Sci.* 21 (2010) NA-NA. doi:10.1002/app.32017.
- [59] S. De Vrieze, B. De Schoenmaker, Ö. Ceylan, J. Depuydt, L. Van Landuyt, H. Rahier, G. Van Assche, K. De Clerck, Morphologic study of steady state electrospun polyamide 6 nanofibres, *J. Appl. Polym. Sci.* 119 (2011) 2984–2990. doi:10.1002/app.33036.
- [60] D.H. Reneker, A.L. Yarin, Electrospinning jets and polymer nanofibers, *Polymer.* 49 (2008) 2387–2425. doi:10.1016/j.polymer.2008.02.002.
- [61] A. Stanishevsky, J. Wetuski, M. Walock, I. Stanishevskaya, H. Yockell-Lelièvre, E. Kořáková, D. Lukáš, Ribbon-like and spontaneously folded structures of tungsten oxide nanofibers fabricated via electrospinning, *RSC Adv.* 5 (2015) 69534–69542. doi:10.1039/c5ra11884k.
- [62] R. Nirmala, H.R. Panth, C. Yi, K.T. Nam, S.J. Park, H.Y. Kim, R. Navamathavan, Effect of solvents on high aspect ratio polyamide-6 nanofibers via electrospinning, *Macromol. Res.* 18 (2010) 759–765. doi:10.1007/s13233-010-0808-2.
- [63] S. Huan, G. Liu, G. Han, W. Cheng, Z. Fu, Q. Wu, Q. Wang, Effect of experimental parameters on morphological, mechanical and hydrophobic

- properties of electrospun polystyrene fibers, *Materials (Basel)*. 8 (2015) 2718–2734. doi:10.3390/ma8052718.
- [64] O. Ero-Phillips, M. Jenkins, A. Stamboulis, Tailoring Crystallinity of Electrospun Plla Fibres by Control of Electrospinning Parameters, *Polymers (Basel)*. 4 (2012) 1331–1348. doi:10.3390/polym4031331.
- [65] E.P.S. Tan, S.Y. Ng, C.T. Lim, Tensile testing of a single ultrafine polymeric fiber, *Biomaterials*. 26 (2005) 1453–1456. doi:10.1016/j.biomaterials.2004.05.021.
- [66] V. Milleret, B. Simona, P. Neuenschwander, H. Hall, Tuning electrospinning parameters for production of 3D-fiber-fleeces with increased porosity for soft tissue engineering applications, *Eur. Cells Mater*. 21 (2011) 286–303. doi:10.22203/eCM.v021a22.
- [67] H. Jiyong, Z. Yinda, Z. Hele, G. Yuanyuan, Y. Xudong, Mixed effect of main electrospinning parameters on the β -phase crystallinity of electrospun PVDF nanofibers, *Smart Mater. Struct*. 26 (2017). doi:10.1088/1361-665X/aa7245
- [68] S. Saehana, F. Iskandar, M. Abdullah, Optimization of Electrospinning Parameter by Employing Genetic Algorithm in Order to Produce Desired Nanofiber Diameter, *Int. J. Chem. Nucl. Metall. Mater. Eng*. 7 (2013) 78–83.
- [69] L. Li, Z. Wu, S. Jiang, S. Zhang, S. Lu, W. Chen, B. Sun, M. Zhu, Effect of halloysite nanotubes on thermal and flame retardant properties of polyamide 6/melamine cyanurate composites, *Polym. Compos*. 36 (2015) 892–896. doi:10.1002/pc.23008.
- [70] K. Szpilska, K. Czaja, S. Kudla, Thermal stability and flammability of polyolefin / halloysite nanotubes composites, *Polimery*. 12 (2015) 673–679. doi:10.14314/polimery.2015.673.
- [71] M. Liu, B. Guo, M. Du, D. Jia, Drying induced aggregation of halloysite nanotubes in polyvinyl alcohol/halloysite nanotubes solution and its effect on properties of composite film, *Appl. Phys. A Mater. Sci. Process*. 88 (2007) 391–395. doi:10.1007/s00339-007-3995-8.

- [72] H. Alamri, I.M. Low, Effect of halloysite nanotubes on water absorption and mechanical characteristics of cellulose fibre reinforced epoxy composites in wet conditions, (2012) 6–8. doi:10.13140/RG.2.1.2811.8881.
- [73] A.R. de Anda, Influence of the solvent sorption, additivation , and chemical modification on the molecular mobility dynamics of Polyamide 6,6 amorphous phase and its consequences on the tensile and impact strength properties of this polymer Agustin Rios de Anda To c, (2014).
- [74] B.H. Choi, Z. Zhou, A. Chudnovsky, S.S. Stivala, K. Sehanobish, C.P. Bosnyak, Fracture initiation associated with chemical degradation: Observation and modeling, *Int. J. Solids Struct.* 42 (2005) 681–695. doi:10.1016/j.ijsolstr.2004.06.028.
- [75] K. Wudy, D. Drummer, F. Kühnlein, M. Drexler, Influence of degradation behavior of polyamide 12 powders in laser sintering process on produced parts, *AIP Conf. Proc.* 1593 (2014) 691–695. doi:10.1063/1.4873873.
- [76] V. Bugatti, G. Viscusi, C. Naddeo, G. Gorrasi, Nanocomposites Based on PCL and Halloysite Nanotubes Filled with Lysozyme: Effect of Draw Ratio on the Physical Properties and Release Analysis, *Nanomaterials.* 7 (2017) 213. doi:10.3390/nano7080213.
- [77] S. Padhi, P.G.R. Achary, N.C. Nayak, Molecular transport behaviour of organic solvents through halloysite nanotubes filled ethylene – vinyl acetate copolymer, 38 (2015) 925–933.
- [78] P. Yuan, D. Tan, F. Annabi-Bergaya, Properties and applications of halloysite nanotubes: Recent research advances and future prospects, *Appl. Clay Sci.* 112–113 (2015) 75–93. doi:10.1016/j.clay.2015.05.001.
- [79] G. Bayram, S. Şahin, D. Budak, R.B. Yılmaz, B. Erkmen, Elektro-eğirme Yöntemi Kullanılarak Üretilen Naylon-6/Halloysit Nanotüp Nano-fiberlerinin Çoklu Fonksiyonel Özelliklerinin Geliştirilmesi, Tübitak Final Report, (2018).
- [80] F. Navarro-Pardo, G. Martínez-Barrera, A.L. Martínez-Hernández, V.M. Castaño, J.L. Rivera-Armenta, F. Medellín-Rodríguez, C. Velasco-Santos,

- Effects on the thermo-mechanical and crystallinity properties of nylon 6,6 electrospun fibres reinforced with one dimensional (1D) and two dimensional (2D) carbon, *Materials (Basel)*. 6 (2013) 3494–3513. doi:10.3390/ma6083494.
- [81] N. Mahmood, M. Islam, A. Hameed, S. Saeed, A.N. Khan, Polyamide-6-based composites reinforced with pristine or functionalized multi-walled carbon nanotubes produced using melt extrusion technique, *J. Compos. Mater.* 48 (2014) 1197–1207. doi:10.1177/0021998313484779.
- [82] H.K. Reimschuessel, A. Chemical, Relationships on the effect of water on glass transition temperature and young's modulus of nylon 6, *J. Polym. Sci. Polym. Chemisrty Ed.* 16 (1978) 1229–1236. doi:10.1002/pol.1978.170160606.
- [83] C. Pai, R. Jeng, Effects of moisture on thermal and mechanical properties of nylon 6,6, *Adv. Polym.* 9 (1989) 157–163. doi:10.1002/adv.1989.060090206.
- [84] M.S. Saharudin, R. Atif, I. Shyha, F. Inam, The degradation of mechanical properties in polymer nano-composites exposed to liquid media -A review, *RSC Adv.* 6 (2016) 1076–1089. doi:10.1039/c5ra22620a.

APPENDICES

APPENDIX A

FTIR SPECTRA FOR UNMODIFIED AND APTES MODIFIED HNTs

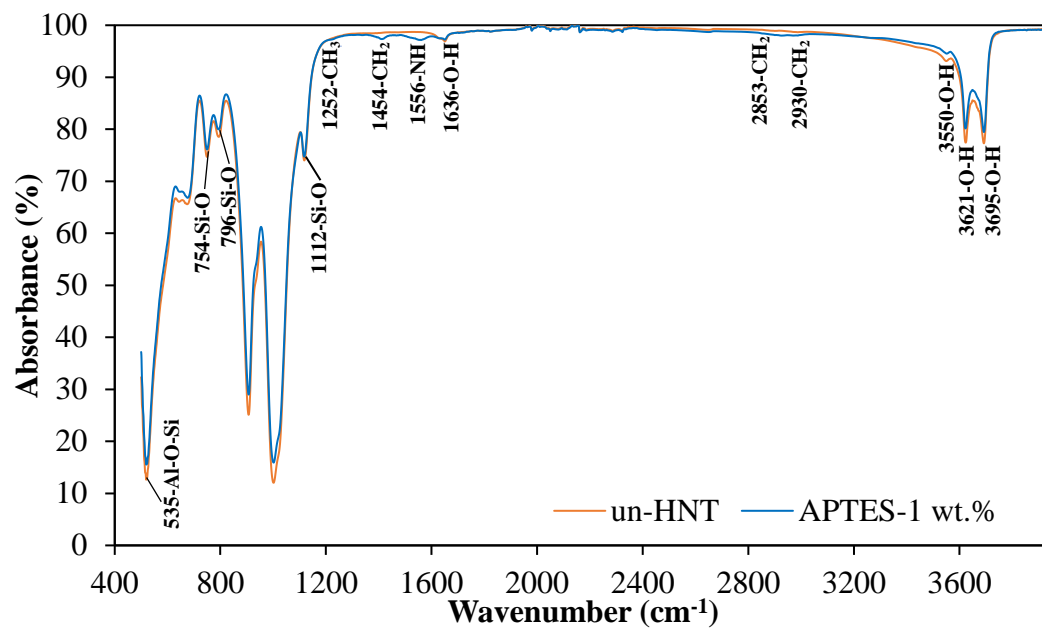


Figure A.1. FTIR Spectra of unmodified and 1 wt.% APTES modified HNTs.

APPENDIX B

DSC CURVES OF THE NANOFIBER PRODUCED USING DIFFERENT PROCESS PARAMETERS

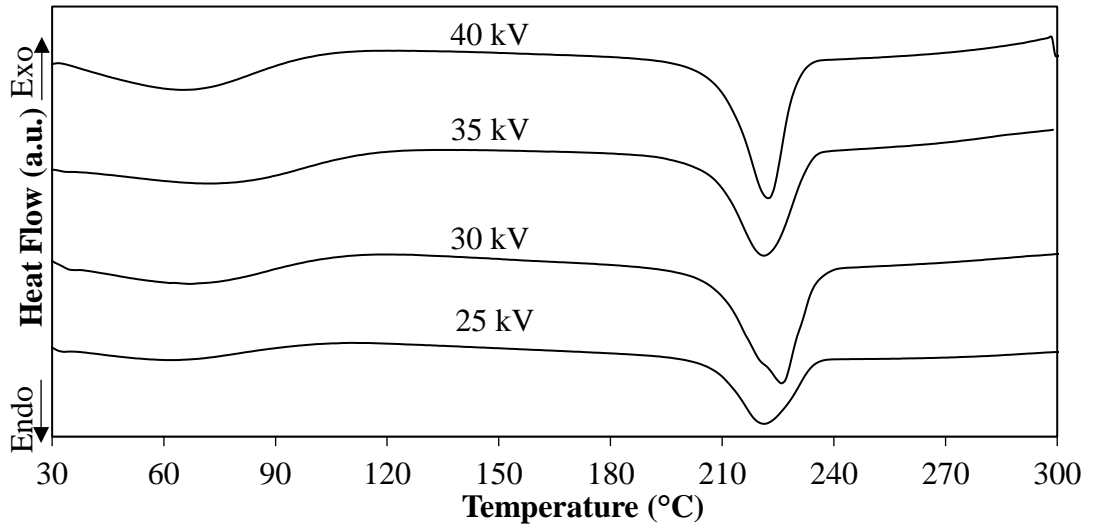


Figure B.1. DSC curves of the nanofibers produced using different applied voltage values.

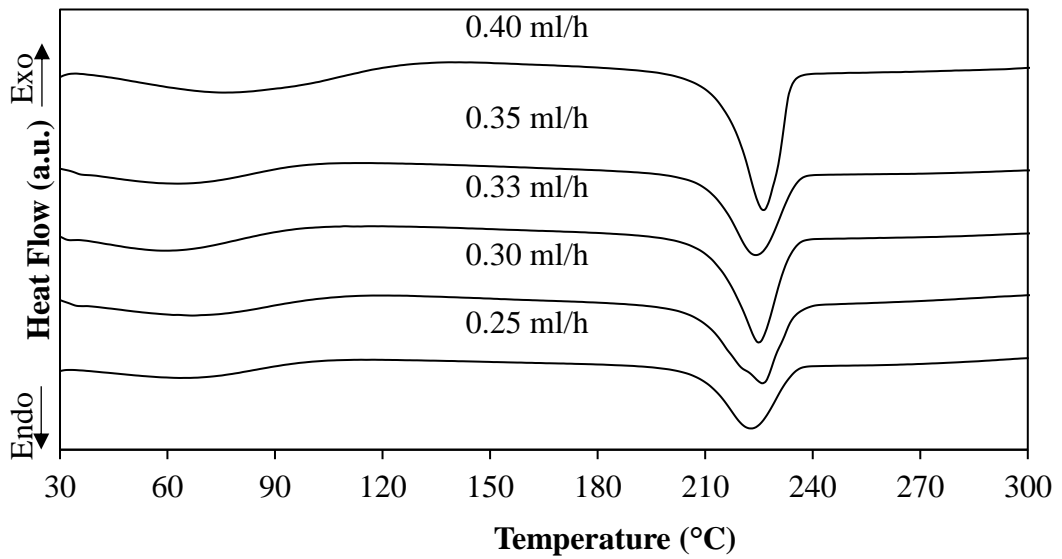


Figure B.2. DSC curves of the nanofibers produced using different feed rate values.

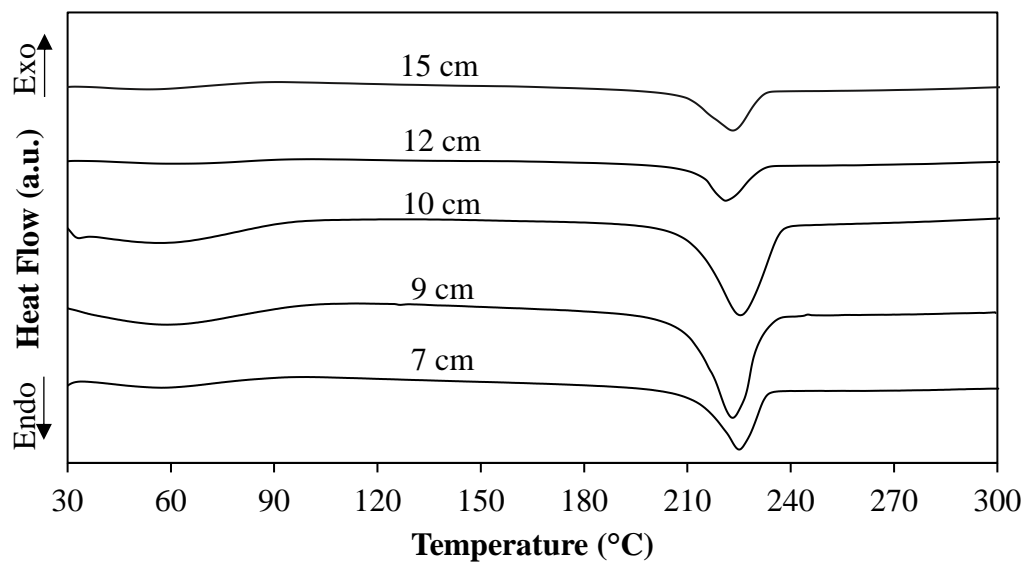


Figure B.3. DSC curves of the nanofibers produced using different tip-to-collector distance values.

APPENDIX C

RAW DATA OF TENSILE TEST RESULTS

Table C.1. Tensile test data of the nanofiber mats produced using different voltage values.

Applied Voltage (kV)	Tensile Strength (MPa)	Tensile modulus (MPa)	Elongation at Break (%)
25	7.97 ± 0.80	70.22 ± 8.47	47.60 ± 5.62
30	7.24 ± 0.59	76.82 ± 5.66	58.07 ± 5.95
35	8.46 ± 0.71	82.70 ± 13.12	40.20 ± 3.42
40	6.73 ± 1.53	73.01 ± 9.52	37.92 ± 6.57

Table C.2. Tensile test data of the nanofiber mats produced using different feed rate values.

Feed Rates (mL/h)	Tensile Strength (MPa)	Tensile modulus (MPa)	Elongation at Break (%)
0.25	8.95 ± 1.96	83.61 ± 3.811	51.30 ± 15.30
0.30	7.24 ± 0.59	76.82 ± 5.66	58.07 ± 5.95
0.33	10.02 ± 1.29	101.22 ± 14.77	62.75 ± 5.44
0.35	10.00 ± 0.85	86.72 ± 15.64	54.80 ± 2.50
0.40	12.59 ± 3.17	82.36 ± 8.39	58.50 ± 8.70

Table C.3. Tensile test data of the nanofiber mats produced using different tip-to-collector distance values.

Tip-to-Collector Distance (cm)	Tensile Strength (MPa)	Tensile modulus (MPa)	Elongation at Break (%)
7	7.30 ± 0.71	88.11 13.42	51.96 5.36
9	7.88 ± 0.63	98.21 ± 10.07	70.70 ± 4.20
10	10.02 ± 1.29	101.22 ± 14.77	62.75 ± 5.44
12	7.62 ± 0.84	104.06 ± 8.03	49.99 ± 1.48
15	7.50 ± 1.55	80.57 ± 17.09	43.65 ± 6.45

Table C.4. Tensile test data of the composite nanofiber mats containing un-HNTs and m-HNTs.

Sample	Tensile Strength (MPa)	Tensile modulus (MPa)	Elongation at Break (%)
PA6	7.24 ± 0.59	76.82 ± 5.66	58.07 ± 5.95
1 wt.% un-HNT	7.34 ± 0.88	60.24 ± 10.65	58.61 ± 7.88
1 wt.% m-HNT	7.95 ± 1.80	96.06 ± 13.16	47.66 ± 7.18
2 wt.% un-HNT	7.18 ± 0.76	69.33 ± 4.28	57.37 ± 3.77
2 wt.% m-HNT	7.64 ± 0.80	76.59 ± 5.86	48.39 ± 4.89
4 wt.% un-HNT	8.41 ± 0.99	61.90 ± 5.99	56.97 ± 4.07
4 wt.% m-HNT	7.33 ± 0.93	69.45 ± 7.20	51.17 ± 6.32
6 wt.% un-HNT	7.42 ± 0.38	73.70 ± 4.08	59.70 ± 5.13
6 wt.% m-HNT	8.01 ± 0.80	68.82 ± 6.17	49.04 ± 5.16
8 wt.% un-HNT	7.69 ± 0.54	68.80 ± 7.61	57.10 ± 4.09
8 wt.% m-HNT	6.65 ± 0.55	74.23 ± 6.92	53.61 ± 5.84

Table C.5. Tensile test data of the samples exposed to different chemical vapors in the old setup.

Chemical Vapors	Sample	Tensile Strength (MPa)	Tensile modulus (MPa)	Elongation at Break (%)
Unexposed	Neat	9.94 ± 0.95	139.30 ± 16.06	58.11 ± 3.61
	1 wt.%	10.53 ± 1.02	144.69 ± 14.11	63.73 ± 5.99
	8 wt.%	9.32 ± 0.79	146.43 ± 15.49	48.27 ± 5.33
HCl	Neat	8.91 ± 1.36	82.51 ± 13.26	43.60 ± 13.42
	1 wt.%	8.66 ± 1.07	95.30 ± 19.52	35.98 ± 10.28
	8 wt.%	7.48 ± 0.97	139.96 ± 11.51	24.23 ± 2.05
Acetone	Neat	9.54 ± 1.29	127.81 ± 7.91	44.62 ± 11.51
	1 wt.%	8.52 ± 1.44	118.24 ± 16.53	48.87 ± 4.83
	8 wt.%	8.76 ± 0.42	106.30 ± 7.49	29.32 ± 5.94
Toluene	Neat	8.65 ± 0.72	121.30 ± 12.54	58.20 ± 10.04
	1 wt.%	10.39 ± 1.77	150.65 ± 10.26	66.71 ± 2.31
	8 wt.%	9.07 ± 1.14	118.64 ± 17.47	48.92 ± 9.42
Water	Neat	7.61 ± 0.63	100.08 ± 14.61	29.98 ± 7.20
	1 wt.%	9.08 ± 0.77	105.02 ± 11.62	35.80 ± 5.95
	8 wt.%	9.44 ± 0.95	125.11 ± 10.23	33.64 ± 9.80

Table C.6. Tensile test data of the samples exposed to different chemical vapors in the new setup.

Chemical Vapors	Sample	Tensile Strength (MPa)	Tensile modulus (MPa)	Elongation at Break (%)
Unexposed	Neat	11.52 ± 1.04	95.07 ± 6.82	73.14 ± 5.95
	1 wt.%	9.71 ± 1.63	102.77 ± 11.37	46.96 ± 8.88
	8 wt.%	10.67 ± 1.48	105.90 ± 11.75	48.93 ± 10.67
HCl	Neat	6.96 ± 0.64	69.35 ± 6.95	27.69 ± 2.42
	1 wt.%	9.45 ± 2.05	93.10 ± 12.87	32.87 ± 10.10
	8 wt.%	7.53 ± 0.58	64.56 ± 5.93	30.29 ± 3.12
Acetone	Neat	8.43 ± 1.34	67.22 ± 8.73	45.03 ± 8.74
	1 wt.%	10.13 ± 1.33	73.71 ± 9.99	47.22 ± 5.35
	8 wt.%	8.38 ± 1.41	83.47 ± 8.44	37.27 ± 12.56
Toluene	Neat	12.12 ± 1.30	76.27 ± 16.05	60.74 ± 6.78
	1 wt.%	11.71 ± 1.55	91.17 ± 8.20	58.83 ± 8.12
	8 wt.%	13.13 ± 1.14	87.35 ± 8.67	55.95 ± 8.53
Water	Neat	11.45 ± 0.92	74.51 ± 12.67	38.02 ± 4.18
	1 wt.%	7.88 ± 1.09	73.99 ± 6.25	34.37 ± 7.15
	8 wt.%	11.66 ± 1.36	89.30 ± 12.40	40.49 ± 5.97

APPENDIX D

SAMPLE CALCULATION OF DIFFUSION COEFFICIENT

Equation 2.4 was used to calculate the diffusion coefficient of the samples containing 1 wt.% m-HNTs exposed to acetone vapor in accordance with the Fick's Second law. In the equation, M_t shows the percent weight increase of the sample at time t , M_∞ stands for the percent weight increase at the equilibrium, D is diffusion coefficient, l is the half thickness of the sample, and the t is the time. Using the values of samples containing 1 wt.% m-HNTs exposed to acetone vapor in Table D.1, the normalized weight increase graph was plotted as a function of the square root of the time. This graph was used to calculate the slope and diffusion coefficient obtained from the region where the normalized mass increase is less than 0.5.

Equation 2.4 is given below.

$$\frac{M_t}{M_\infty} = 2 \left(\frac{D}{\pi l^2} \right)^{1/2} t^{1/2} \quad (2.4)$$

Table D.1. Data used to calculate the diffusion coefficient of the samples containing 1 wt.% m-HNTs exposed to acetone vapor.

	Values								
Time (h)	0	4.6	27.7	52.2	75.5	100	124	147.5	171.5
Time ^{1/2} (h ^{1/2})	0	2.1	5.3	7.2	8.7	10	11.1	12.1	13.1
M _t (%)	0	1.420	2.150	3.008	2.559	3.380	3.230	2.772	2.910
M _∞ (%)	2.971								
M _t /M _∞	0	0.477	0.724	1.013	0.861	1.138	1.087	0.933	0.980
l (m)	2.095x10 ⁻⁵ ± 5.008x10 ⁻⁶								

The normalized weight change is less than 0.5 (0.477) was used to calculate the value of the diffusion coefficient. The calculation steps are shown below.

$$0.477 < 0.5$$

$$0.477 = 2.1 \times 3600 \times \left(\frac{2 \times D^{1/2}}{\pi^{1/2} \times 2.095 \times 10^{-5}} \right)$$

$$D = \left(\frac{0.477}{2 \times 2.1 \times 3600} \times \pi^{1/2} \times 2.095 \times 10^{-5} \right)^2 = 4.94 \times 10^{-15} \text{ m}^2/\text{s}$$

As a result, the diffusion coefficient was calculated as $4.94 \times 10^{-15} \text{ m}^2/\text{s}$ for the sample containing 1% m-HNTs exposed to acetone vapor.

APPENDIX E

CUMULATIVE FREQUENCY GRAPHS OF THE SAMPLES EXPOSED TO DIFFERENT CHEMICAL VAPORS

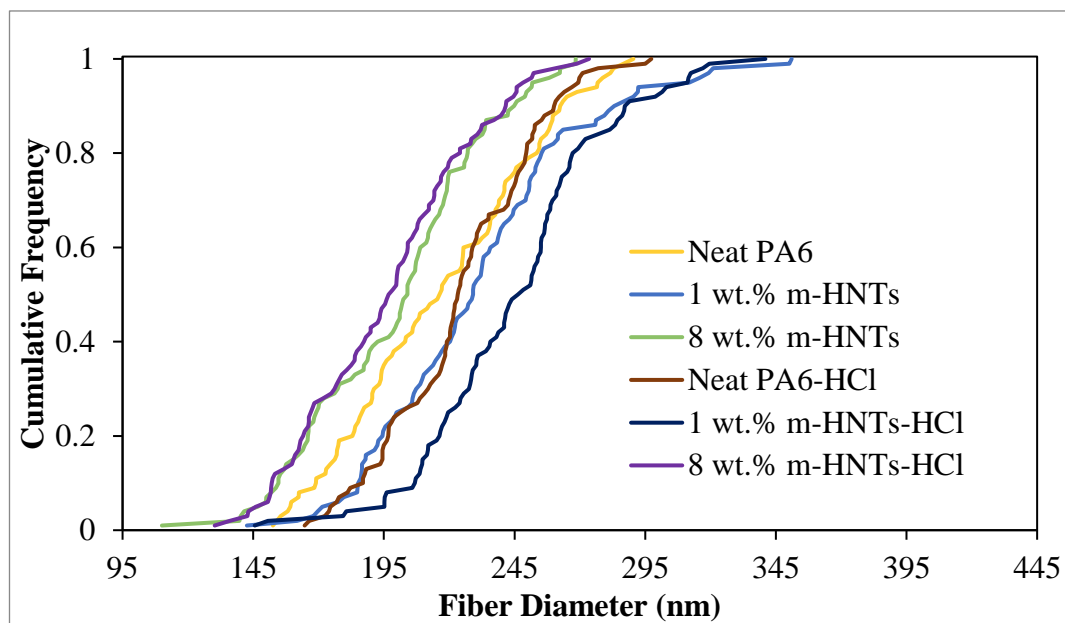


Figure E.1. Cumulative frequency plots of fiber diameters of the samples exposed to HCl vapor in the old setup.

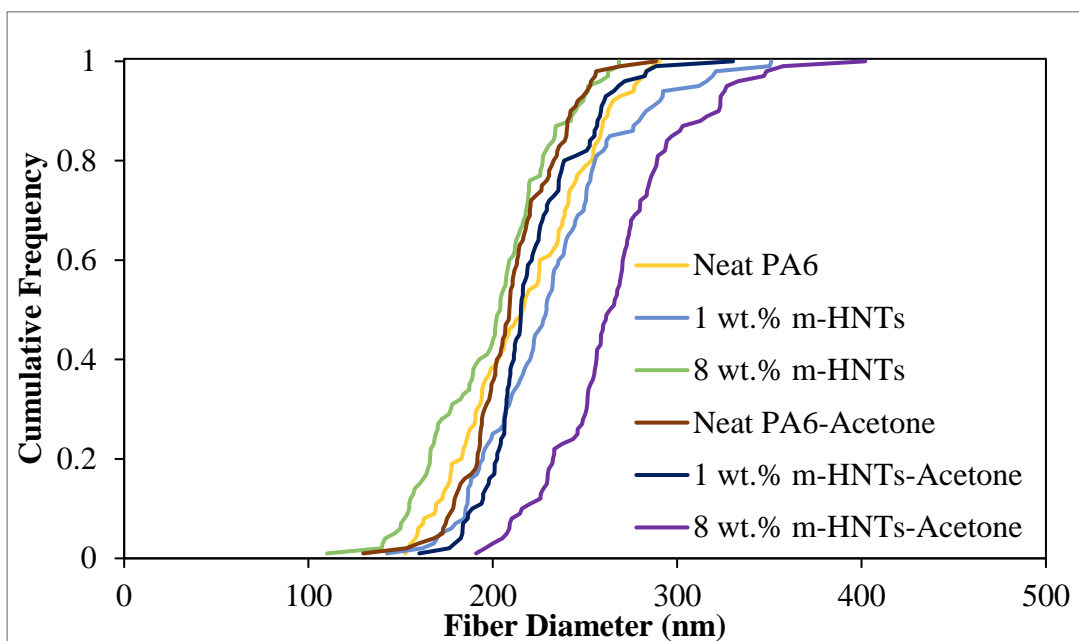


Figure E.2. Cumulative frequency of fiber diameters of the samples exposed to acetone vapor in the old setup.

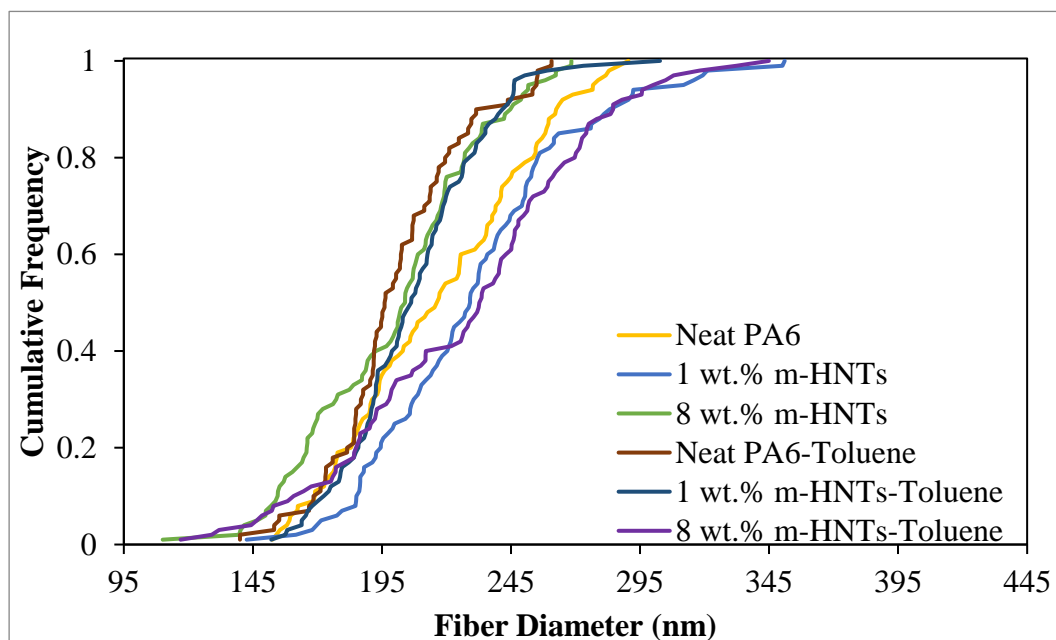


Figure E.3. Cumulative frequency of fiber diameters of the samples exposed to toluene vapor in the old setup.

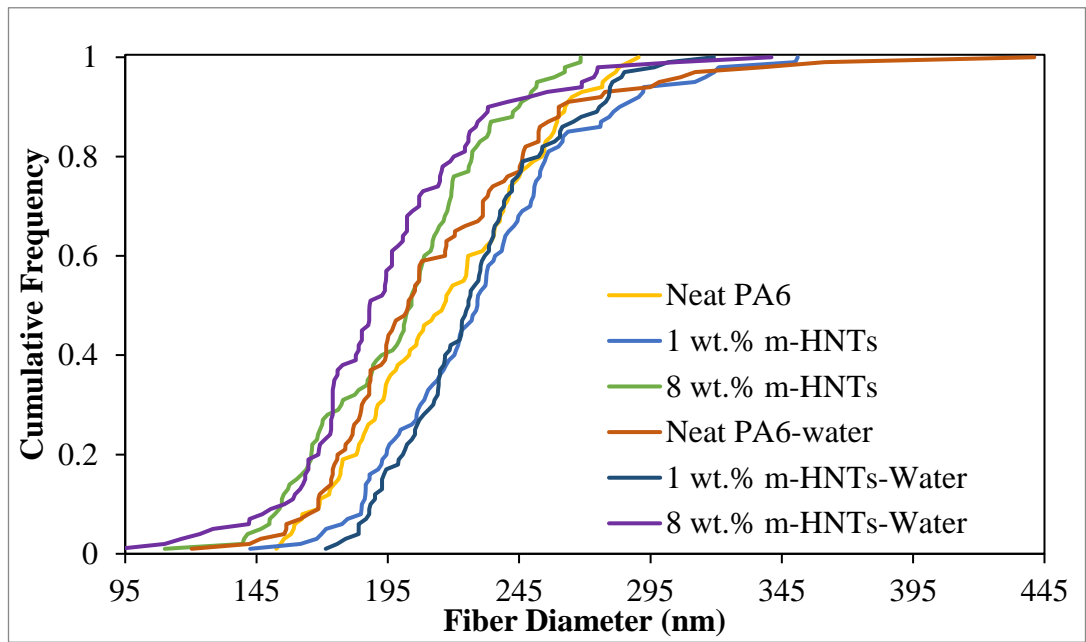


Figure E.4. Cumulative frequency of fiber diameters of the samples exposed to water vapor in the old setup.

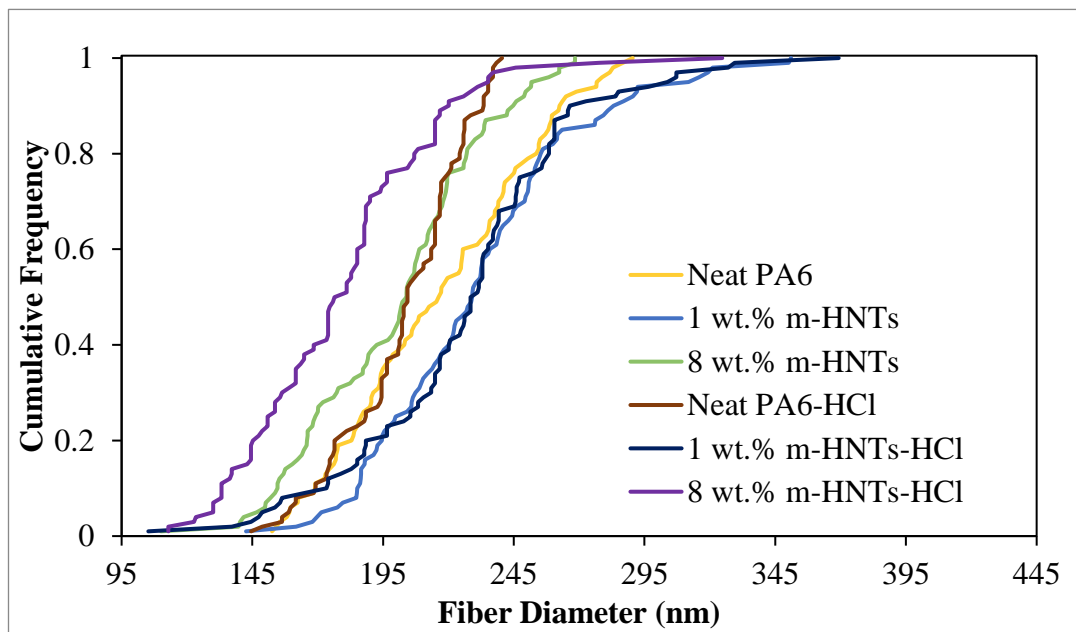


Figure E. 5. Cumulative frequency of fiber diameters of the samples exposed to HCl vapor in the new setup.

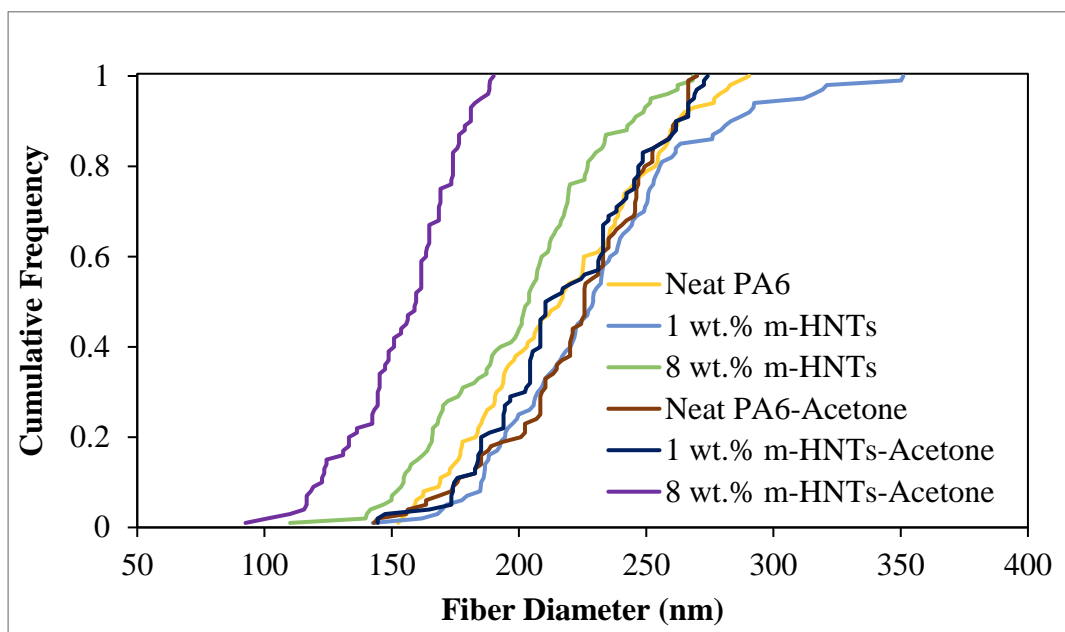


Figure E.6. Cumulative frequency of fiber diameters of the samples exposed to acetone vapor in the new setup.

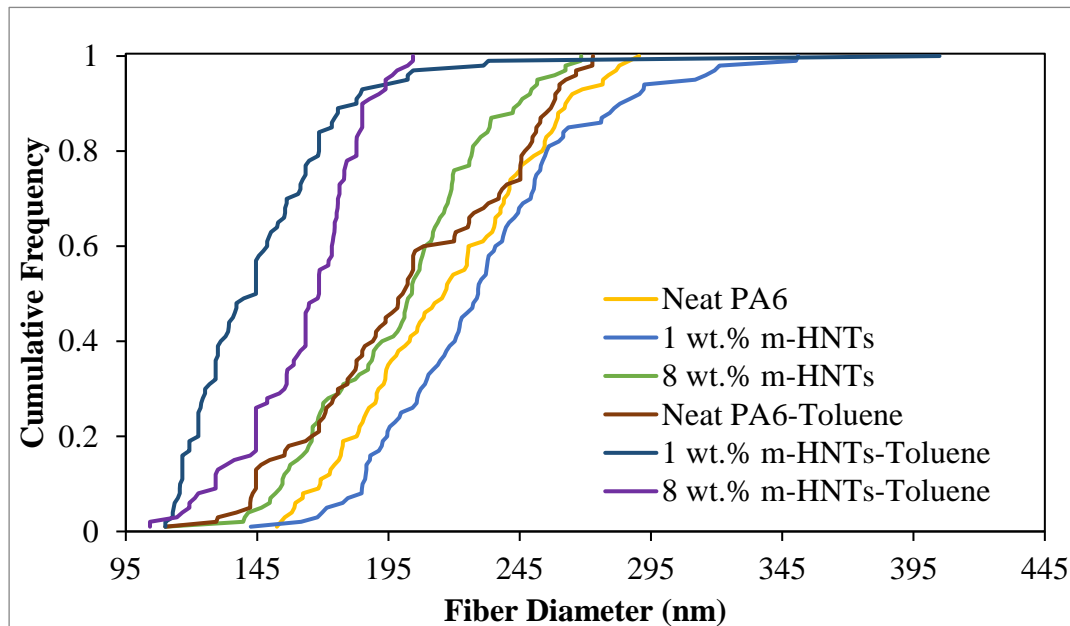


Figure E.7. Cumulative frequency of fiber diameters of the samples exposed to toluene vapor in the new setup.

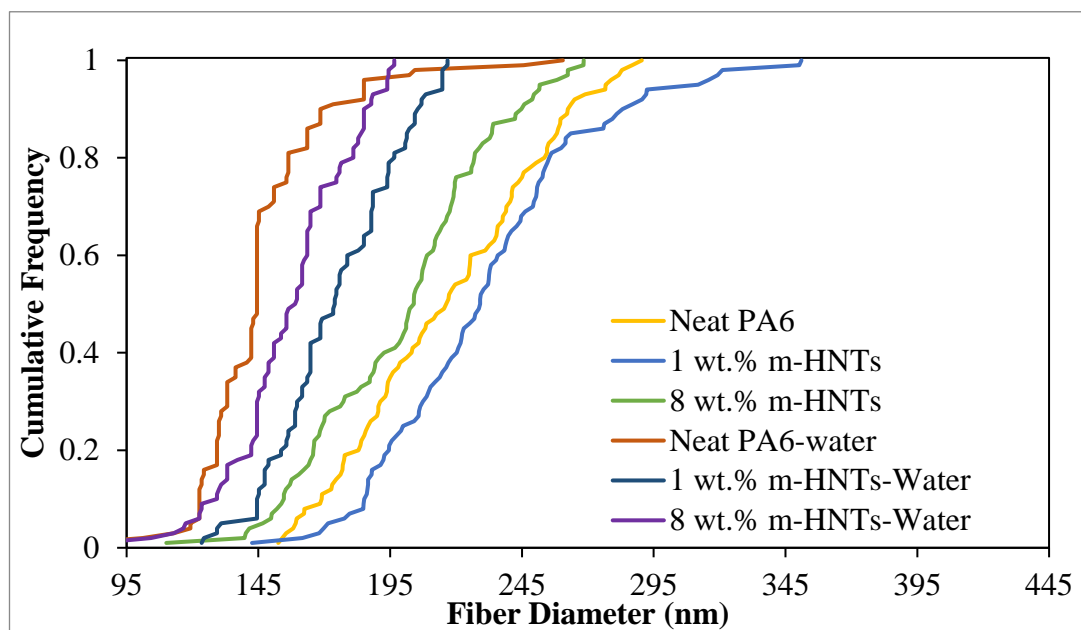


Figure E.8. Cumulative frequency of fiber diameters of the samples exposed to water vapor in the new setup.